KNITTED SMART STRUCTURES: MODELING VIA FINITE ELEMENT ANALYSIS AND EXPERIMENTAL INVESTIGATION

A Thesis

by

HANNAH ROSE STROUD

Submitted to the Office of Graduate and Professional Studies of
Texas A&M University
in partial fulfillment of the requirements for the degree of

MASTER OF SCIENCE

Co-Chair of Committee,	Darren Hartl
Co-Chair of Committee,	Kristi Shryock
Committee Member,	John Whitcomb
Head of Department,	Rodney Bowersox

August 2020

Major Subject: Aerospace Engineering

ABSTRACT

The properties of shape memory alloy (SMA) wires have long been leveraged in a variety of industries. Straight wires using the shape memory effect have been used as linear actuators in applications that range from valve actuation to robotic grippers, while wires using the pseudoelastic effect have been used in medical devices such as guidewires and stents for years. While properties of straight wire-formed SMA are well understood, complex geometries developed from SMA wire such as knits are less explored. Early experimental results indicate that such geometries have structural advantages in bending and are more flexible than weaves and meshes (which use mostly straight wire). SMA knits are therefore a good candidate for medical and bio-compatible devices, as the human body often demands flexibility, particularly in limbs and joints. In addition, knitted structures have the unique ability to be tailorable in both structure and material for improved shaping and variation structural response compared with weave-based fabrics. Knitting techniques and patterns developed in the textile industry allow for variable materials and geometries in the same structure, allowing for a large range of tailored macro-structure responses based on knit pattern alone.

Current models for these types of smart structures are simplistic, however. Out of plane deformation and 3D geometry of stitches are ignored, and contact interactions between stitches are considered only as constraints on stitch motion. This work seeks to develop and validate a finite element model for SMA knitted structures incorporating the Boyd-Lagoudas SMA transformation model. A representative volume element (RVE) is developed for common knit patterns, and macro-structure response is explored and experimentally validated. This research provides a foundation for better understanding fundamental capabilities and responses of knitted SMA structures, allowing for better design, functionality, and customizability of the existing devices that use them and enabling new designs.

DEDICATION

To my parents.

There are more things in heaven and earth, Horatio, Than are dreamt of in our philosophy.

ACKNOWLEDGMENTS

I would like to thank my advisors for their guidance and support, my officemates for their candor and geniality, and my lab-mates for cultivating an environment that fosters collaboration and advancement. Special thanks goes to Patrick Walgren, Pedro Leal, William Scholten, and Andrew Leaton who provided thoughtful reviews of this document.

CONTRIBUTORS AND FUNDING SOURCES

Contributors

This work was supported by a thesis committee consisting of Professors Darren Hartl, co-advisor, and Kristi Shryock, co-advisor, of the Department of Aerospace Engineering, and Professor John Whitcomb of the Department of Materials Science and Engineering.

The user-defined material subroutine (VUMAT) used in this work was developed by Dr. Alex Solomou. All other work conducted for the thesis was completed by the student independently.

Funding Sources

Graduate study was supported by a Graduate Diversity fellowship from Texas A&M University and by NSF project REvolutionizing Diversity Of Engineering (REDO-E) (project 1730693).

NOMENCLATURE

SMA	Shape Memory Alloy
Stitch	Single loop that is patterned or repeated in various ways to compose a knitted structure
Knit	A stitch type that results in a loop being pulled through the front of the fabric. Often represented in patterns as a "V"
Purl	A stitch type that results in a loop being pulled through the back of the fabric. Often represented in patterns as a "–"
Course	Horizontal group of stitches of a knitted structure
Wale	Vertical group of stitches of a knitted structure
Garter	The simplest knit pattern. It is comprised of alternating courses of knits and purls
Stockinette	Another basic knit pattern. It is comprised entirely of knits
Rib	A slightly more complex knit pattern where courses alternate knit and purl stitches. Often seen in sweater cuffs
Seed	A slightly more complex knit pattern where courses and wales alternate knit and purl stitches. Often seen in knitted neckties
Cast-on	A base chain of loops through which the first row will be started
Cast-off	A finishing technique that mimics the form of a cast-on

TABLE OF CONTENTS

Page

LIST OF FIGURES

FIGURE Page

LIST OF TABLES

TABLE Page

1. INTRODUCTION AND LITERATURE REVIEW

Since its development in the 3rd century [1], knitting has revolutionized the capabilities of textiles. New garments, namely the stocking and sock [2], were developed as a result of the advent of this technique by way of the seamless fabrics with an unmatched ability to stretch that were created using knitting. The unique properties of knits are enabled by their interconnected looping structure which, unlike the largely straight members that comprise woven fabrics, contains many interlocked bends. Manipulating the structure by changing the way in which these loops connect provides knits with the ability to tailor properties governing shape, stretch, and fit within a single fabric via the stitch architecture or knit pattern [3]. Knitted structures themselves have long been investigated from an engineering perspective, with geometric and mechanical models appearing in the 1930s [4]. While their unique structure provides performance advantages, knit performance is also influenced by properties of the base material [5]; in particular, by coupling knitting techniques with smart materials, in this case shape memory alloys (SMA), new capabilities can be explored. Though the study of SMA wires was popularized in the 1960s, knitted configurations of this material are a more recent study [6]. As new applications emerge, reliably predicting the response of these structures and motivating design decisions necessitates the development of models accounting for actuation response and complex contact interactions.

Applications in compression garments and medical devices motivated some modeling of knitted SMA, but models that incorporate actuation behavior and fully capture contact interactions inherent in inter-stitch linking have yet to be developed.

1.1 Modeling Knitted Structures

Certain terminology is useful in accurately describing a knit structure. Knits are characterized by repeating unit loops, or *stitches*, of a continuous thread-like medium interlocked in varying ways to create a *pattern*. A knit stitch is a loop that is pulled through the front of the fabric, while a purl stitch is a loop that is pulled through the back of the fabric. This is illustrated in figure 1.1,

where knit stitches are depicted in gray and purl stitches are depicted in maroon. The use of knit or purl stitches along a *wale*, a column of stitches, and/or *course*, a row of stitches, dictate fabric pattern [1].

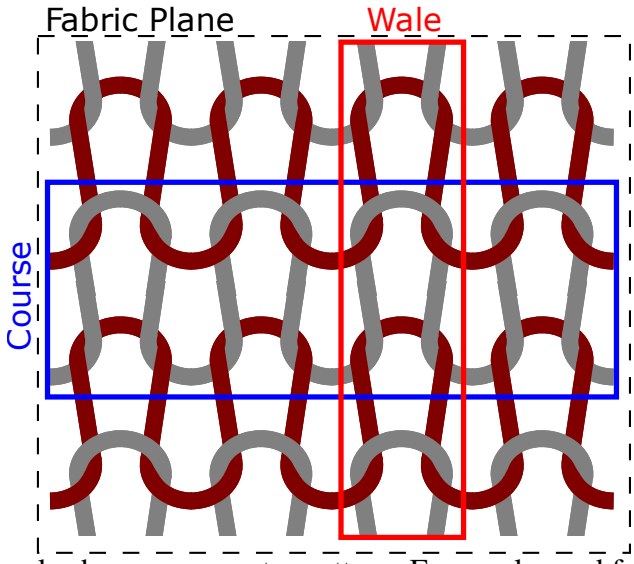

Figure 1.1: Course and wale shown on a garter pattern. Four wales and four courses are depicted.

Knitted loops are inherently non-linear in their behavior due to their geometry and resulting interactions with surrounding stitches. Important considerations for modeling knitted structures include three areas: single stitch geometry, fabric-level knit pattern, and material behavior.

1.1.1 Review of Knit Geometry Models

The Industrial Revolution, with its distinct focus on textile manufacturing, brought about a search for descriptions for the geometry of knitted structures. Originally, many of these models sought not only to provide some insight into fabric behavior, but to develop accurate estimates of stitch lengths and yarn required for increasingly complex patterns. Three main types of knit models were investigated in the early 20th century: geometric, mechanical, and energy loop models [4]. Geometric loop models sought to describe knit stitch shapes mathematically, while mechanical models sought to describe changes in loop dimensions and stitch shape as a result of forces and displacements, and energy models sought to improve upon mechanical models by using energy

methods to solve for stitch response. In developing a basis for loop shape for this work, geometrical models are of particular significance. Examples of popular models that led to the development of the geometry used in this work are given below. Notably, each of the models discussed herein is based on a stockinette architecture, described in section 1.1.2, which motivates choice in side plane projection geometry.

Peirce developed an early three dimensional geometric model based on empirical observations. This model defines stitch geometry as circular segments for needle and sinker loops with straight segments for connecting legs when projected on a fabric plane [7]. The parameters of this model are based on the angle between the knit centerline and the line between geometry-defining circle centers, diameter of the geometry defining circles, and the angle between the centerline and the connection point between loop and leg. Stitch curvature is assumed to be semi-cylindrical as if pressed along the top half of a cylinder running along each course. This assumption coupled with the geometry of the fabric projection proved to be over-simplified, however, as Leaf and Glaskin demonstrated torsional inconsistencies with Peirce's 3D geometry [8]. Choosing to maintain the course-wise cylinder assumption (i.e. semi-circular side plane projection), Leaf and Glaskin developed a torsionally consistent fabric projection based only on circles. Parameters in this model are largely based on angles to stitch contact and angles between centerline and the line between geometry-defining circle centers, making it an interesting choice for studies in knit structure extension.

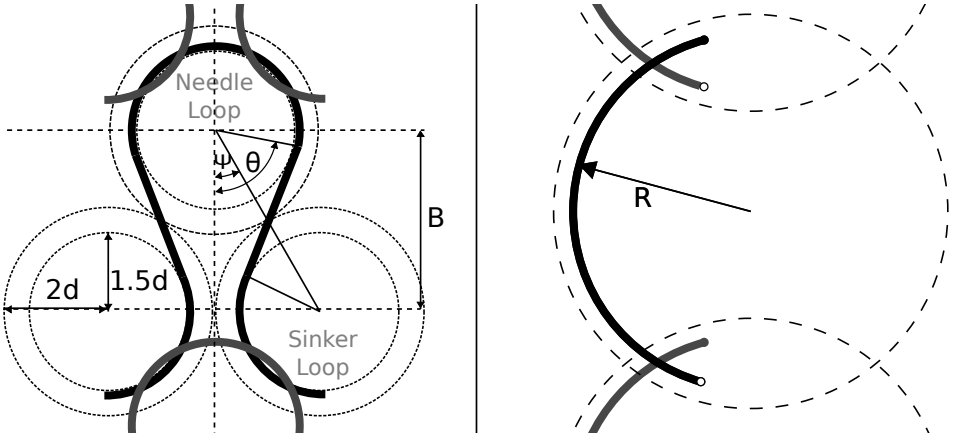

(a) Peirce's model.

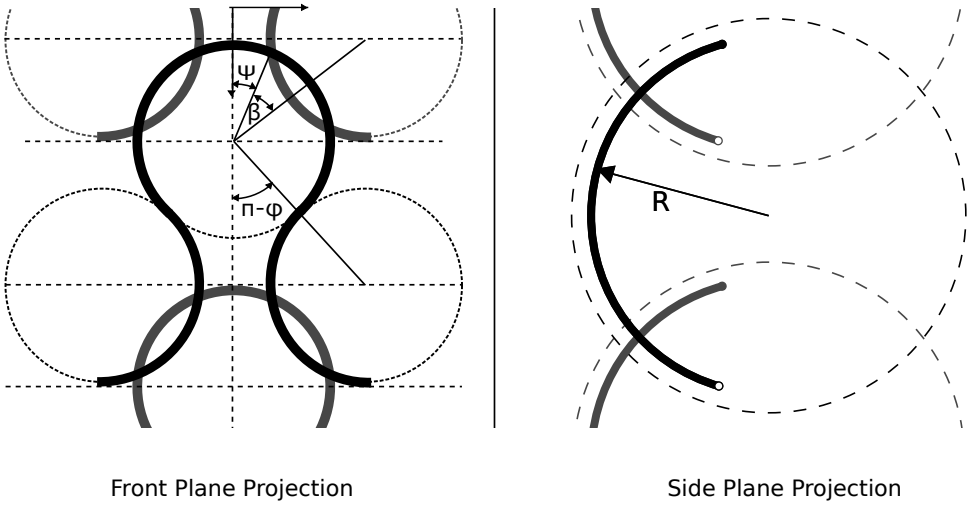

(b) Leaf and Glaskin's model.

Figure 1.2: Projections of two geometric models of a knit stitch [7, 8].

Later models sought the simplicity and visual similarity to physical knits present in Peirce's model without the torsional inconsistencies. For example, Suh's geometric model closely resem-

bles Peirce's with key exceptions: needle and sinker loops on the fabric projection are circular but not centered at the leg intersection point, and stitch curvature in the side plane projection is not assumed to be semi-circular [9].

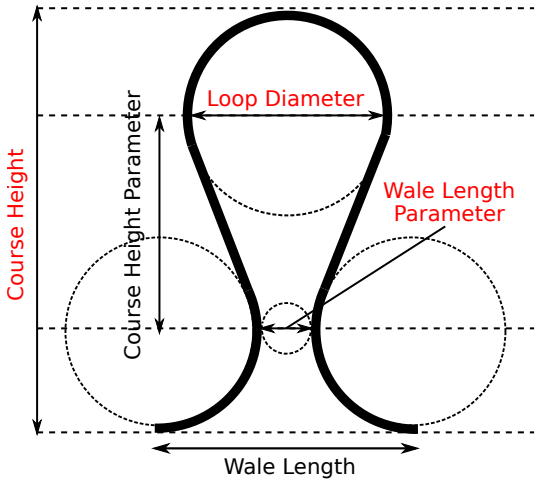

Figure 1.3: Geometry based on Peirce's model of a knit stitch.

The geometric model developed for this work must be compatible with stitch architectures other than stockinette; therefore, no assumptions are made regarding side plane projection geometry. Geometric considerations used in the FEA model in this study most closely resemble the fabric plane projection of Peirce's knit model, though key changes are made to ensure the needle and sinker loops connect to the straight legs at points that are exactly tangent to prevent stress concentrations[1]. The dominating geometric features, shown in figure 1.3, were chosen for simplicity and visual resemblance to wire knits, which maintain a relatively constant bend radius and do not kink as severely as yarn. The parameters for this geometry are loop diameter, a course height parameter, a wale length parameter, course height, and wale length. These parameters were chosen so that dimensions from experimental samples could be easily found. Concerns regarding torsional inconsistencies of Peirce's 3D model can be neglected without an assumed side plane projection; side plane geometry is solved for in terms of displacement during FEA and therefore

[1] See appendix A for notes on the construction of the tangent line.

must be torsionally consistent.

1.1.2 Knit Architectures

Knit architectures are combinations of the two types of stitches, knit or purl, that compose a unit; when those units are repeated and/or combined, a pattern is created [10]. The most basic pattern types have courses that are composed of only one type of stitch (i.e. knit or purl). Examples of this basic type of pattern are garter pattern and stockinette pattern, which can be minimally represented with two stitches.

A garter architecture uses courses of consistent stitch type where each course alternates between knit and purl. A single wale exhibits one plane of symmetry, shown in figure 1.4. This architecture is less commonly seen in clothes than other architectures despite its simplicity. It is the simplest architecture to construct via hand knitting; however, it may be less common because it is inherently more complex to construct via machine knitting due to its courses alternating between knit and purl stitches.

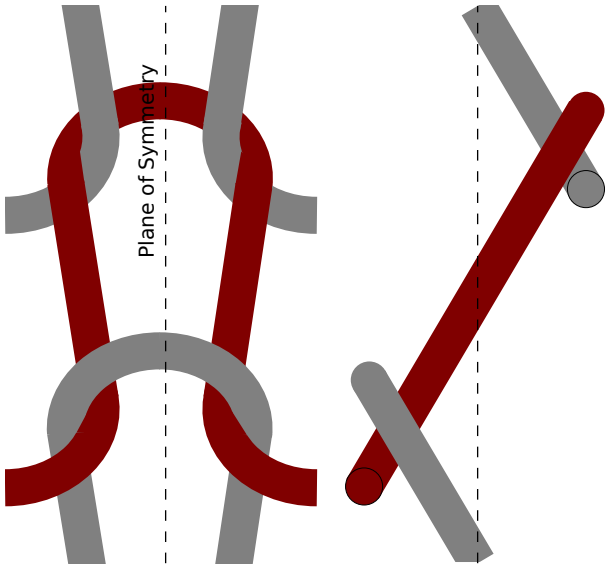

(a) Front view. (b) Side view.

Figure 1.4: Garter stitch schematic.

A stockinette architecture is composed entirely of knit stitches and has one plane of symmetry (figure 1.5b). This architecture is commonly seen in simple knitted clothing garments because it is the simplest architecture to construct with a knitting machine.

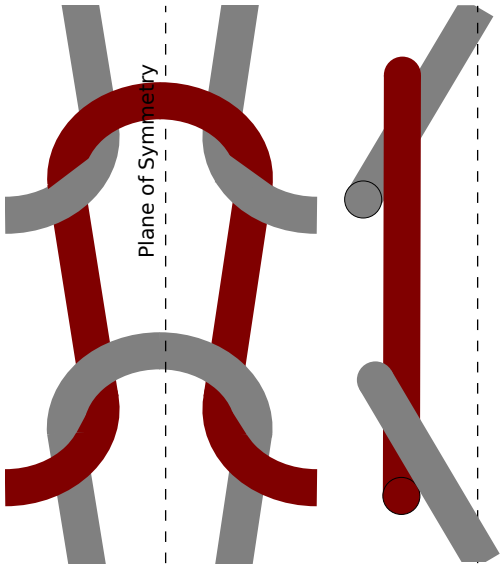

(a) Front view. (b) Side view.

Figure 1.5: Stockinette stitch schematic.

More complex patterns can be created by patterning these architectural units in a certain way. A rib architecture, for example can be created by mirroring a stockinette wale over the right or left side of the original stockinette stitch. The resulting pattern contains wales comprised of a single stitch type and courses consisting of alternating knit and purl. Rib architecture can be minimally expressed using four complete stitches. This architecture offers a uniquely high capacity for stretch, allowing garments to remain fitted to the wearer after the donning process. This makes it ideal for garment finishings, including sleeve cuffs, waist bands, and hat bands.

In a similar way, a seed architecture can be formed by treating a unit garter stitch in the same way. The resulting pattern consists of both wales and courses that alternate knit and purl. Seed architecture can also be minimally represented with four stitches. It is often used in knitted neckties due to its interesting appearance.

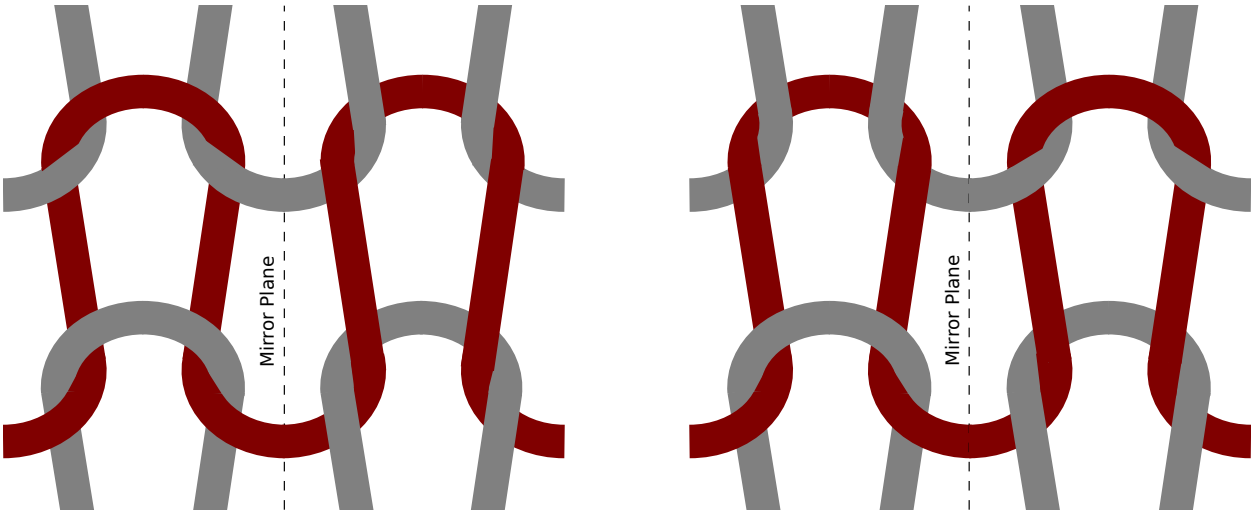

(a) Rib stitch. (b) Seed stitch.

Figure 1.6: Repeated patterns represented by four stitches.

Figure 1.7 provides examples of the appearance of such architectures when knitted into physical fabrics. To better display the differences in these patterns, monolithic yarn (i.e. yarn comprised of a single strand rather than many strands wound together) is used.

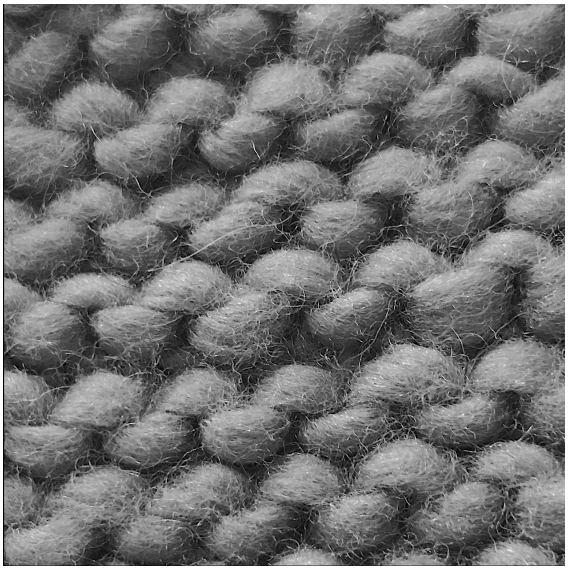

(a) Garter stitch.

(b) Stockinette stitch.

(c) Rib stitch.

(d) Seed stitch.

Figure 1.7: Knit samples.

1.2 Overview of Shape Memory Alloys

Shape memory alloys are a class of metallic material with the ability to undergo a martensitic phase transformation from a parent austenite phase [11]. This transformation can be induced through stress-based or thermal stimuli (or a combination of the two) and generates a recoverable

transformation strain, providing SMAs with unique strain recovery and actuation capabilities. The simplest cases of transformation exist when changes in stress or temperature are isolated from each other. In isothermal conditions, a sufficient stress stimulus applied to an austenitic SMA sample prompts the transformation into martensite, and upon removal of the stress, reverse transformation occurs and the transformation strain generated during loading is recovered [11]. This response is commonly referred to as the superelastic response of SMAs. In isobaric conditions, an austenitic SMA sample generates up to 5% transformation strain upon cooling; when heated, the sample recovers the transformation strain [11]. This type of cycling gives rise to the use of SMAs as actuators.

1.3 Prior Studies on Knitted SMA

SMAs in a knitted form were first investigated in the 1980s for use in medical catheters [12]. As applications in medicine and later aerospace continued to emerge, efforts were made to model the behavior of these structures as well. Section 1.3.1 introduces prior work on characterization efforts of knitted SMA structures, section 1.3.2 describes some of these proposed applications, and section 1.3.3 details the modeling efforts motivated by these advancements.

1.3.1 Investigations on Actuation Behavior

Early studies on actuation behavior of knitted structures were empirical investigations primarily focused on a given knit architecture's response to thermal stimuli [13, 14]. Subsequent works sought to characterize actuation performance of a garter stitch architecture under low loads (i.e. on the order of 1 N for a sample of 15 courses and 15 wales) and identify effects of stitch geometry on actuation [15, 16]. Preliminary efforts to investigate the effect of shape setting, a technique commonly used to introduce a new zero-stress configuration to an SMA structure, on knitted structures of a garter stitch architecture found a decrease in actuation displacement for structures shape set with tension in the wale-wise direction compared with non-shape set structures [17]. An experimental framework for design, characterization, and operation of knitted SMA actuators under low loads has been proposed based on prior literature [18].

1.3.2 Applications

Due to their flexibility in bending and pseudoelastic behavior, SMA knit structures are of particular interest for biomedical applications, particularly in-vivo implants. Traditional stents, for example, in regions subject to large degrees of bending or body motion may apply excessive pressure to tissue, leading to tissue rupture or device kinking, which can cause protrusions and punctures [19]. Knitted stents can accommodate these bends appropriately, allowing for improvements in challenging stent placements such as those in the esophagus [20]. Similarly, knitted vein graft support meshes, used to provide a supportive radial inward force to veins in coronary bypass procedures, have been shown to have longer operational life spans and greater kink resistance than their braided counterparts [21]. Orthopedic implant spacers for stronger implant fixation [22], scaffolds for tissue growth and regeneration [23], and high-stretch prosthetic devices [24] have also been improved by the use of knitted structures comprised of smart materials.

Aerospace engineering applications of knitted smart materials often employ the active transformation behavior of SMAs. For example, a rib stitch architecture overlaid on an aerodynamic surface has been shown to enable flow control capabilities by actuating into the flow, causing a surface displacement [25]. A challenging and important application for active knits is a mechanical counter-pressure (MCP) bio-suit to enable space exploration [26]. Current space suits rely on air pressure, making them bulky and challenging to don, doff, and maneuver in; an MCP suit would form fit to the wearer and provide a controlled pressure while accounting for large deformations at anatomic points of flexion.

At the juncture between aerospace engineering-motivated designs and biomedical engineering-based designs sits the unique category of wearables enabled by active SMA knits. Compression garments, commonly needed medical devices often used to improve blood flow, may behave in ways similar to an MCP space suit. Active compression garments have been investigated in a medical sense for treatment of orthostatic hypotension [27]. Additionally, such garments have been proposed as a method of enabling future smart wearable design through improved active fitting capabilities [28, 29, 30].

1.3.3 Modeling Efforts of Knitted SMA

A two-dimensional analytical model was developed by Abel et al. to investigate a garter stitch architecture [31]. This state-based model considers mechanical and thermal operations performed on an initial state to model fabric extension at four material states. However, this model does not capture the out of plane deformation of the knit nor capture the full transformation behavior of the SMA. Additionally, a finite element model which incorporates a superelastic SMA model of a nitinol vein graft mesh was developed [32]. This model was developed as a design tool to investigate the effects of parameters such as loop geometry and wire diameter on radial compression performance of vein graft meshes. This model, however, does not account for the actuation features of SMA, as it employs the Auricchio model of superelasticity [33]. In addition, current knit models only account for a single stitch architecture in a fabric. To investigate more complex knit patterns employing multiple architectures, new models must be developed.

1.4 Thesis Overview

The overarching goal of this work is to develop and experimentally validate a model that captures both non-linear geometric behavior due to large, unpredictable contact regions and non-linear material behavior. This work will build off tools developed by previous researchers and will utilize insights from previous studies in knitted SMAs. The research tasks completed herein are as follows:

1. Develop FEA model of garter stitch geometry incorporating SMA model implementation.

2. Experimentally test actuation capabilities of representative knit samples from both a stress-free (shape set) and stressed (non-shape set) configuration.

3. Compare results of FEA model with experimental results for multiple load cases.

Using the described stitch geometry and a garter pattern, a model accounting for contact interactions and complex material behavior is constructed in ABAQUS. Representative loading cases,

namely iso-force thermal cycles and block force tests with controlled force and displacement respectively acting along the wale direction, are investigated using this model. Material properties used in the model are determined experimentally through single-wire isobaric thermal cycles.

Garter-patterned knit samples composed of eight courses and eight wales are constructed of SMA wire using hand-knitting techniques. One sample is heat treated to achieve a stress-free (shape set) knitted state. Both shape set and non-shape set samples are subjected to the same loading test performed in the model, and results are compared with model predictions.

2.1 SMA Constitutive Model

The formulation of the SMA model and relevant equations, described below, were developed by Lagoudas *et al.* [11] using a Gibb's free energy formulation. Hooke's Law, which gives the elastic relation between stress and strain while taking both thermal and transformation effects into account and shown in equation 2.1, is instrumental in describing the elastic and transformation strain response.

$$\boldsymbol{\varepsilon} = \mathbf{S} : \boldsymbol{\sigma} + (T - T_o)\boldsymbol{\alpha} + \boldsymbol{\varepsilon}^t \tag{2.1}$$

Here, S varies as a function of the martensitic volume fraction, ξ, $\boldsymbol{\sigma}$ is the stress tensor, T and T_o are the current and initial temperature of the material, respectively, $\boldsymbol{\alpha}$ is the coefficient of thermal expansion in all directions denoted as a tensor, and finally $\boldsymbol{\varepsilon}^t$ is the current transformation strain for a given ξ and load history.

Evolution of transformation strain is described by equation 2.2 and supported by equations 2.3 and 2.4.

$$\dot{\boldsymbol{\varepsilon}^t} = \dot{\xi}\boldsymbol{\Lambda} \tag{2.2}$$

$$H_{cur} = \begin{cases} H_{min} + (H_{max} - H_{min})(1 - e^{-k(\bar{\sigma} - \sigma_{crit})} & \text{if } \bar{\sigma} > \sigma_{crit} \\ H_{min} & \text{otherwise} \end{cases} \tag{2.3}$$

where H_{min} and H_{max} refer to the minimum and maximum possible amount of transformation strain, respectively, k is a model parameter found empirically, and $\boldsymbol{\sigma}_{crit}$ is the minimum stress for which transformation beyond H_{min} can occur.

$$\boldsymbol{\Lambda} = \begin{cases} \frac{3}{2} H^{cur}(\bar{\sigma}) \frac{\boldsymbol{\sigma'}}{\bar{\sigma}} & \text{for forward} \\ \frac{\boldsymbol{\varepsilon}^{t-r}}{\xi^r} & \text{for reverse} \end{cases} \tag{2.4}$$

where ε^{t-r} and ξ^r are the remembered transformation strain and martensitic volume fraction calculated from the most recent forward transformation, $\boldsymbol{\sigma'}$ is the vector form of deviatoric stress, and $\bar{\sigma}$ is the von Mises stress.

As the Gibbs free energy formulation ensures thermodynamic consistency, the following condition can be derived and used as transformation criteria:

$$\Phi = \begin{cases} \boldsymbol{\sigma} : \boldsymbol{\Lambda} + \frac{1}{2} \boldsymbol{\sigma} : \mathbf{S} : \boldsymbol{\sigma} + \rho \Delta S_o T - (\rho b^M \xi + \mu_1 + \mu_2) - Y & \text{for forward} \\ -\boldsymbol{\sigma} : \boldsymbol{\Lambda} - \frac{1}{2} \boldsymbol{\sigma} : \mathbf{S} : \boldsymbol{\sigma} - \rho \Delta S_o T + (\rho b^A \xi + \mu_1 - \mu_2) - Y & \text{for reverse} \end{cases} \tag{2.5}$$

Equations 2.6 through 2.11 outline parameters necessary to solve for the thermodynamic consistency condition seen in equation 2.5. They are related to changes in entropy and internal energy due to temperature along with the differences of material properties found in an SMA's martensitic and austenitic form. More detail as to their physical meaning can be seen in the work by Lagoudas *et al.* [11].

$$\rho \Delta S_o = -C H_{cur}(\bar{\sigma}) \tag{2.6}$$

where C is the model parameter governing effect of stress on transformation surfaces and ρ is the

density of the SMA being modeled.

$$\rho b^A = -\rho \Delta S_o (A_f - A_s) \tag{2.7}$$

where $\Delta\ S_o$ is the difference in the compliance tensor between an SMA's purely martensitic and austenitic form, and A_s and A_f refer to the temperatures at which an SMA begins and ends transformation into austenite in a zero stress state, respectively.

$$\rho b^M = -\rho \Delta S_o (M_s - M_f) \tag{2.8}$$

where M_s and M_f refer to the temperatures at which an SMA begins and ends transformation into martensite in a zero stress state, respectively.

$$Y = \frac{1}{4}\rho \Delta S_o (M_s + M_f - A_f - A_s) \tag{2.9}$$

$$\mu_1 = \frac{1}{2}\rho \Delta S_o (M_s + A_f) \tag{2.10}$$

$$\mu_2 = \frac{1}{4}\rho \Delta S_o (A_s - A_f - M_f + M_s) \tag{2.11}$$

With these parameters known, equation 2.5 can then be calculated for any given stress, temperature, and martensitic volume fraction and used as transformation criterion; equation 2.12 states

that Φ must be less than zero for any elastic case and equal to zero for any case where the SMA is transforming from one phase to another, indicating that any positive value of Φ is non-physical and if such a value occurs the direction of Φ should be switched.

$$\begin{cases} \Phi < 0 & \text{when } \dot{\xi} = 0 \\ \Phi = 0 & \text{when } \dot{\xi} \neq 0 \end{cases} \tag{2.12}$$

This three-dimensional model is well suited for studying continuum elements, and its implementation as an ABAQUS user-defined subroutine (VUMAT) developed by Solomou is employed in this work and further described in section 2.3.

2.2 ABAQUS/Explicit Formulation

The geometry that enables the large macro-scale deformations through high contact slip mechanisms [34] inherent to the study of knits requires thoughtful modeling considerations. ABAQUS/Explicit is particularly well suited to large, non-linear, quasi-static analyses [35]. This software uses a forward Euler integration technique to solve the equations of motion through time:

$$\mathbf{M}\ddot{\mathbf{u}} = \mathbf{P} - \mathbf{I}, \tag{2.13}$$

where $\mathbf{M}$ is the lumped mass matrix, $\mathbf{P}$ is the external load vector and $\mathbf{I}$ is the internal load vector. By solving for $\ddot{\mathbf{u}}$, nodal accelerations can easily be calculated through time. This method does not require iterations for a solution but requires small time steps for solution accuracy.

2.2.1 Considerations for Analysis Computation Time

The requirement of small time steps for solution accuracy may become infeasible as the time period of analysis increases. An analysis of T seconds, for example, requires N number of incre-

ments of length t, which is found to be [36],

$$t \leq \frac{2}{\omega_{max}}, \tag{2.14}$$

neglecting damping and [37],

$$t \leq \frac{2}{\omega_{max}}(\sqrt{1+\xi^2} - \xi), \tag{2.15}$$

if damping is accounted for, where ω_{max} is the highest eigenvalue in the system and ξ is the fraction of critical damping in the mode with the highest frequency. The total number of increments N required for the analysis is T/t; therefore, efforts to improve computation time must reduce the number of increments, thereby focusing on either increasing increment length, t, or decreasing simulation total time, T.

Load Factoring

The process of load factoring decreases the total simulation time by applying the loads or boundary conditions in a model in a shorter time period than the one used by the actual process [36]. This method is only valid if there are no rate dependencies in the material and the kinetic energy in the model is substantially less than (i.e. less than 5% of) the strain energy. Comparisons with ABAQUS/Standard or convergence studies can be used to determine the minimum possible analysis time.

In this work, analysis time scale was determined iteratively and ultimately chosen to reduce model dynamic instabilities, discussed in appendix C.

Mass Scaling

The most commonly used method of improving analysis time for quasi-static problems is mass scaling. This method relies on the relationship between model density and wave speed to increase time increment length, t. Since it is often not necessary or computationally feasible to compute t exactly, the following reasonable estimate is made based on wave speed (c_d) and characteristic

element length (L^e) [38]:

$$t = \frac{L^e}{c_d}. \tag{2.16}$$

This is the value utilized by ABAQUS/Explicit. A simple estimation of the wave speed for a linear elastic material with a Poisson's ratio of zero is,

$$c_d = \sqrt{\frac{E}{\rho}}, \tag{2.17}$$

indicating that an increase material stiffness causes the time increment to decrease, while an increase in material density increases the time increment. This method is also limited by the comparative value of kinetic energy against strain energy, as the solution of a quasi-static analysis must not become dominated by system inertia.

Mass scaling techniques are employed in this work to improve computation time without affecting analysis results. A comparative study was performed, and ultimately a factor of 10,000 was chosen to scale the material density.

2.2.2 Domain Decomposition

To improve computation time, this work employs an ABAQUS feature called domain decomposition. This feature allows for multiple topological domains to be analyzed simultaneously and independently by multiple processors, subsequently passing relevant information along common boundaries [39]. Eight domains were used for this analysis and chosen using the program's automatic load balancing features which distribute computational processes across processors. The domains chosen through this method are shown in figure 2.1.

2.3 Globally Explicit Implementation of SMA Constitutive Model

The implementation of the SMA constitutive model employed in this work was developed as a user-defined material subroutine for ABAQUS/Explicit in the form of a VUMAT. The VUMAT employs an implicit closest-point projection method for a return mapping algorithm to solve for the stress response resulting from transformation. This algorithm uses a backward Euler integra-

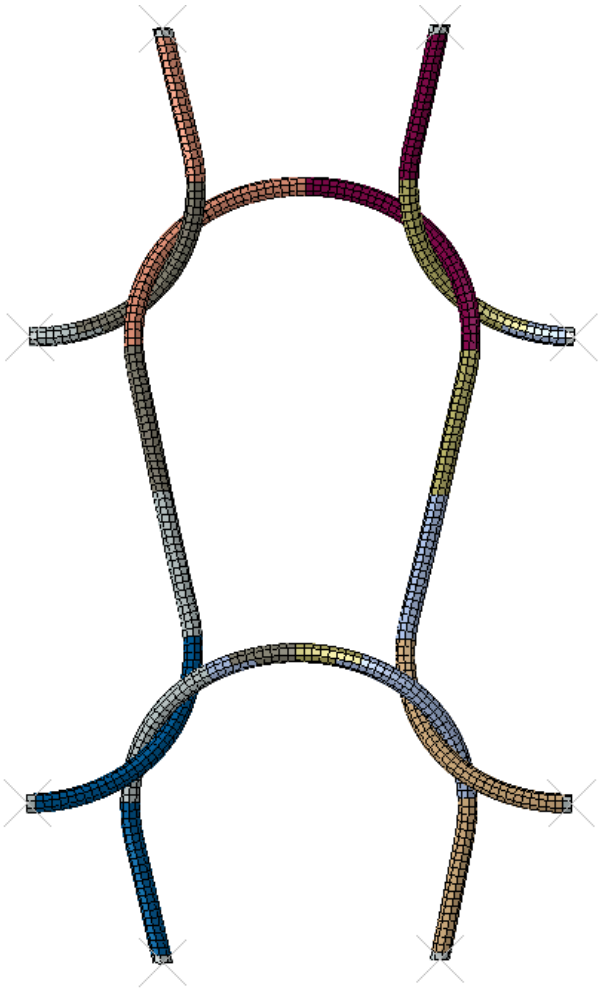

Figure 2.1: Domains utilized in ABAQUS/Explicit analysis.

tion scheme to develop a non-linear algebraic set of equations from the transformation evolution equation that can then be solved using the Newton iteration method [11]. The resulting predictor-corrector scheme that enforces the constitutive relationship of SMAs described in 2.1 is formatted in FORTRAN for compatibility with ABAQUS.

2.4 Contact Formulation

The crux of this problem is the high contact between stitches. The relationships for describing this contact employed by ABAQUS/Explicit is reported herein. The central equation of contact

theory is the contact/penetration condition, shown in equation 2.18 as given by Wriggers *et al.* [40],

$$g_{N+} = \begin{cases} ||\mathbf{x}^1 - \hat{\mathbf{x}}_t^2(\bar{\xi^1}, \bar{\xi^2})|| & \text{for } [\mathbf{x}^1 - \hat{\mathbf{x}}_t^2(\bar{\xi^1}, \bar{\xi^2})] \cdot \bar{\mathbf{n}}^2 < 0 \\ 0 & \text{otherwise} \end{cases}, \tag{2.18}$$

where $\bar{\xi^1}$ and $\bar{\xi^2}$ are natural local shape parameters of the master surface, $\mathbf{x}^1$ and $\mathbf{x}^2$ are position vectors of the slave and master surfaces respectively, and $\bar{\mathbf{n}}^2$ is the outward unit normal from the master surface at the master point. This condition not only serves as a contact verification condition, where $g_{N+} > 0$ is indicative of contact, but $g_{N+} = 0$ represents the classical non-penetration condition. This equation is the fundamental supposition in evaluating contact forces.

2.4.1 Contact Stresses

Contact stresses can be expressed by the vector $\boldsymbol{\sigma} = p_N \bar{\mathbf{n}}^2 + t^i \bar{\mathbf{a}}_i^2$. The normal components are represented by p_N and the tangent components by t^i. The stress vector acts on both surfaces, and by Newton's 3rd law yields $\boldsymbol{\sigma}^1 = -\boldsymbol{\sigma}^2$.

In the normal direction:

If the non-penetration condition is upheld, contact must occur when $g_{N+} = 0$; in this case, p_N must be non-zero. If adhesive stresses are neglected (i.e. simple compressive contact), the Kuhn-Tucker condition for frictionless contact can be stated [40]:

$$g_{N+} \geq 0, \quad p_N \leq 0, \quad g_{N+} p_N = 0\,. \tag{2.19}$$

Experimental formulations have been developed to evaluate p_N as a function of material properties. The simplest of these formulations is the nonlinear constitutive equation developed by Kragelsky *et al.* [41]:

$$p_N = c_N (g_{N+})^n\,. \tag{2.20}$$

Here, c_N and n are material parameters that must be determined experimentally.

In the tangential direction:

A simplified form of the tangential slip function is expressed as:

$$\mathbf{g}_t = \dot{\bar{\xi}}^i \bar{\mathbf{a}}_i^2 \quad \text{for } i = 1, 2\,, \tag{2.21}$$

where $\bar{\mathbf{a}}_i^2$ is a tangent vector along the contact surface and $\dot{\bar{\xi}}^i$ represents a change in shape parameters of the master surface along that vector. In the case of stick, $\mathbf{g}_t = 0$. In the case of sliding friction, Coulomb's law is used:

$$\mathbf{t}_T = -\mu |p_N| \frac{\mathbf{g}_t}{||\mathbf{g}_t||}\,, \tag{2.22}$$

where μ is the frictional coefficient.

2.4.2 Enforcement Methods

Contact is accounted for in the weak form of the boundary value problem as a force applied on the boundary. The forms presented in this report represent the integral forms as seen in the weak formulation of the contact problem.

Hard enforcement

Strict enforcement of the no-penetration condition yields the following formulation for the force as it is included in the weak formulation:

$$\int_{\Gamma_c} (p_N \delta g_{N+} + \mathbf{t}_T \cdot \delta \mathbf{g}_T) dA\,. \tag{2.23}$$

While this represents the most desirable case, it is often challenging and computationally expensive to implement. Models with complex geometry or other properties reach better convergence with less strict methods.

Penalty method

The contact condition that represents the penalty method relaxes the constraints of the hard contact enforcement. In this case, the constraint on g_{N+} is violated and does not equal zero during contact, but a penalty multiplier is applied. The formulations represent the pure stick (tangential)

case,

$$\int_{\Gamma_c} (\epsilon_N g_{N+} \delta g_{N+} + \epsilon_T \mathbf{g}_T \cdot \delta \mathbf{g}_\mathbf{t}) dA, \quad \epsilon_N > 0, \epsilon_T > 0\,, \tag{2.24}$$

where δg_{N+} is associated with the variation of the normal gap, and the slip condition,

$$\int_{\Gamma_c} (\epsilon_N g_{N+} \delta g_{N+} + \mathbf{t}_T \cdot \delta \mathbf{g}_\mathbf{t}) dA, \quad \epsilon_N > 0\,, \tag{2.25}$$

which may or may not account for friction.

Lagrange multiplier

$$\int_{\Gamma_c} (\lambda_N \delta g_{N+} + \boldsymbol{\lambda}_T \cdot \mathbf{g}_T) dA\,, \tag{2.26}$$

The Lagrange multiplier is associated with the contact pressure, i.e. λ_N represents p_N directly. The tangential term is more complex. For a simple case, that is in the case of frictional slip, $\boldsymbol{\lambda}_T \cdot \mathbf{g}_T$ can be simplified to $\mathbf{t}_T \cdot \mathbf{g}_T$.

2.4.3 Considerations for Implementation in FEA

When implemented in finite element analysis, contact often requires special considerations. In early FEA implementations, users needed to define specific elements expected to experience contact [42]. As simulations improved, level of user involvement decreased, and defined contact pairs of parts or surfaces became sufficient [42]. Continued development in this area has led to general contact formulations, where no user input is required to determine contact areas in the model [42]. Most of these advancements are aimed at making contact analyses accessible and simple to non-specialist modelers. An important consideration for FEA implementations of contact develops from part geometry. In particular, FEA solutions are impacted by the need to mesh a part.

Contact Types

Knowing how two objects are expected to intersect each other and what geometry exists at contact points greatly improves convergence behaviors in FEA solvers. The following types of ge-

ometric contact are employed in commercial softwares and can be automatically detected without additional user input.

Surface to Surface:

Surface to surface contact is the primary and most common form of general contact used in FEA solutions. It is also the simplest to implement and offers the fewest issues with convergence. However, some challenges still persist with this type of contact. Surfaces in contact do not always have corresponding meshes; therefore mortar methods must be used to ensure solution accuracy at these surfaces [42]. Convergence can be helped by using smoothing techniques and mesh refinement [43].

Edge to Surface and Edge to Edge:

Edge based contact typically involves a line of nodes contacting either a surface or another line of nodes. Revising the contact discretization method to rely on the line of nodes along the edge in contact rather than a whole surface that is not affected can greatly improve convergence and solution time. When two edges come into contact, it becomes important to consider their orientation with respect to each other. When both edges are parallel (long line of contact), a radial formulation, allowing the contact check to extend radially along the line of nodes, is used. When the edges are not parallel and therefore cross at one or a few number of points, a cross formulation, based on the cross product between the edges, is used to determine contact.

This type of contact can be extended to a vertex to surface formulation, where a single node is the initial contact point.

Geometric Corrections

A significant problem in contact in FEA is overestimation of contact forces due to stress concentrations generated by artificial geometry produced by the mesh. For example, a perfectly cylindrical part will become discretized when meshed, and the resulting edges will impart stress concentrations onto a smooth surface when in contact. To combat this, smoothing techniques and geometry resolutions are utilized [42].

Contact Considerations Employed in This Work

Due to the large motions of the structure and large potential contact area, the continuum element-based, explicit FEA model employed a general contact method, which considers contact over the whole model. This formulation considers all three contact types, though surface-to-surface is the dominating type in this analysis because of the 3D continuum elements utilized. A hard enforcement method was used for contact in the normal direction; simple geometry of the contact surfaces (i.e. cylindrical in the near field) minimized risk of convergence issues with this enforcement method. To develop the tangential contact properties, a comparison between a model accounting for friction and one neglecting friction were considered. The model accounting for friction was significantly more computationally expensive compared with its frictionless counterpart, and in simple simulations results were comparable. However, for more complex simulations such as thermal cycles, friction was critical in damping out vibrations due to loading, and for the subsequent models was therefore included. The friction coefficient employed in this work was 0.2.

2.5 Model Features

2.5.1 Geometric Parameters

Stitch geometry used in this study is defined by four measurable parameters: loop diameter, wire diameter, a wale length parameter, and course height. The values of these geometric parameters were chosen to correspond with the measured values of the experimental sample. Additional parameters, the course height parameter and wale length, were determined using the measured parameters and simple geometric relationships.

Two complete stitches, a knit and a purl, comprise the garter stitch RVE. The knit stitch is split along its medial course-wise axis, forming two separate components: a segment comprised of the needle loop and a segment comprised of the two sinker loops. The needle loop segment of the knit stitch is positioned at the base of the RVE at a 30^{o} rotation out of the front face of the fabric. The purl stitch is positioned at a 30^{o} rotation into the fabric plane such that the needle loop segment of the knit loop, upon a downward translation along the fabric plane, will intersect the sinker loops

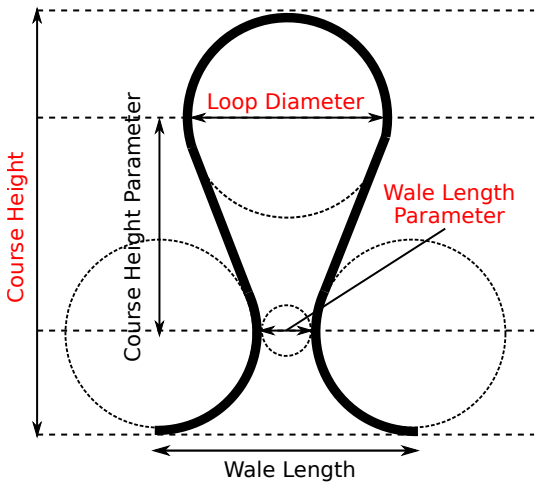

Figure 2.2: Stitch geometry employed in model. Quantities measured from experimental sample are shown in red.

Table 2.1: Geometric parameter values for shape set model.

Bend diameter	0.00395 m
Wire diameter	0.0003 m
Course height parameter	0.00412 m
Wale length parameter	0.00226 m
Course height	0.00867 m
Wale length	0.00621 m

of the purl stitch. The sinker loop segment of the knit stitch is positioned at the upper surface of the RVE at a 30^o rotation out of the front face of the fabric such that an upward translation of this segment along the fabric plane brings the sinker loops of this segment into contact with the needle loop of the purl stitch. The initial RVE geometry is shown in figure 2.3.

2.5.2 Application of Periodic Boundary Conditions

For this representative unit of a large fabric, boundary conditions were carefully considered to represent continuous fabric response away from fabric ends. To achieve a response that replicates the linked behavior of stitches, periodic boundary conditions were employed. These conditions were formed by applying an equation-based constraint such that motion of one point resulted in the opposite motion of the linked point, as would be seen in uniaxial stretching (both horizontally and

Table 2.2: Geometric parameter values for non-shape set model.

Bend diameter	0.00437 m
Wire diameter	0.0003 m
Course height parameter	0.00296 m
Wale length parameter	0.00348 m
Course height	0.00793 m
Wale length	0.00785 m

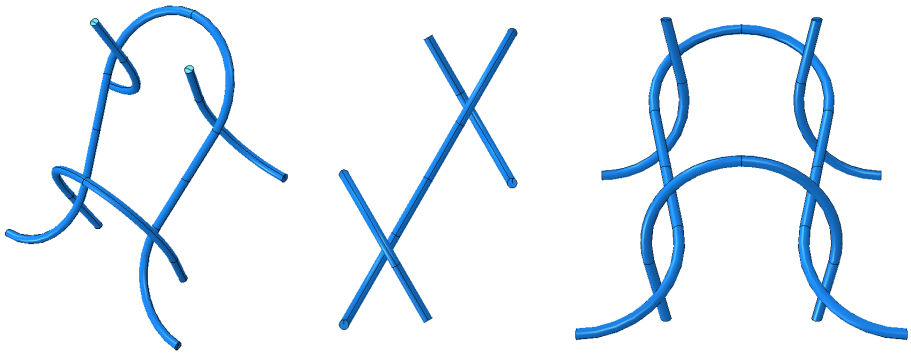

(a) Isometric view. (b) Side view. (c) Front view.

Figure 2.3: Initial 3D geometry of a shape set garter stitch before deformation.

vertically) of a fabric. This motion is controlled by forces and displacements applied to a reference point included in the constraint equations. Figure 2.4 shows regions where these conditions were applied; circles of the same color indicate linkage via condition equation. The equations applied to the node pairs have the following form:

$$u_1^i - u_2^i = u_{RP}^i \quad \text{for} \quad \text{controlled directions}$$

$$u_1^i = u_2^i \quad \text{for} \quad \text{uncontrolled directions}$$

Here, u_1^i represents displacement or rotation of the first node in a node pair where i is the direction. Controlled direction is wale-wise for red and pink indicators shown in figure 2.4 and course-wise for green and blue indicators. Uncontrolled directions are all other translations and rotations at

these points, and u^i_{RP} represents the displacement of the reference point. In this way, displacements of node pairs are linked and controlled through a reference point, while their rotations are linked such that wire ends (which represent a connection to another stitch) remain parallel to their paired wire end. In the simulation, these conditions were applied through discrete rigid surfaces

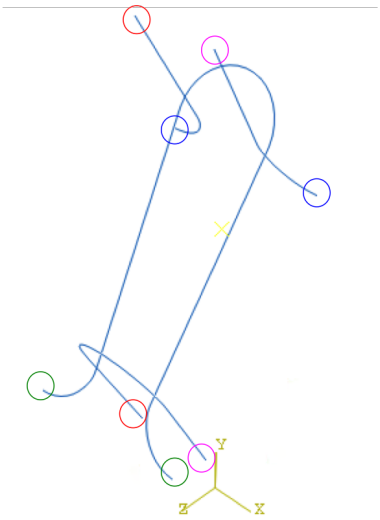

Figure 2.4: Periodic boundary conditions link stitch ends to simulate a continuous fabric. Circles of corresponding colors represent a constrained pair.

connected to ends of wires. Constraint equations governed the motion of reference points on the discrete surfaces, which enforced continuity between deformable, periodically linked stitch ends. This method of enforcing periodic boundary conditions was superior to individual node-based linking methods, which resulted in excess stress concentrations that were not representative of fabric behavior.

2.5.3 Mesh Parameters and Convergence Study

The model was meshed using continuum solid hexahedral elements. The element type chosen for this simulation was C3D8I, denoting a 3-D, 8-noded incompatible mode element. This element type was chosen for its good performance in benchmarking bending problems [44] compared with its C3D8 counterpart, as the incompatible mode feature reduces problems related to

shear-locking and improves bending performance. Beam elements were initially considered for this problem. Ultimately, however, this element type was inconsistent with the existing material model implementation and continuum elements were used instead.

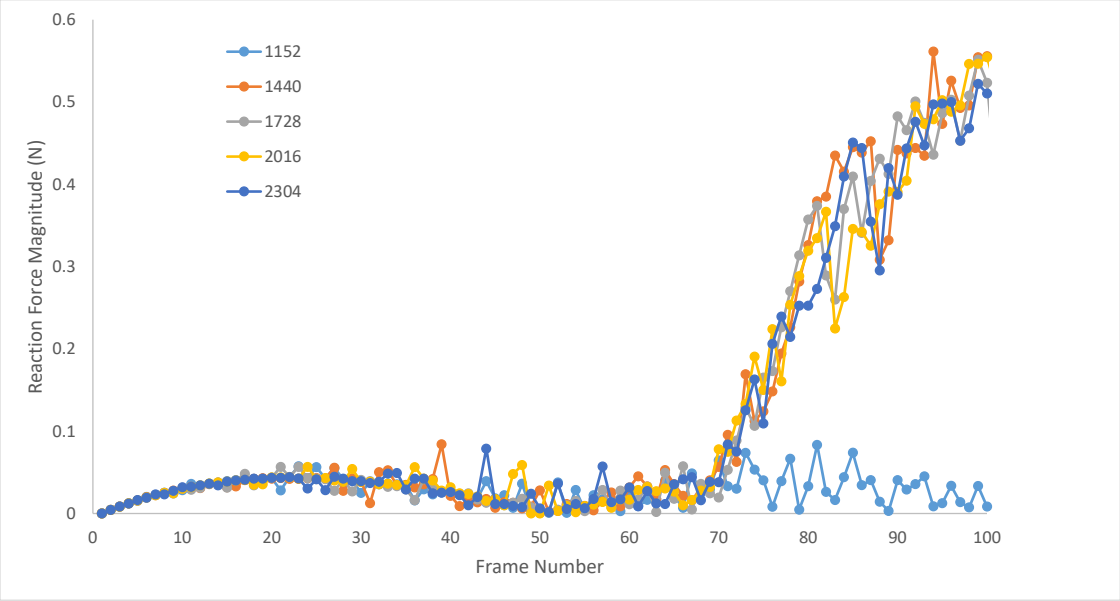

Figure 2.5: Mesh convergence study. Magnitude of reaction force plotted at each frame number for runs with 1152, 1440, 1728, 2016, and 2304 elements.

A mesh convergence study was performed to determine an appropriate mesh size. Five mesh sizes, ranging from 1152 to 2304 elements, were considered in a simple simulation in which the RVE was stretched to an arbitrary prescribed length. For the model with 1152 elements, elements were too large to engage contact. Convergence is achieved for models with 1440 elements or greater. Figure 2.5 shows the reaction force at a given frame in the solution. Large variations indicating potential model instability can be seen in this figure, and these are further discussed in appendix C. Simulations carried out in this work used 1664 elements.

2.5.4 Model Adjustments for Non-Shape Set Knit Structures

The non-shape set knit structures differ from their shape set counter parts in that the stresses incurred through the knitting process are retained in the structure and not alleviated by a heat treat-

ment. In the shape set analyses, the stress-free initial structure is easily obtained through controlled geometry input. In the non-shape set analysis, however, the initial stress state must be accounted for. Therefore, an analysis must be run to simulate knitting the structure to obtain the initial stress state. In the experimental sample, the fully martensitic material de-twins to accommodate the stresses associated with knitting. Because the de-twinning phenomenon is not accounted for in the SMA constitutive model, however, the initial stress state is determined using an austenitic wire model that transforms to martensite with sufficient stress. This stress state is likely more similar to the de-twinned stress state than a fully elastic analysis performed in martensite; in addition, upon heating of the experimental sample, the de-twinned, high stress regions of the knit loops are likely to either remain in martensite or easily transform due to increased stress upon subsequent loading. Therefore, the loaded and hot configuration of the model as described is likely similar in stress and martensitic volume fraction to the real world implementation of this structure.

The knitting process was simulated using semi-circular analytical surfaces that push an initially straight wire segment composed of 1664 continuum elements to form the prescribed geometry of a single stitch. The initial wire configuration and the surfaces used to form the stitch geometry in this analysis are shown in figure 2.6a. The resulting stress state and material model state variables are used in subsequent analyses for the non-shape set wire. The initial stress state resulting from forming the stitch is depicted in figure 2.6b, and the martensitic volume fraction of the stitch is shown in figure 2.6c. It can be seen that stress-induced transformation does occur at some regions of the needle and sinker loops.

Three instances of this stitch with relevant stress and transformation information are then placed to form an extended (i.e. three whole stitches) version of the garter RVE. Internal surfaces are created at the course-wise mid-plane of the top and bottom stitch (both knit stitches) and tied to rigid analytical surfaces. Figure 2.7 shows this extended RVE configuration. Due to the location of the smaller diameter surfaces through the legs of the knit stitches, data is taken only from the true (i.e. not extended) RVE region. Reference points on these surfaces coupled with a controlling reference point form the periodic connections described in section 2.5.2. The iso-force and block

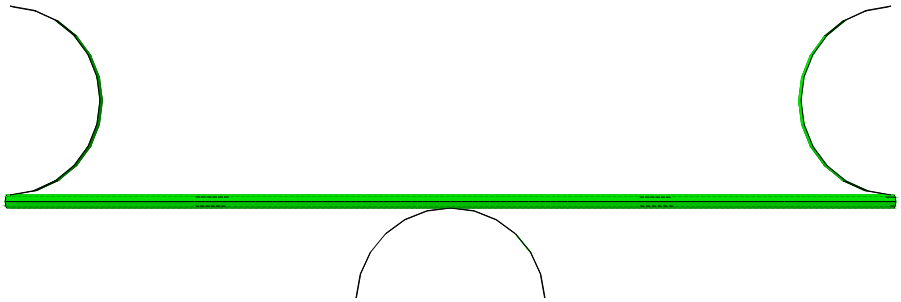

(a) Initial wire configuration before forming process. Surfaces used in stitch forming shown.

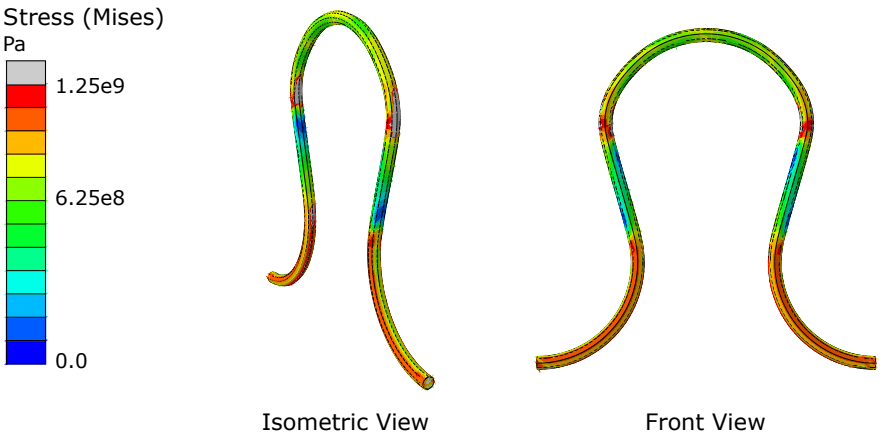

(b) Stress state resulting from forming process.

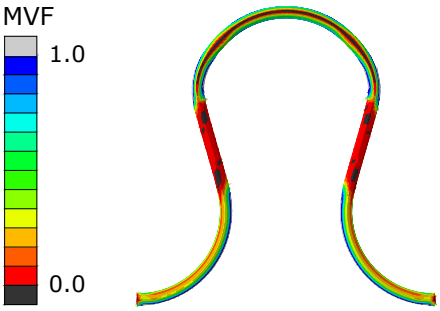

(c) Martensitic volume fraction resulting from forming process.

Figure 2.6: Results of the non-shape set forming analysis.

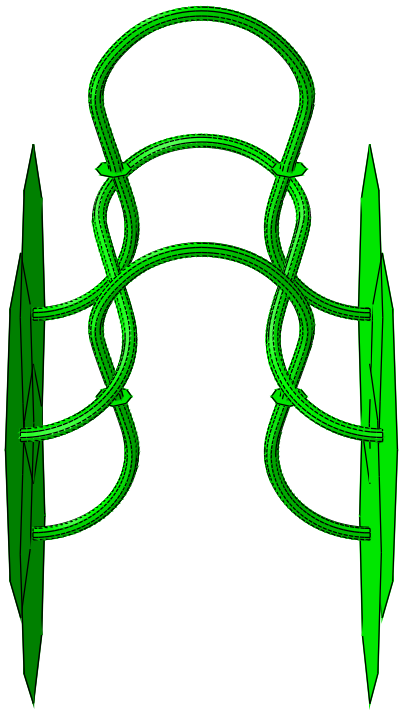

Figure 2.7: Initial RVE geometry of non-shape set wire shown with surfaces tied to maintain contact between sinker loops and needle loops of stitches.

force analyses can then be performed from this new reference state.

2.6 Representative Load Case Simulations for Shape Set Wire

Analyses performed were designed to replicate the experimental load cases as closely as possible; material properties used in this analysis were found experimentally and are described in section 3.1.3. Due to the expensive nature of the knitting problem, the analyses performed in this work utilized the restart capability of ABAQUS/Explicit to avoid repeatedly solving aspects of the simulations that were common to all runs. The flow of analyses performed is described by figure 2.8. Two wale-length constraint conditions were studied for all load cases. In the unconstrained condition, wale length is allowed to shorten as the RVE is loaded; minimum wale length is enforced through geometric constraints, i.e. sinker loops are prevented from sliding fully through the needle loop. In the constrained configuration, wale length is fixed at the initial value, prohibiting significant structural displacement of the RVE. These two constraint cases serve to highlight the

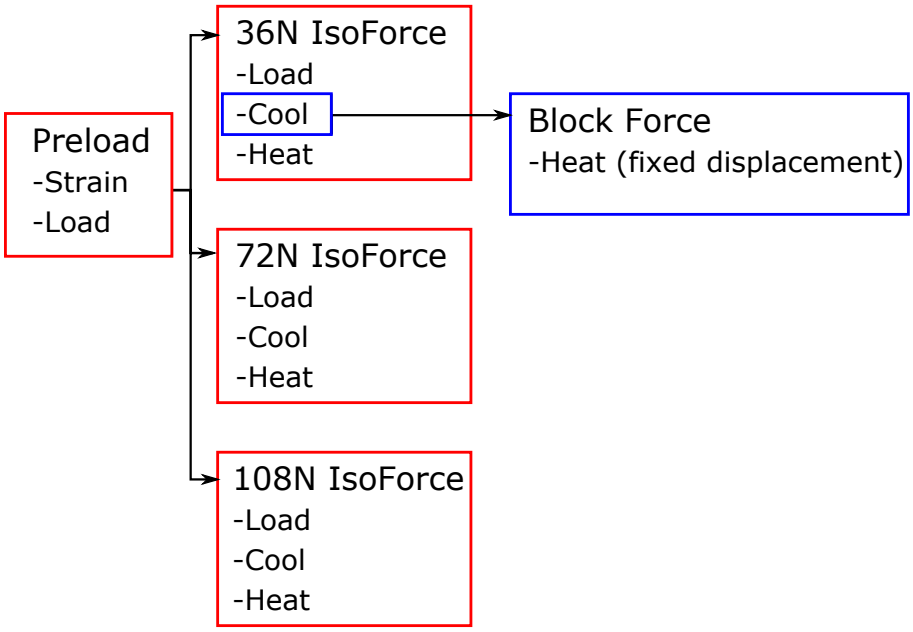

Figure 2.8: Flow chart showing hierarchy of restart jobs for the shape set knit.

change in displacement generated due to structural advantages and the change in displacement due only to transformation.

2.6.1 Pre-Load

The garter stitch geometry was modeled in ABAQUS as described in section 2.5.1. This initial geometry, unlike a physical knitted structure, does not contain any surfaces in contact. Therefore, it is necessary to initialize a state that is representative of a knit structure under no or very light load. A pre-loading analysis was performed and utilized as the initial state (via the restart function of ABAQUS) for each subsequent analysis. In the pre-load state, the controlling reference point is displaced such that the knit stitch segments of the RVE just come into contact with the purl stitch. A second step then applies a load to the controlling reference point of 0.5625 N, the analog of 12.5 MPa through the legs of the stitch. All iso-force and block force analyses are initialized from this pre-loaded state.

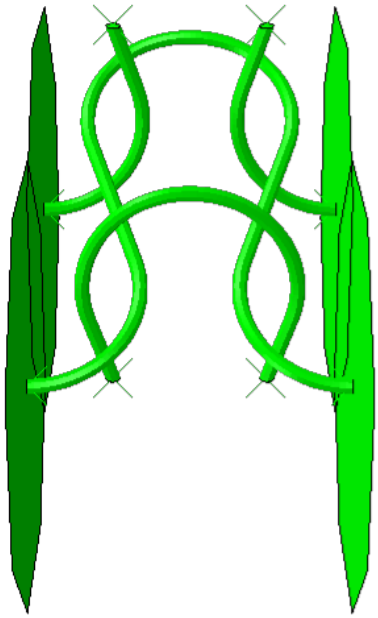

Figure 2.9: Initial RVE geometry of shape set wire shown with surfaces tied to maintain contact between sinker loops and needle loops of stitches.

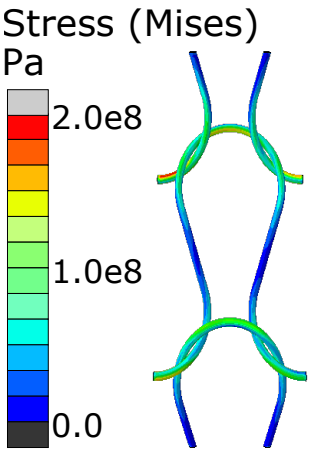

Figure 2.10: RVE configuration in the pre-loaded state. Contours represent Mises stress in Pa.

2.6.2 Iso-Force Analyses and Results

In the iso-force analyses performed, temperature was initially set to 167°C (440 K) to ensure a completely austenite state. A prescribed load was then applied to the controlling reference point over one time step and held for one time step. The load was then held constant as the temperature is reduced to 57°C (330 K) over one time step and held for another before heating again to 167°C

(440 K) over one time step and held for another. This test was performed for a sequence of increasing loads, beginning from 4.5 N per stitch (equivalent to 36 N applied to a fabric of eight stitches per course), which is representative of each stitch leg bearing 100 MPa, and increasing incrementally to 13.5 N per stitch, which is representative of each stitch leg bearing 300 MPa.

Results

A comparison of the results of the six analyses performed for the iso-force thermal cycles of the shape set RVE is presented in this section. None of the curves exhibit smooth forward transformation. Reverse transformation exhibited increased smoothness, especially for the constrained cases.

Figure 2.11 depicts the normalized displacement of a single RVE as temperature is cycled, where the length of the RVE is normalized by the value of the RVE length at initial extension before temperature is cycled. The magnitude of displacement due to transformation of the constrained models is considerably lower than that of the unconstrained. This is an obvious effect of constraining the allowed structural displacement. The constrained models all exhibit similar transformation-induced displacement magnitudes despite variation in load, indicating that structural displacement is a major contributing factor to percent length during transformation compared with initial loading. This idea is further exhibited in the unconstrained models, where the analysis performed at the lowest load experiences the most normalized displacement during transformation. The structural extension due to only initial loading is the least at the lowest load case; since there is still structural displacement that is allowed in this state, the coupling between structural displacement and transformation displacement then allows this load case to increase its original length by a higher percentage than the analyses performed under higher loads. As the load increases toward the load at which the maximum structural displacement is achieved upon initial loading, the structural displacement during transformation decreases, driving the extension due to transformation toward a constant value.

Figure 2.12 shows the geometry of the unconstrained RVE overlaid with a Mises stress contour at key points in the transformation cycle for the lowest applied load case. The difference in

structural displacement between the unloaded initial state and the loaded initial state is apparent from the geometry. The difference in the geometry of the cooled state is even more stark, and how displacement would be generated due to geometric deformation can be clearly seen, as the radius of curvature of all loops has decreased significantly, effectively increasing the length of the legs of the stitches. As expected, the loops experience the highest stresses in the RVE while the stitch legs experience the lowest.

Figure 2.13 shows the geometry of the unconstrained RVE overlaid with a contour indicating martensitic volume fraction for the same load case. The RVE is shown to start in austenite, remain fully in austenite upon loading, and transform fully to martensite upon cooling. Notably, however, full reverse transformation is not achieved upon heating, and significant portions of the needle and sinker loops remain martensitic. This accounts for the unrecovered transformation displacement exhibited by all models. As the structural displacement increases during transformation and the radius of curvature of each of the loops reduces, the stress increases in these regions, seen in figure 2.12, driving the temperature required to induce transformation higher. Therefore, the temperature of the RVE at the beginning of the analysis is no longer sufficient to fully transform the material. Further heating would result in full transformation provided that the geometric deformations are such that the forces due to transformation in the loops are sufficient to recover the initial geometry. It is possible that the geometry change may render this recovery impossible for certain load cases.

Figure 2.14 shows the geometry of the constrained RVE overlaid with a Mises stress contour at key points in the transformation cycle for the lowest applied load case. Compared with the unconstrained geometry at these points shown in figure 2.12, significantly less structural displacement is seen at all states. Additionally, significantly smaller regions of the needle and sinker loops of each stitch saw high stresses after cooling, and these stresses were of a lesser magnitude than those seen by the unconstrained cases. Upon heating, a configuration very similar to that of the initial load is exhibited.

The martensitic volume fraction contour indicates that in fact, more regions fully recovered into austenite for the constrained case than the unconstrained case. This is directly attributed to the

smaller regions of stress concentrations exhibited in the constrained case. For the same temperature cycle, the constrained case recovered considerably more displacement generated due to transformation than the unconstrained case did, and only a slight increase in cycle finish temperature would yield full recovery for this model. Figure 2.15 depicts the geometry of the constrained case loaded at the lowest value with a contour representing martensitic volume fraction for key points in the load cycle. While the fully heated RVE appears to be fully austenitic, some martensite remains at points of contact.

As discussed, smooth transformation is not achieved during any model run, particularly in cooling. This is likely due to the coupling of contact, stress, and transformation; as elements slide past each other (a result of transformation) in contact, the stress experienced by that element may quickly decrease as contact is lost, potentially inducing transformation in that element and thereby generating transformation strain. Because the unconstrained models allow considerably more inter-element sliding, this mechanism of non-smooth extension occurs more frequently throughout the cooling cycle. Figure 2.16 shows the constrained model at frames preceding and at the point where this discontinuity occurs. In the pre-event frame, the sinker loops of the upper knit stitch and the needle loop of the middle purl stitch are not fully transformed. In the event frame, the decreased radius of curvature at the bends indicates some slip has occurred; simultaneously, these bends have transformed into martensite.

2.6.3 Block Force Analysis

In a typical block force test, a prescribed displacement is imparted on the sample; a thermal cycle then induces actuation, and the resulting maximum force generated is the blocking force. The block force analysis performed developed the prescribed displacement from the corresponding iso-force analysis. Since it is advantageous to initialize both an experiment and a modeled simulation involving SMAs from the austenite parent phase, the simulation began at high temperature. The controlling reference point was then loaded to 4.5 N as in the iso-force analysis and the RVE was cooled to 57°C (330 K). The displacement of the controlling reference node was then fixed in this position as the RVE was heated to 167°C (440 K). Because the prescribed displacement was

developed from the iso-force analysis, this analysis utilized the restart function of ABAQUS and restarted from the fully cooled increment of the iso-force test performed using a load of 4.5 N. Output force was measured as a sum of the applied force and the reaction force imparted due to transformation.

Results

As expected, the constrained model generated more force than the unconstrained model upon heating. The constrained model generated 64.4 N of force while the unconstrained model generated 23.6 N of force for one RVE at the temperature of 167^{o}C. Neither model achieved the maximum possible force, and additional heating could generate still more force. The slope of the unconstrained model, however, indicates that it was approaching its peak force production at the temperature at which the analysis ended. As in the iso-force results, contact interactions and element sliding are present, preventing complete smoothness.

2.7 Representative Load Case Simulations for Non-Shape Set Wire

Analyses performed to model the behavior of non-shape set wire were initialized from the non-zero stress and internal variable state obtained through the stitch forming procedure described in section 2.5.4. In a similar way to the shape set simulations, the restart capability of ABAQUS/Explicit was utilized to reduce computation time. The order of restarted analyses is shown in figure 2.18. Simulations for each representative load case were performed using both a constrained and unconstrained wale length. Material parameters were determined experimentally and are described in section 3.1.3.

2.7.1 Prestrain

A displacement analysis was performed to initiate contact between the stitches in the RVE. No mechanical load was applied during this analysis. The initial stress state applied to each stitch caused a distinct flattening of the stitch geometry, inhibited by contact forces of connecting stitches,

2.7.2 Iso-Force Analyses and Results

The extended RVE was studied under thermal cycles performed with a constant load applied to the controlling reference point. Temperature was initially set to be 147°C (420 K); load was then applied over the length of one time step. The RVE was then cooled to 42°C (315 K) over one time step and subsequently heated to 147°C (420 K) again over one time step.This analysis was performed for three constant loads: 4.5 N, 9.0 N, and 13.5 N. These correspond to values of 36 N, 72 N, and 108 N respectively for a sample comprised of eight wales for an approximate comparison to 100 MPa, 200 MPa, and 300 MPa values of stress in the stitch legs.

Results

The iso-force analyses of the non-shape set model behave differently than those of the shape set model, particularly with respect to reverse transformation. As in the shape set model, forward transformation is not smooth. Reverse transformation does not result in a significant recovery of displacement generated during forward transformation despite evidence of martensite transforming into austenite in the stitch legs. This may be due to an inability to recover geometric deformations, i.e. insufficient forces to recovery geometry were present during transformation. This may also be a result of interference from the extended sections of the RVE, which were not constrained properly, or may result from some other analysis inaccuracy. Possible reasons and solutions for the lack of reverse transformation are still being investigated.

Normalized displacement results for all unconstrained and constrained iso-force analyses of the non-shape set model are shown in figure 2.19. As in the unconstrained shape set structure, percent length due to thermal cycling decreases with increased loading; however, in the non-shape set structure, this decline is far more severe. This may be due to the high stress initial state applied to these analyses; as the RVE is loaded before thermal cycling, it becomes more likely to transform into martensite through stress-induced transformation. As the load level increases, more martensite is likely to form due to this phenomenon. Upon cooling, these already transformed sections are not available to generate transformation strain as they have already transformed. Therefore,

displacement due to transformation declines with increasing load. The constrained non-shape set results also indicate a decline in percent length in the cool state as load increases, and unlike the shape set results, the constrained 108 N run outperforms its unconstrained counterpart. (A 72 N run was not performed due to limits on computing resources.) This change in performance during thermal cycling under high loads is likely due to the fact that the unconstrained models transform more during loading than the constrained models; therefore, the constrained models are able to generate more martensite upon cooling.

As described above, wale length was allowed to decrease to enable maximum structural extension in the unconstrained analyses. Figures 2.20 and 2.21 show the geometry of the RVE section of the extended RVE overlaid with Mises stress and martensitic volume fraction contours. Certain regions in the bends experience very high stresses above 2 GPa, but these are excluded here for clarity of the contour. As expected, stresses remain highest in the loop segments of the stitch. Upon reverse transformation, the stitch legs are greatly relaxed in stress while the bends remain stressed. In fact, an additional heating analysis was performed on this configuration to induce additional transformation; however, no further displacement was recovered and the loops only increased in stressed, indicating some binding mechanism inhibiting motion of the geometry. A possibility for this mechanism could be the sever over-stressing of the loops, preventing any recovery of the original geometry of this analysis. Comparing the geometries of the fully cooled and fully heated RVEs, the general shape is observed to be similar and minimal if any lengthwise contraction is apparent. The wale-wise distance between sinker loops has increased in the heated configuration and stress has greatly increased in the loops at this point, indicating that due to geometry, forces were insufficient to significantly recover geometry and manifested as high stress regions instead. Importantly, unlike the shape set samples, martensite is clearly present in the initial configuration of this analysis. Upon cooling, the sample is fully transformed into martensite. Loop regions contain higher concentrations of martensite after heating than in the loaded configuration.

The geometry resulting from the constrained analysis under a 36 N load is shown in figures 2.22 and 2.23, overlaid with a stress and martensitic volume fraction contour respectively. From

figure 2.19, the constrained configuration is shown to recover small amounts of displacement, not experiencing the binding phenomenon of the unconstrained analyses. Due to the constrained wale length, high stress regions appear at contact points between needle and sinker loops, i.e. there are two high stress regions in the needle loops separated by a region of lower stress, unlike the unconstrained model which has a continuous high stress region across each needle loop. This separation of high stress regions allows the center portion of each needle loop to reverse transform upon heating, unlike the unconstrained analyses which saw almost no transformation in loop bends. However, much like the unconstrained analyses, significant geometric recovery is not achieved.

2.7.3 Block Force Analysis and Results

The block force analyses of the non-shape set knit structure were performed for both unconstrained and constrained configurations and were restarted from the cooled state of the respective 36 N iso-force analyses. In the cooled state, the displacement was fixed in the wale-wise direction. The extended RVE was then heated and force output was measured as a summation of the applied force and the reaction force of the RVE (not extended RVE).

Results

Results of the block force analysis of the non-shape set structure are depicted in figure 2.17. As expected, the constrained model outputs more force than the unconstrained model. However, the unconstrained model only barely increases force output as temperature increases. This may result from a similar binding effect experienced by the unconstrained iso-force analyses, where transformation forces were insufficient to induce significant geometry change. Since geometric deformation is a large contributor to displacement during transformation, one can reasonably expect that geometric recovery upon reverse transformation would impart the most force during a block force test. Very little geometric recovery occurred in the unconstrained block force analysis, much like the unconstrained iso-force analysis performed at the lowest force. Therefore, very little actuation force was produced and can all be attributed to material transformation in the stitch legs. The constrained model produced considerably more force. However, force is imparted almost

immediately, possibly indicating that the sample was insufficiently cooled into a fully martensitic state before the block force analysis. Further investigation showed an average martensitic volume fraction of 0.97 before heating, confirming that further cooling was needed for full transformation. The unconstrained model also suffered from insufficient cooling.

2.7.4 Discussion

Non-shape set structures experienced higher stresses (due to the initial stress state) and more stress induced transformation upon loading that shape set counterparts. This contributed to more geometric deformation and less recovery at lower loads. At higher loads, displacement during transformation of non-shape set structures was dominated by transformation in stitch legs.

Non-shape set structures were also shown to produce less force during block force analyses than shape set structures. In both shape set and non-shape set structures, constrained analyses produced more force than unconstrained analyses. Therefore, shape setting a knit fabric and applying constraining boundary conditions tend to increase the amount of force produced upon actuation.

Challenges with these various analyses may negatively impact model comparison against experimental results and impact future work using the approaches laid out in this work. Firstly, the VUMAT implementation of the SMA model was very time intensive, rendering all model runs very computationally expensive (on the order of 100 hours). Secondly, less computationally expensive frictionless models experienced instabilities, causing fluctuations in displacement during transformation; models employing friction did not experience these issues. Moreover, the non-shape set analyses added an additional layer of complexity over the shape set analyses with mapping the initial material state onto the stitches in the RVE. This additional mapping procedure could only be carried out by running the analysis from the ABAQUS input file directly, which is more complicated than the scripting method employed in the other analyses. As a result, not only was the geometry present in the non-shape set analyses extended (though data was only taken from sections within the original RVE geometry), regions of the extended geometry were not properly constrained and may have interfered with model results. Another consequence of this added complexity is shown in figure 2.24. The initial state of the non-shape set stitch was determined through

a forming analysis designed to simulate the knitting process, and these results were mapped to a prestrain analysis to form the extended RVE. Stress state and values of internal variables remained identical in the prestrain analysis to those of the forming analysis. However, strain values differed greatly as a result of this mapping. Figure 2.24a shows the maximum principal strain contour on the stitch at the end of the forming analysis. Figure 2.24b shows the same contour on the extended RVE at the initial state of the prestrain analysis. The contour on each stitch in the initial state of the prestrain analysis should be identical to the one shown in figure 2.24b. It is, however, not remotely similar. This disparity is due to the rotations each stitch instance is subjected to in building the extended RVE; the reference frame is updated in this analysis. It is possible that the analyses performed in this work are not affected by this disparity, as the VUMAT only sees local strain increments and would potentially not see these large strain values. However, additional work is needed to confirm the results presented in this paper are in fact unaffected by these large strain values.

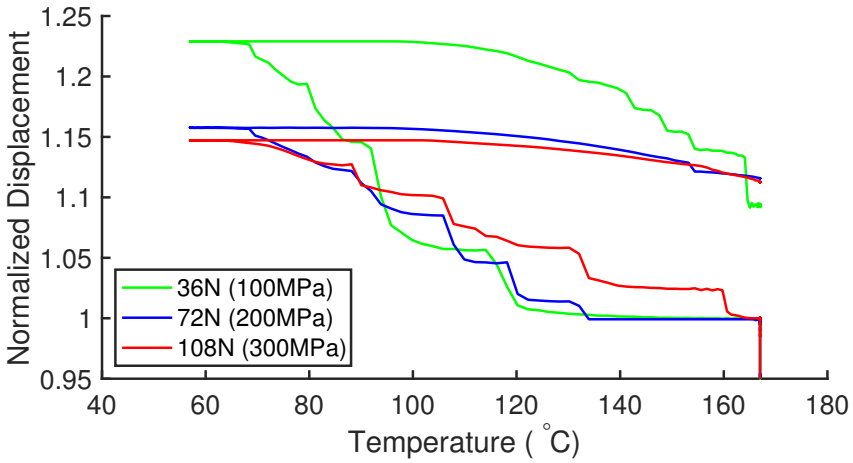

(a) Unconstrained results.

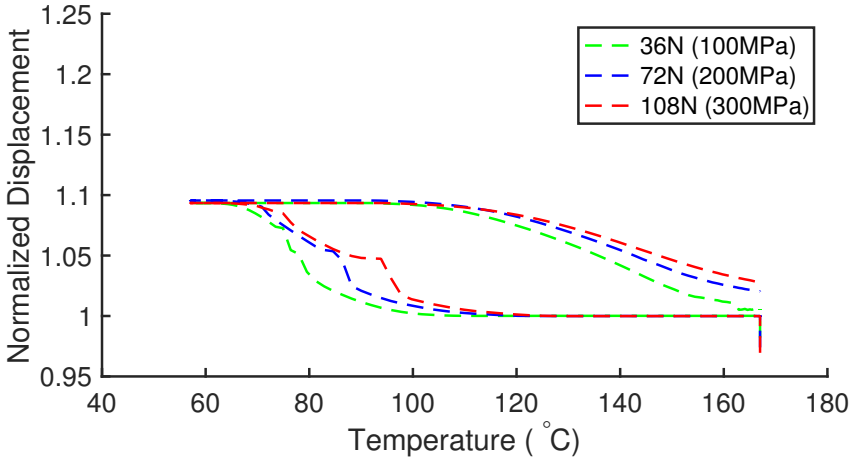

(b) Constrained results.

Figure 2.11: Normalized displacement plotted against temperature for both constraint conditions at three constant loads for the shape set model. Legend represents sample load with nominal stress experienced in stitch legs in parentheses.

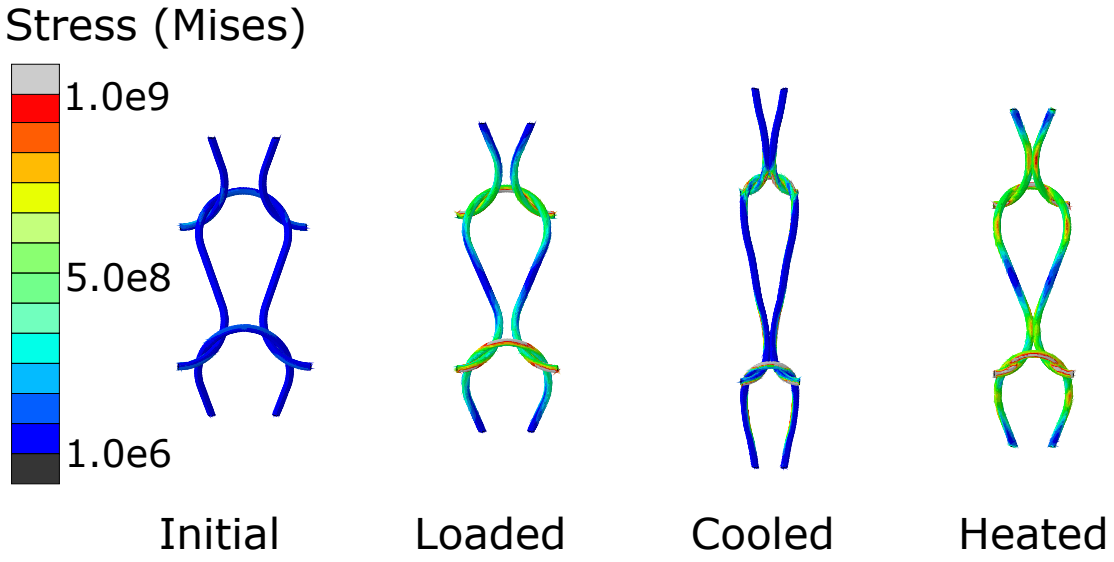

Figure 2.12: Mises stress of the shape set garter RVE under 36 N uniaxial load at key points in iso-force thermal cycle. Wale length is not constrained; true uniaxial load case modeled.

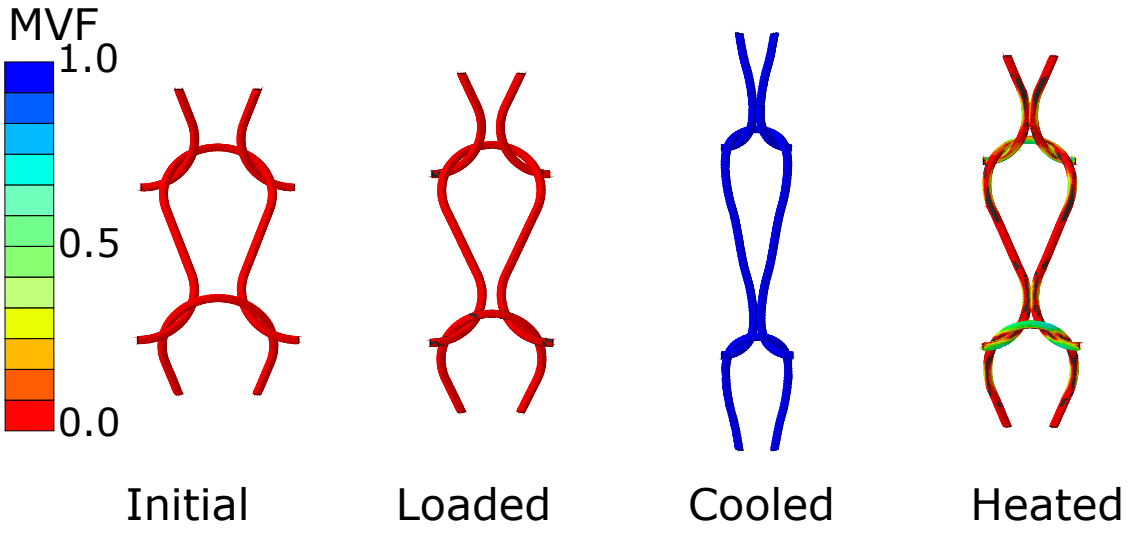

Figure 2.13: Martensitic volume fraction of the shape set garter RVE under 36 N uniaxial load at key points in iso-force thermal cycle. Wale length is not constrained; true uniaxial load case modeled.

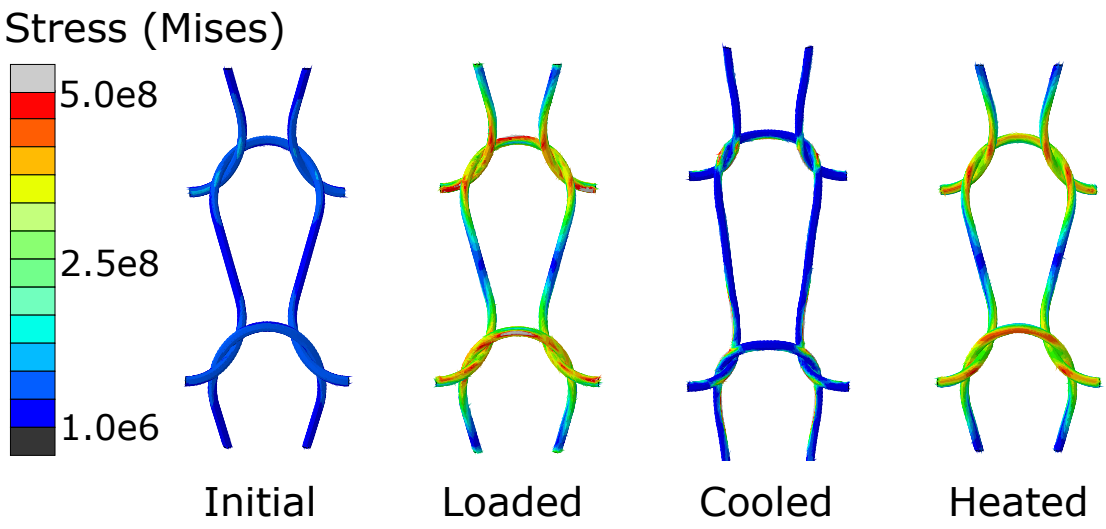

Figure 2.14: Mises stress of the shape set garter RVE under 36 N uniaxial load at key points in iso-force thermal cycle. Wale length is constrained.

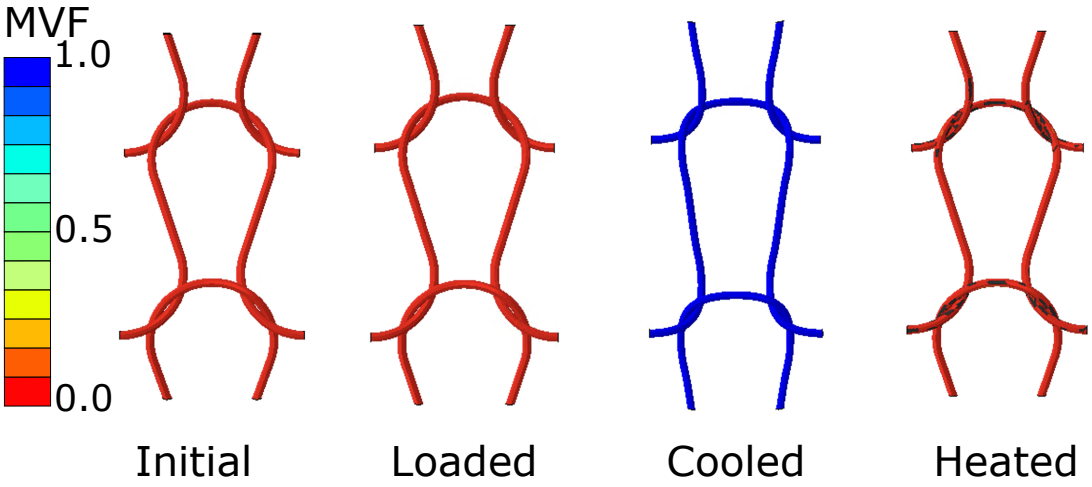

Figure 2.15: Martensitic volume fraction of the shape set garter RVE under 36 N uniaxial load at key points in iso-force thermal cycle. Wale length is constrained.

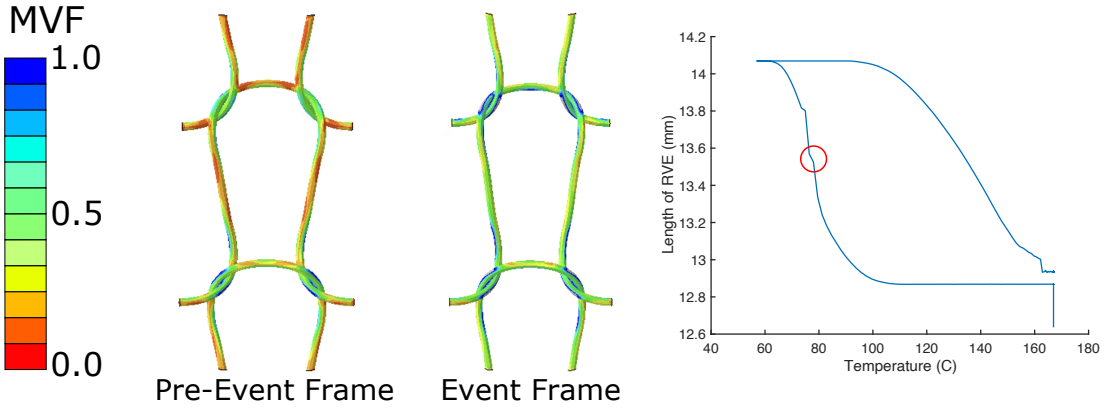

Figure 2.16: Shape set RVE geometry at frames of interest. MVF shown as contour.

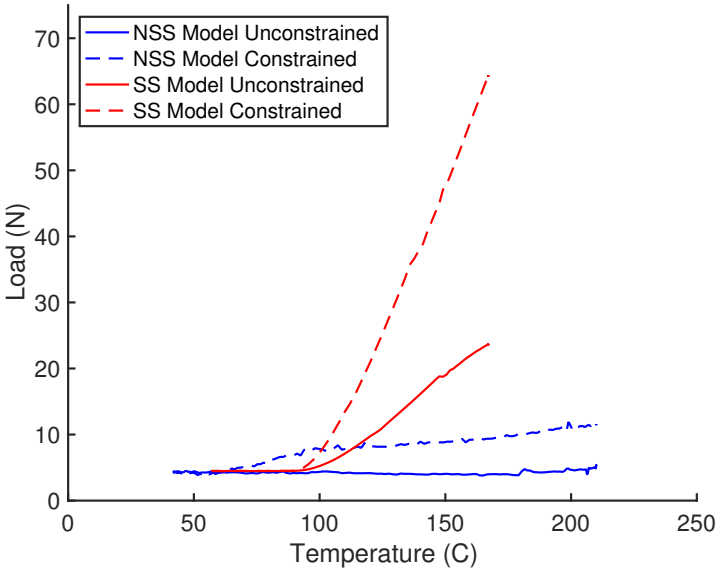

Figure 2.17: Block force results from unconstrained and constrained analyses for shape set (SS) and non-shape set (NSS) models.

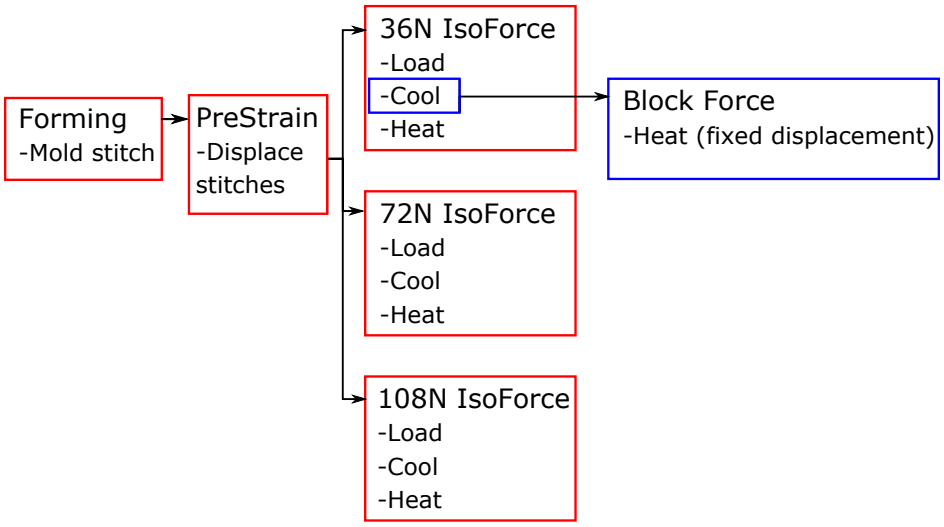

Figure 2.18: Flow chart showing hierarchy of restart jobs for the non-shape set knit.

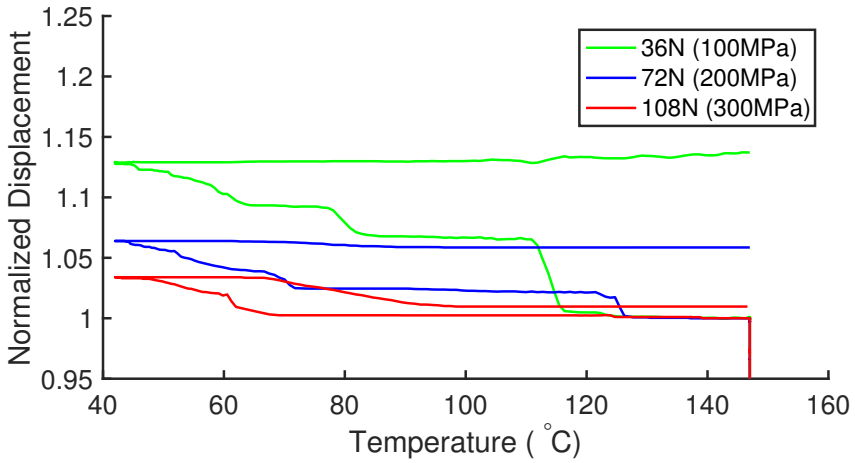

(a) Unconstrained results.

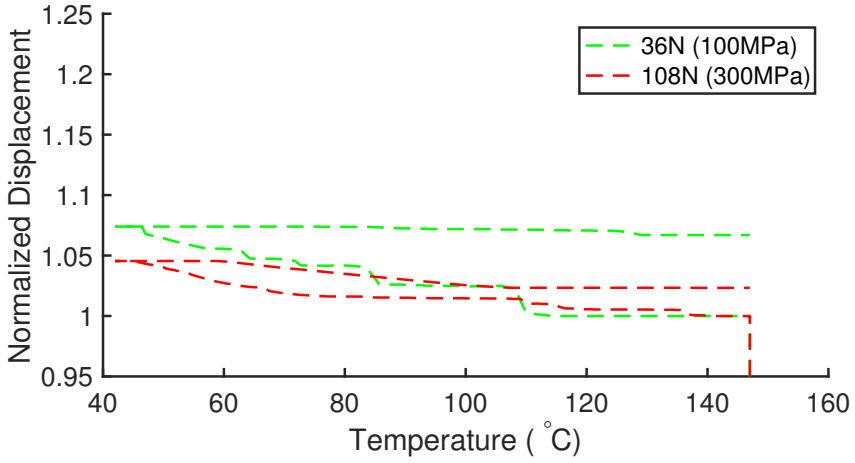

(b) Constrained results.

Figure 2.19: Normalized displacement plotted against temperature for both constraint conditions at three constant loads for the non-shape set model. Legend represents sample load with nominal stress experienced in stitch legs in parentheses.

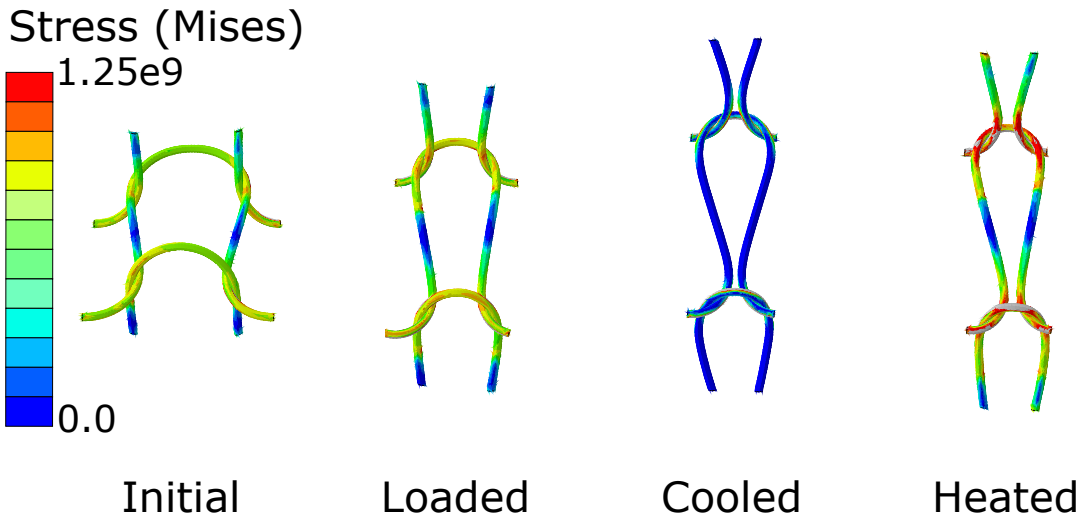

Figure 2.20: Mises stress of the shape set garter RVE under 36 N uniaxial load at key points in iso-force thermal cycle. Wale length is not constrained; true uniaxial load case modeled.

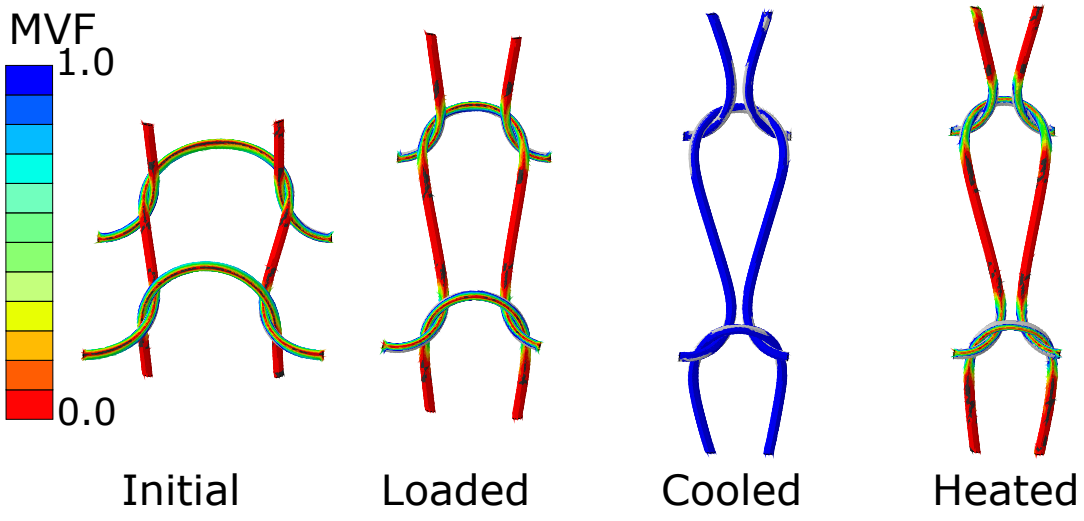

Figure 2.21: Martensitic volume fraction of the shape set garter RVE under 36 N uniaxial load at key points in iso-force thermal cycle. Wale length is not constrained; true uniaxial load case modeled.

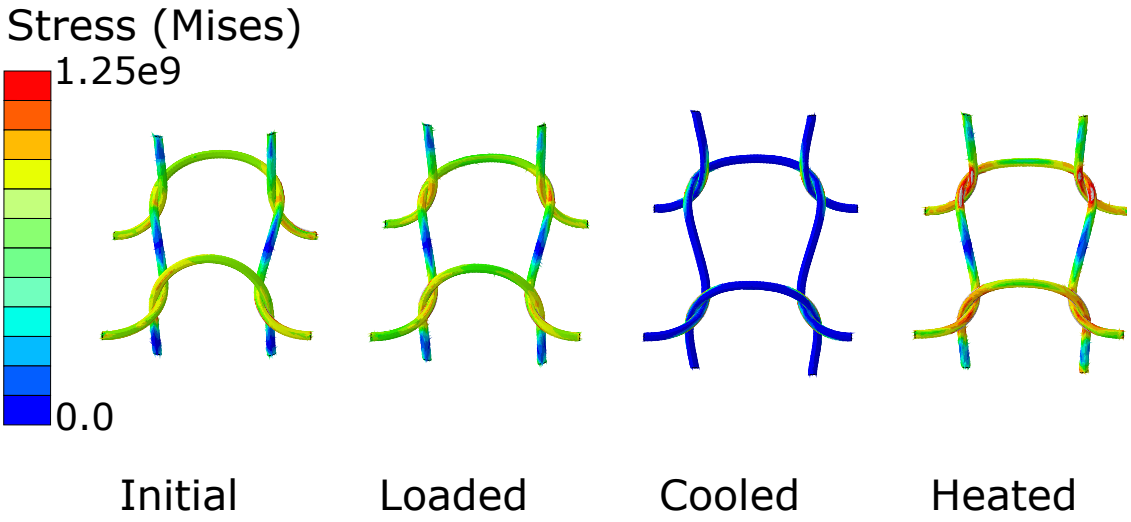

Figure 2.22: Mises stress of the shape set garter RVE under 36 N uniaxial load at key points in iso-force thermal cycle. Wale length is constrained.

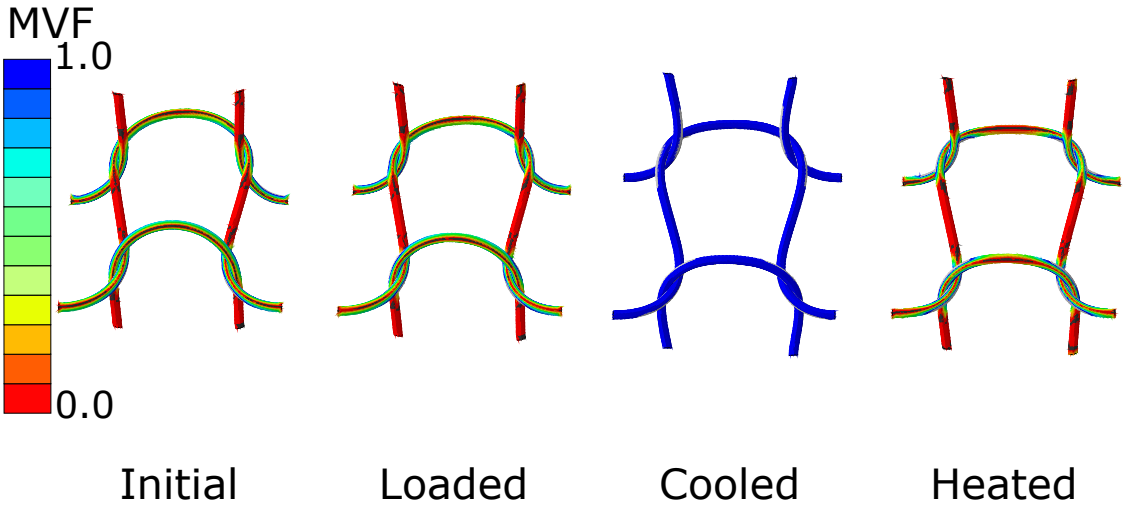

Figure 2.23: Martensitic volume fraction of the shape set garter RVE under 36 N uniaxial load at key points in iso-force thermal cycle. Wale length is constrained.

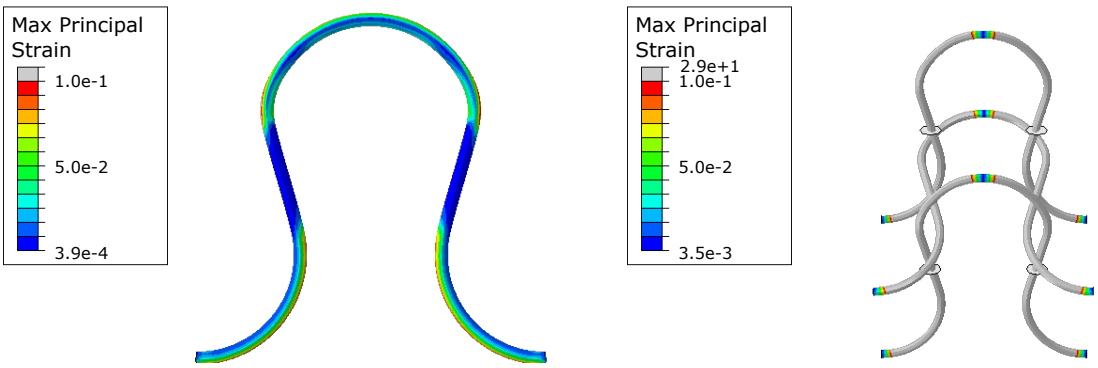

(a) Principal strain at end of forming analysis.

(b) Principal strain at beginning of prestrain analysis.

Figure 2.24: Comparison of max principal strain of a single stitch at the end of the forming analysis against the extended RVE at the beginning of the prestrain analysis, restarted using imported data from the forming analysis. Contour limits are made similar for easy comparison. Maximum principal strain shown to be <29 in the restarted analysis.

3. EXPERIMENTAL PARAMETER DETERMINATION AND VALIDATION OF KNIT ACTUATION TEST CASES

3.1 Preliminary Characterization and Material Parameter Identification

Before a comparison can be made between the FEA model of the knitted structure and the structure's experimental response, the behavior of the material that comprises the structure must be characterized. For SMAs, determining the values of identified parameters that dictate the material's stress-temperature response is paramount. Material properties such as transformation temperatures and their stress dependencies are commonly determined using a combination of two techniques: differential scanning calorimetry (DSC) and isobaric thermal cycling. In this study, two types of samples, representative of the experimental knit sample materials, are examined. The first sample consists of SAES-Getter (spool code 550004) NiTi wire of 0.3 mm diameter with no additional heat treatment (i.e. "off the spool"). The second sample consists of wire from the same spool subjected to a heat treatment of 600^{o}C for 10 minutes followed by a water quench.

3.1.1 Differential Scanning Calorimetry (DSC)

Differential scanning calorimetry is a technique developed in the 1960s to measure the amount of heat required to change the temperature of a sample with respect to a known reference [45]. Due to the exothermic nature of forward transformation and endothermic nature of reverse transformation, this type of testing can easily be used to determine stress-free transformation temperatures; peaks in heat flow will occur at temperatures where phase transformations occur.

The results of DSC tests performed on a heat treated sample and an off-the-spool sample are shown in figure 3.1. The peaks of the non-heat treated sample are clearly less pronounced, particularly in the transformation into martensite. The heat treated sample, on the other hand, has very pronounced peaks that occur at higher temperatures than the non-heat treated sample. In fact, heat treatments have been shown to modify transformation temperatures [46, 47, 48] as well as peak

height [48] considerably in some cases.[1] The resulting stress-free transformation temperatures for

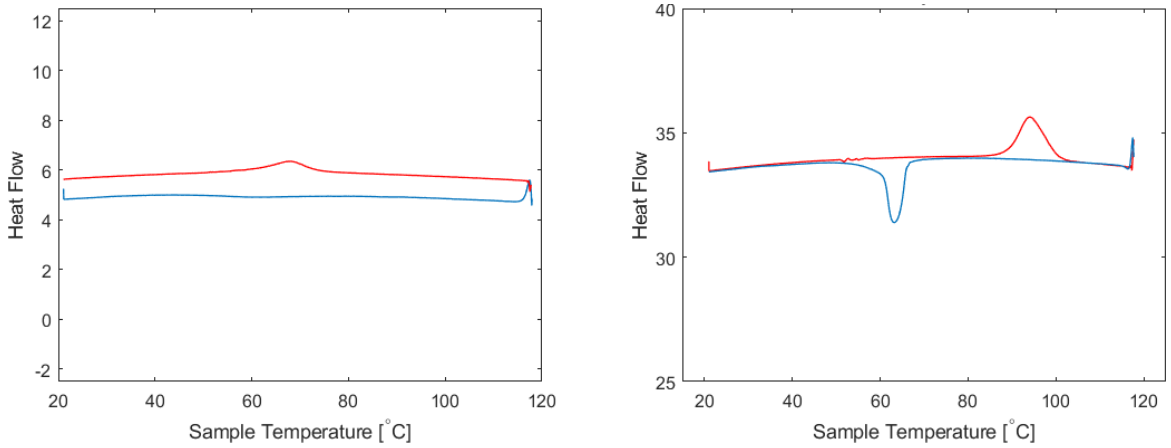

(a) Spool sample (not heat treated).

(b) Sample A (heat treated).

Figure 3.1: DSC results for non-heat treated and heat treated samples.

both samples is listed in table 3.1.

Table 3.1: Stress-free transformation temperatures for both heat treated and non-heat treated samples from DSC data.

°C	M_f	M_s	A_s	A_f
Non-heat treated	52	70	61	78
Heat treated	59	68	91	105

3.1.2 Wire Characterization via Isobaric Thermal Cycling

Determining the parameters used by the Lagoudas SMA model (described in section 2.1) requires characterization of material actuation under a known load case. For this, isobaric thermal cycles were performed on wire samples according to ASTM standards [49]. Wire samples were secured in custom wire grips and mounted in an MTS Insight 30 load frame with a thermal chamber.

[1] Additional discussion can be found in appendix 2.

The chamber was heated to at least 20°C above A_f and the sample was loaded to the testing stress. Temperature was then cycled to at least 20°C below M_f as force was controlled. Displacement was measured using a laser extensometer. For the non-heat treated wire, tests were performed at 200 MPa, 300 MPa, and 350 MPa. The heat treated wire saw a significant increase in unrecoverable strain during cycling under high loading, and therefore tests were performed at lower values of 50 MPa, 100 MPa, and 150 MPa.

3.1.3 Model Parameter Determination

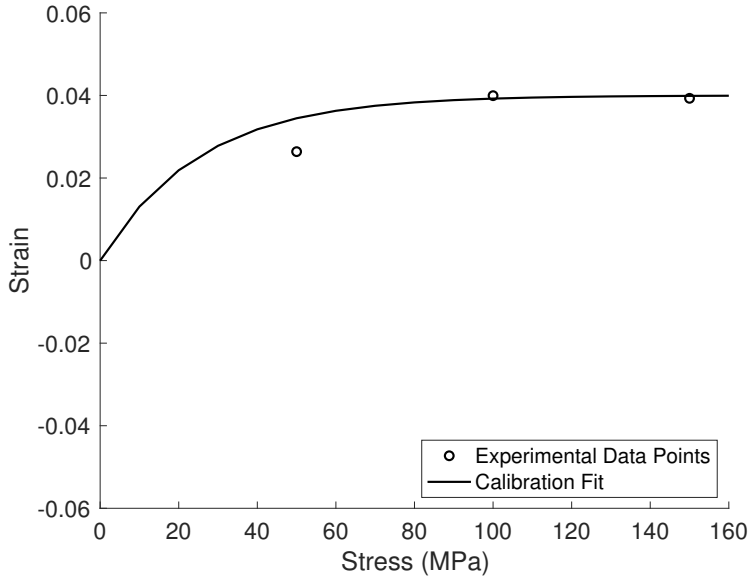

Figure 3.2: H_{cur} curve fit to experimental data from isobaric thermal cycling wire characterization tests.

Model parameters were determined using gradient-based optimization technique packaged in an analysis tool implemented in Matlab previously developed by Leal [50]. The results of the isobaric tests performed on the wires were used to calibrate model parameters such that the strain-temperature curves for the prescribed stress generated by the mathematical tool matched those found experimentally. The parameters determined through this method were Young's modulus of martensite and austenite (E_{M}, E_{M}), transformation temperatures, stress dependence of transforma-

tion surfaces (C_{M}, C_{A}), maximum and minimum transformation strains (H_{max}, H_{min}), parameters to describe the effect of stress on thermally induced transformation (k and σ_o), hardening coefficients ($n1, n2, n3, n4$), and coefficient of thermal expansion (α).

Due to large amounts of unrecoverable strain in the heat treated wire, early knit model runs grossly over-predicted displacement upon transformation. To combat this, the parameters of H_{cur} (namely H_{min}, H_{max}, σ_{crit}, and k) were recalibrated using recovered strain from the isobaric thermal cycles performed on the heat treated wire. The resulting relationship between H_{cur} and stress is shown in figure 3.2. These values were used in the FEA model for the shape set sample. Importantly, the resulting curve better fits the experimental transformation strain recovered at higher stresses, as the knitted structures are mostly subjected to stresses greater than 100 MPa.

Table 3.2: Model parameters for the heat treated wire used in FEA simulations.

E_{M}	96.9 GPa
E_{A}	96.9 GPa
M_{s}	360.4 K
M_{f}	324.3 K
A_{s}	359.1 K
A_{f}	417.8 K
C_{M}	14 MPa/K
C_{A}	12 MPa/K
H_{min}	0.000
H_{max}	0.075
k	1.04e-8
σ_{crit}	0 MPa
α	0
$n1$	0.2388
$n2$	0.1395
$n3$	1.0000
$n4$	0.2831

As the tool used to determine these parameters and the VUMAT are different implementations of the SMA constitutive model, a verification study was performed to compare the results of the Matlab tool against single element ABAQUS studies employing the VUMAT. Figures 3.5 and 3.6

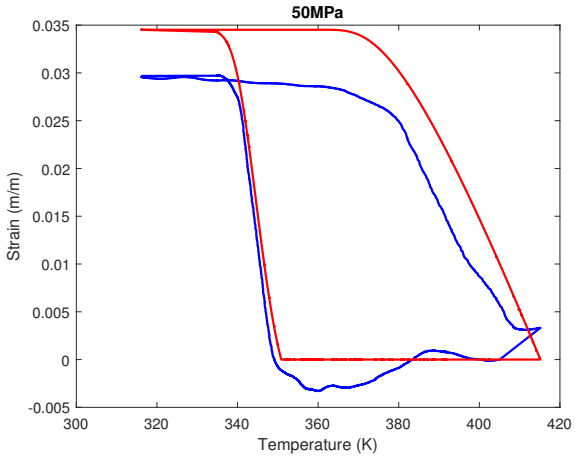

(a) Results from 50 MPa test (blue) overlaid with optimizer results.

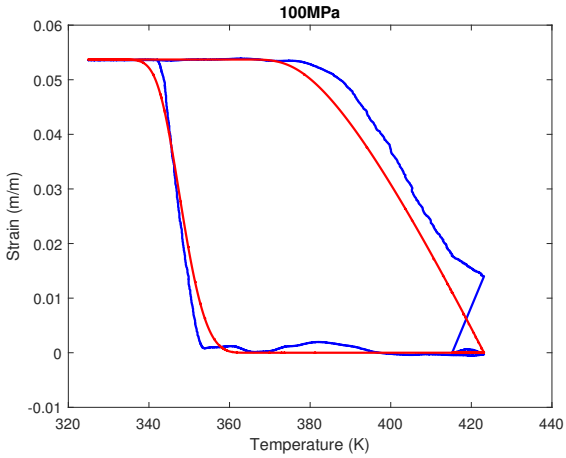

(b) Results from 100 MPa test (blue) overlaid with optimizer results.

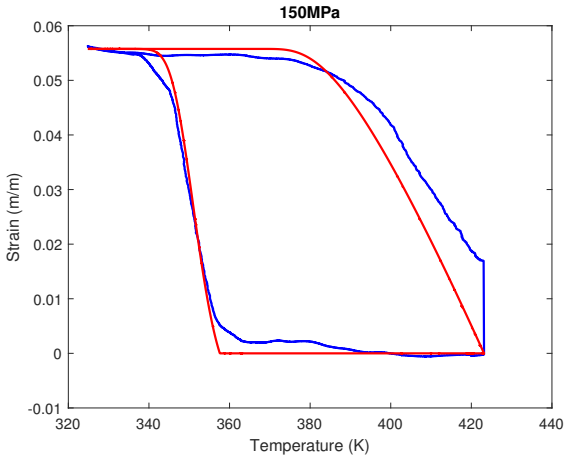

(c) Results from 150 MPa test (blue) overlaid with optimizer results.

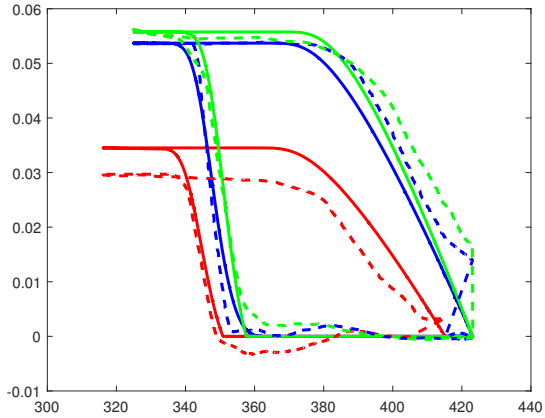

(d) Results from all tests (dashed lines) overlaid with optimizer results.

Figure 3.3: Results of optimized parameters plotted with data curves from isobaric tests performed at different stresses on heat treated wire.

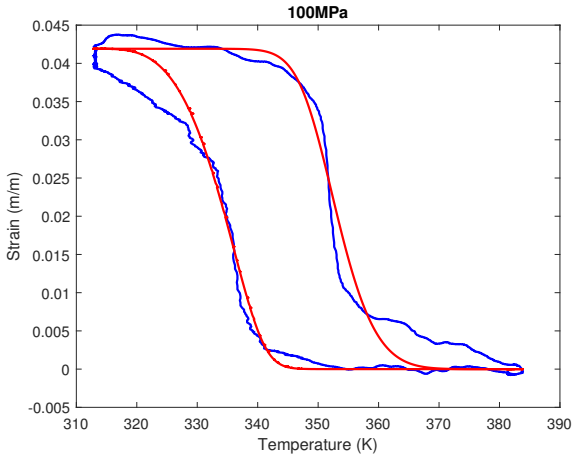

(a) Results from 100 MPa test (blue) overlaid with optimizer results.

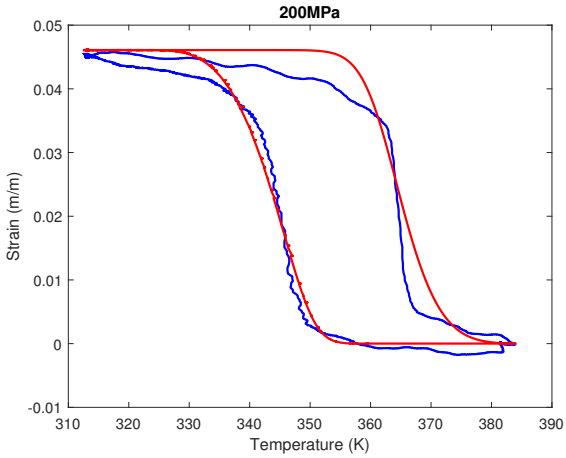

(b) Results from 200 MPa test (blue) overlaid with optimizer results.

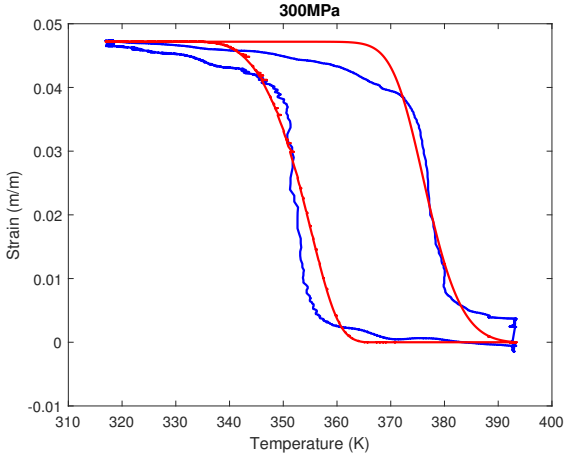

(c) Results from 300 MPa test (blue) overlaid with optimizer results.

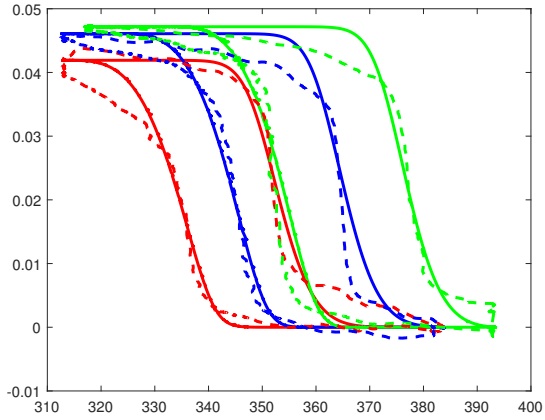

(d) Results from all tests (dashed lines) overlaid with optimizer results.

Figure 3.4: Results of optimized parameters plotted with data curves from isobaric tests performed at different stresses on non-heat treated wire.

Table 3.3: Model parameters for the non-heat treated wire found by optimization tool.

E_{M}	93.9 GPa
E_{A}	109.8 GPa
M_{s}	344.9 K
M_{f}	307.3 K
A_{s}	323.7 K
A_{f}	380.2 K
C_{M}	9.0 MPa/K
C_{A}	8.2 MPa/K
H_{min}	0.000
H_{sat}	0.065
k	5.28e-9
σ_{crit}	0
α	0
$n1$	0.3127
$n2$	0.3368
$n3$	0.3230
$n4$	0.6509

show the results of this verification for the non-shape set and shape set material properties respectively. A reasonable comparison is made between the two models, and the parameters generated via the Matlab tool are therefore acceptable to use in the VUMAT implementation. In the verification of the VUMAT for the shape set model parameters, large temperature increments resulted in a divergence from the expected straight line, particularly at the austenite finish temperature.

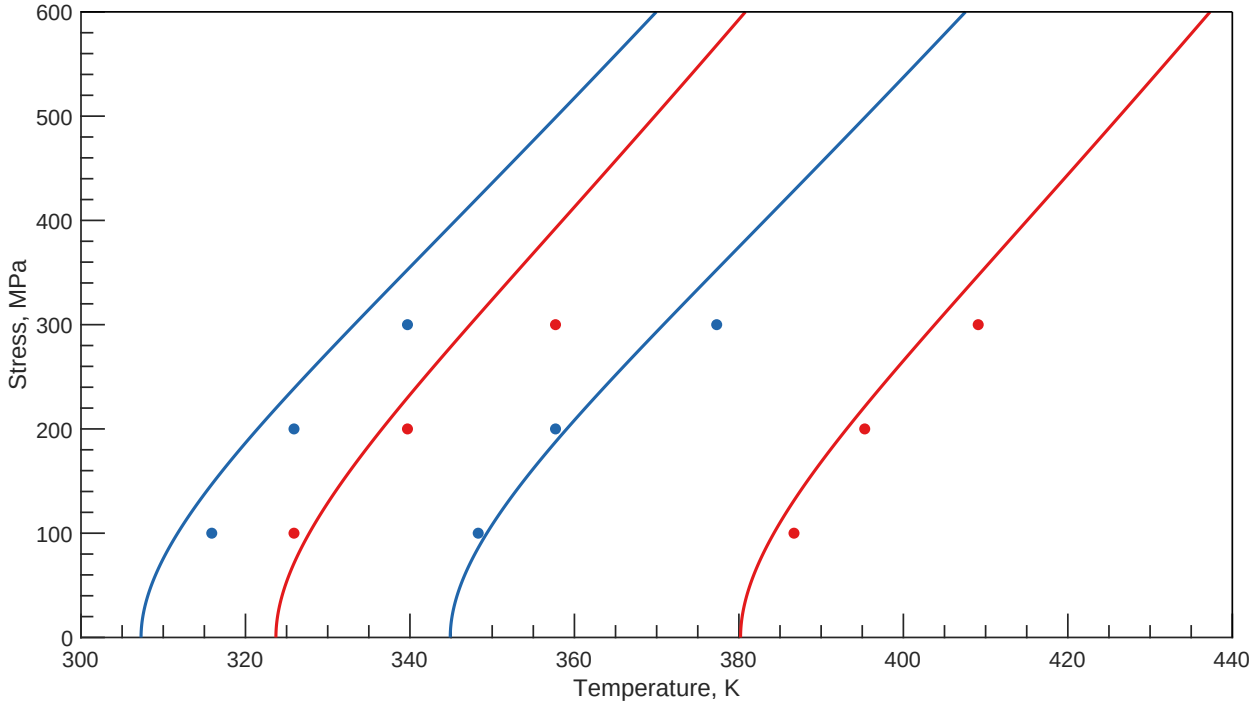

Figure 3.5: Non-shape set phase diagram comparison. Lines generated using Matlab implementation, points generated from ABAQUS/Explicit analyses using VUMAT implementation of SMA constitutive model.

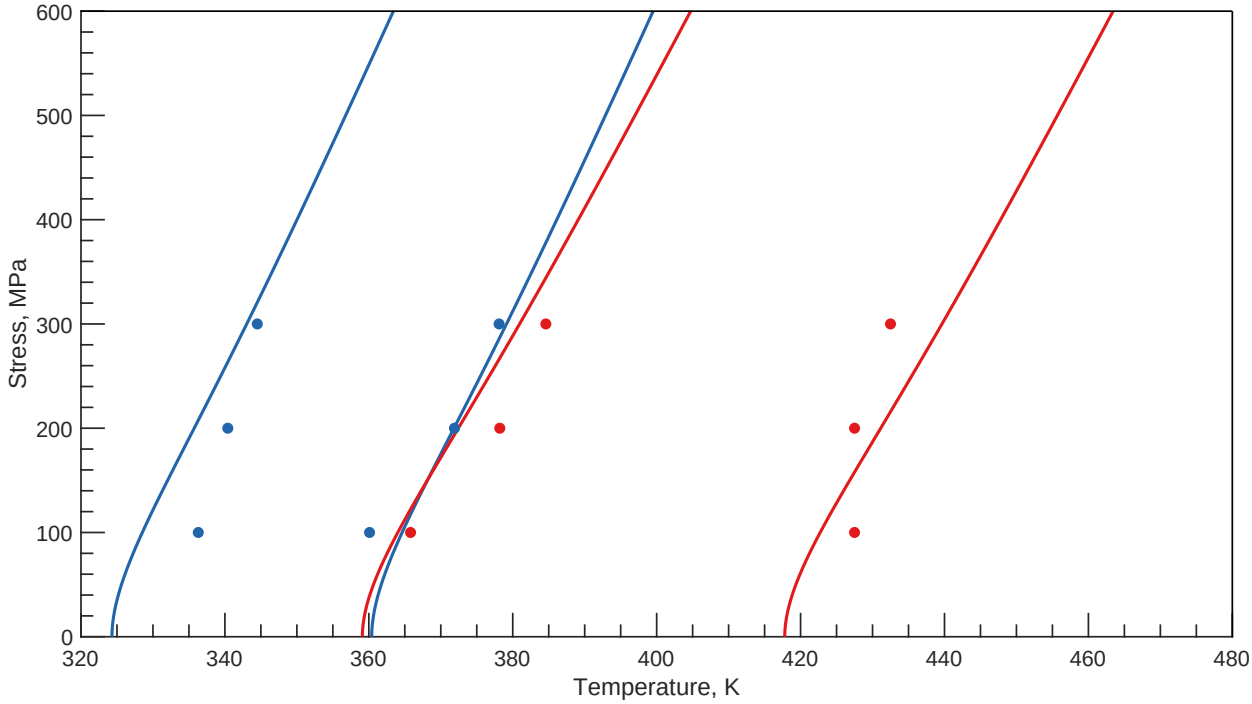

Figure 3.6: Shape set phase diagram comparison. Lines generated using Matlab implementation, points generated from ABAQUS/Explicit analyses using VUMAT implementation of SMA constitutive model.

3.2 Description of Experimental Knit Samples

Two knit samples were knit manually using 5 mm diameter needles and SAES-Getter (spool code 550004) NiTi wire with a diameter of 0.3 mm. Each sample was composed of ten courses (including cast on and cast off) and ten wales. During experiments, only eight courses and eight wales were included in the load path. One sample was knitted of "off the spool" wire; this wire is trained by the manufacturer in uniaxial tension, and this training remains in the material of this knitted sample.

The other sample was shape set in a knitted position to relieve residual stresses incurred from the knitting process [51]. The training imparted by the manufacturer is removed during the heat treatment as well, and no further material training is performed on this sample. To perform the shape setting procedure, the sample was lightly stretched to ensure contact of the needle loops with the sinker loops and secured in a fixture, shown in figure 3.7. Sample and fixture were then placed in an oven at 600^{o}C for ten minutes followed by a water quench.

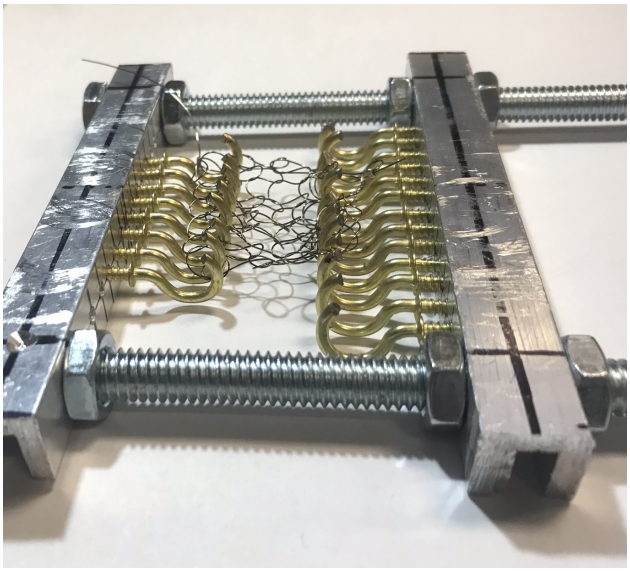

Figure 3.7: Sample in fixture before shape setting.

After the shape setting process, the difference between the two samples was apparent. The shape set sample was elongated and rigid, while the as-knit sample was flexible and springy. The

visual differences are shown in figure 3.8.

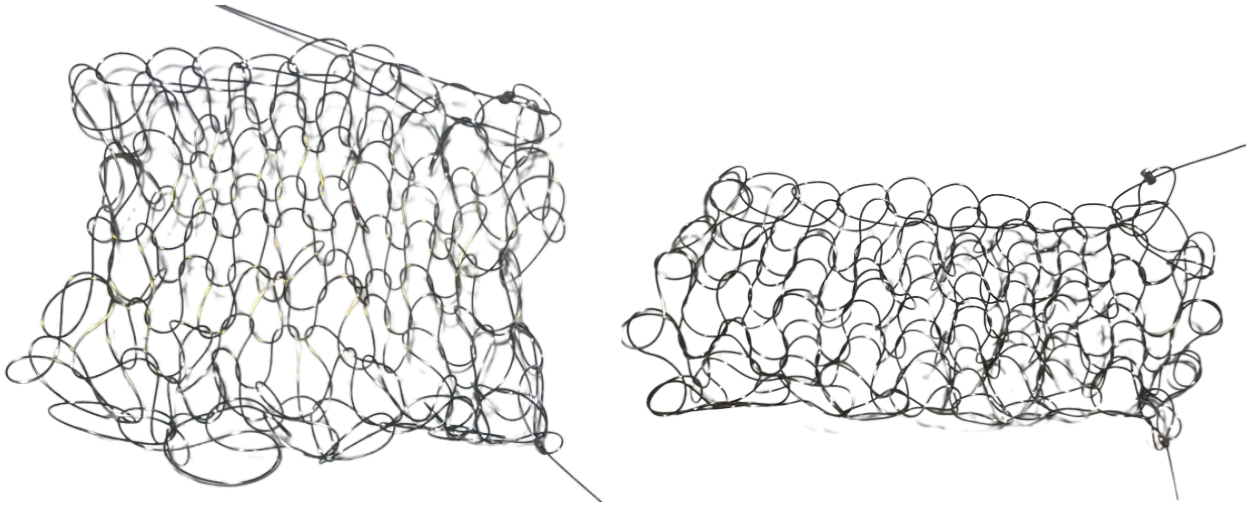

(a) Shape set sample. (b) Non-shape set sample (as knit).

Figure 3.8: Experimental samples before testing.

The knits were mounted into grips by way of high temperature aramid-fiber string. The string was knitted through the upper and lower courses to be loaded in such a way that eight wales were loaded. The loops of the aramid string were looped around aluminum dowels pushed through holes in the sample grips. The samples were thermally isolated from the grips by a layer of phenolic tubing which encircled the aluminum dowels. Reflective tape was adhered to the samples to allow for laser extensometer measurements. The sample grips were then mounted to the MTS grips.

3.3 Iso-Force Tests

An iso-force test is a widely used SMA characterization test to describe actuator behavior under constant load. In single wires, this test is often referred to as isobaric. Applied load is held constant as temperature is cycled, and displacement is measured.

3.3.1 Experiment and Results

Iso-force tests were carried out for three load cases on each sample. The loading conditions were uniaxial in the wale-wise direction, and tests were performed with load controlled to 36 N, 72 N, and 108 N, indicative of 100, 200, and 300 MPa, respectively, of uniaxial stress through

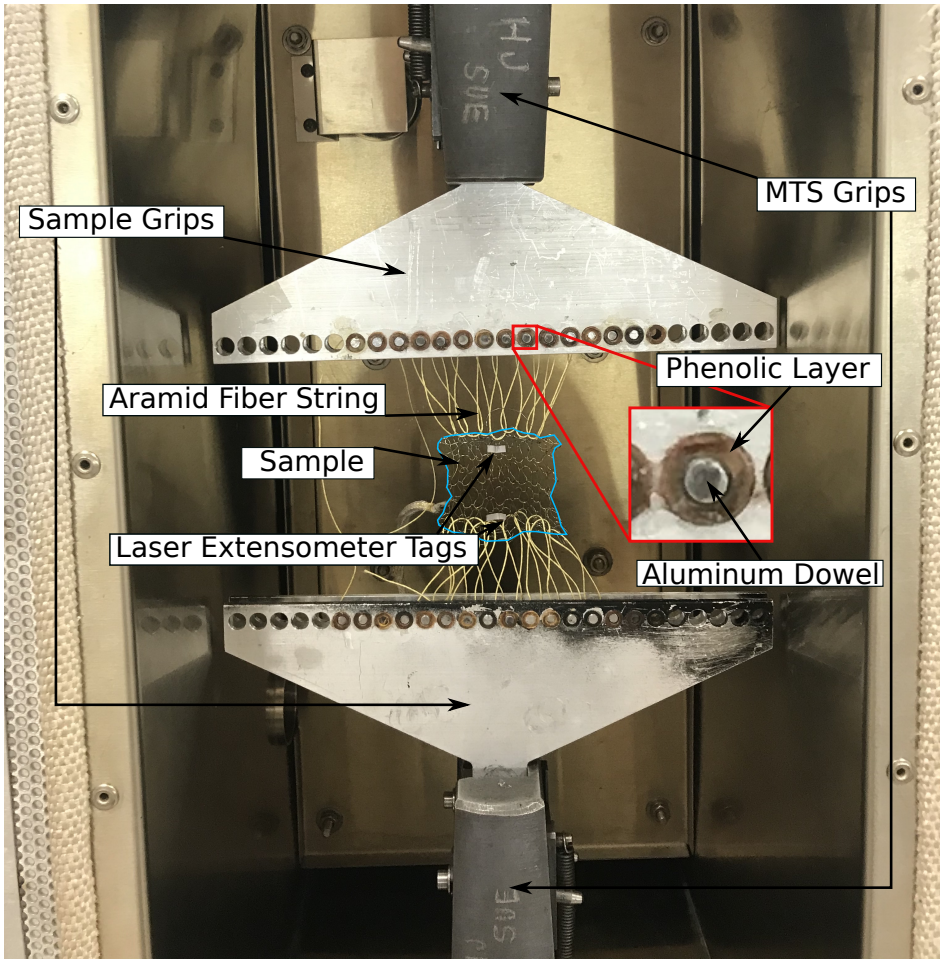

Figure 3.9: Shape set sample (outlined in blue) in grips before testing.

each stitch leg. A thermal chamber encased the sample and grips; laser extensometer data was obtained through a transparent window on the chamber. The room temperature sample was nominally loaded to 4.5 N (an estimated 12.5 MPa in each stitch leg). Load was controlled as the sample was heated to 165°C (438 K). With the sample in an assumed fully austenitic state (fully hot), load was increased to the first testing load. Temperature was then decreased to 50°C (323 K) for the shape set sample and 20°C (293 K) for the non-shape set sample and increased again above 165°C (438 K) as load was controlled and displacement was measured. At this high temperature, load was then increased to the next testing load. This process was repeated until the sample was thermally cycled at all testing loads.

Figure 3.10: Non-shape set sample in grips before testing.

Results

Unloaded in a cold state the shape set sample began the test with a 39.2 mm distance between the two points at which the laser extensometer took measurements. Upon heating and subsequent loading to 36 N, the sample extended to 42.15 mm. The displacements generated and recovered through thermal cycling at each load are shown in table 3.4. The length of the three garter RVEs covered in the range measured by the laser extensometer is plotted against temperature in figure 3.11.

Notably, the shape-set sample both extended and recovered the most at the lowest load. One possible reason for this could be related to the dual mechanisms generating displacement in this

study: the knit structure geometry and the material transformation. As the material transforms, the stitch legs contribute the majority of transformation strain to the extension of the knit structure; in addition, the knit stitch shape changes due to transformation in the loops and allows additional lengthening of the sample. The displacement that can be attributed to the change in geometry is greater than that from the transformation strain generated in the stitch legs. Under lower loads, the knit geometry shift contributes more to displacement generation than at higher loads, where the structure becomes disadvantageously deformed. In addition, retained martensite due to the continuous thermal cycles with no unloading also contributed to the reduction in displacement due to transformation at higher loads.

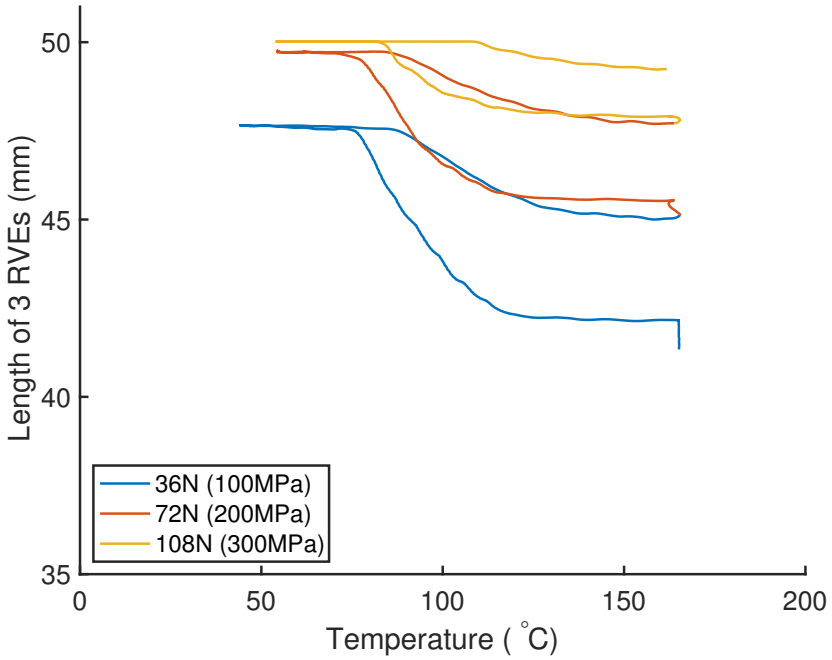

Figure 3.11: Displacement vs. temperature response of the shape set sample under constant load for one continuous test.

None of the tests resulted in full recovery due to the generation of unrecoverable strain in the loops of the stitch. Unrecovered martensite resulting from an increased stress state during structural shift makes up a large portion of this unrecovered displacement, though plastic deformation

Table 3.4: Displacement generated and recovered from thermal cycling the shape set sample at a given load.

Force (N)	Displacement Generated (mm)	Displacement Recovered (mm)	Percent Recovered (%)
36	5.50	2.65	48.2
72	4.73	1.91	40.3
108	2.14	0.79	36.9

may also play a role. Material response cannot perfectly recover displacements generated from structural shifts due to the complex geometry of knits. Upon sufficient cycling, full recovery can be achieved [18], though this occurs at greatly reduced displacements as the primary displacement generation mechanism transitions from geometric deformation to material transformation.

As in the shape set sample, the non-shape set sample did not achieve full recovery for any of the cycles. Unlike the shape set sample, however, percent of displacement generated that was recovered increased as load increased. The non-shape set structure relies considerably more on structural shift to generate displacement than the shape set structure, indicated by the sloped transformation curves in figure 3.12; this sample therefore saw more displacement generation at the lowest load than the shape set sample. Displacement generation decreased as load increased in a manner comparable to the shape set sample, as shown by figure 3.13, which displays the displacement generated and recovered during each thermal cycle performed on both the shape set and non-shape set samples. As load increases, each thermal cycle tends to both generate and recover less displacement than the thermal cycle performed under the next lowest load. This can be attributed to the accumulated martensite resulting from the lack of unloading between thermal cycles. Full recovery was not achieved due to increased stress in the loops of the stitches, and without unloading to allow full recovery into austenite the martensite in the loops remained in the structure during the following cycles. Displacement due to transformation of the following cycles was therefore smaller as less austenite was available to transform upon cooling. Non-shape set samples may have recovered a higher percentage of displacement generated due to the higher temperature

utilized in thermal cycles for this experiment.

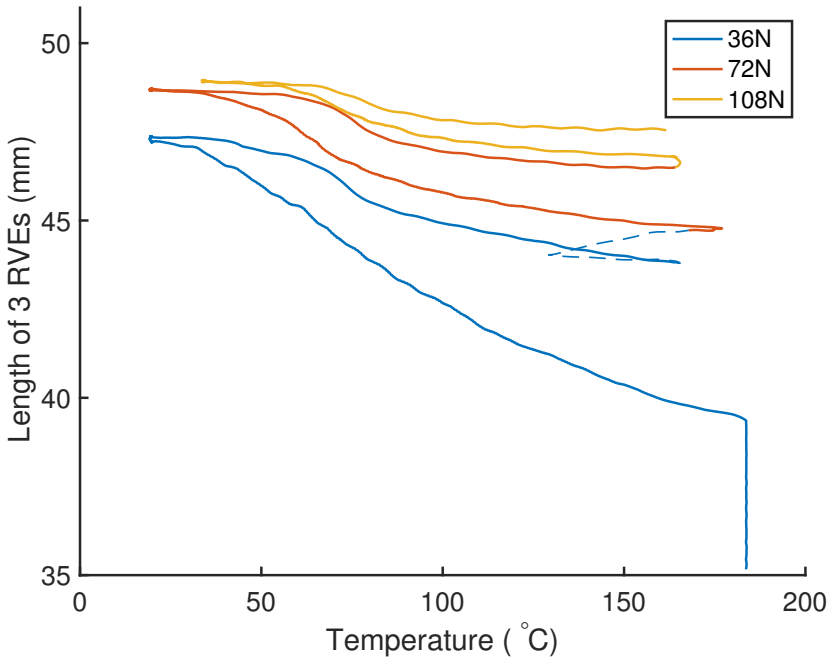

Figure 3.12: Displacement vs. temperature response of the non-shape set sample under constant load for one continuous test.

The experimental results were also compared against existing literature. Iso-force thermal cycles were performed under low loads [16] on a non-shape set sample with 15 courses and 15 wales knitted in a garter pattern from 0.381 mm wire. Recovery strain $\zeta = \frac{l_m - l_a}{l_m}$ for these cycles was obtained, where l_m is the length of the cooled sample and l_a is the length of the sample after recovery. These results were compared against the recovery strains obtained from the iso-force experiments performed in this work under significantly higher loads. Force applied was normalized by number of wales for a closer comparison. Figure 3.14 shows the comparison between this work and reported literature for recovery strain against applied force. The trends in each indicate a reduction in recovery strain under higher loads. It is important to note that experiments performed in this work and in the referenced work were initiated from the lowest load and not unloaded between cycles.

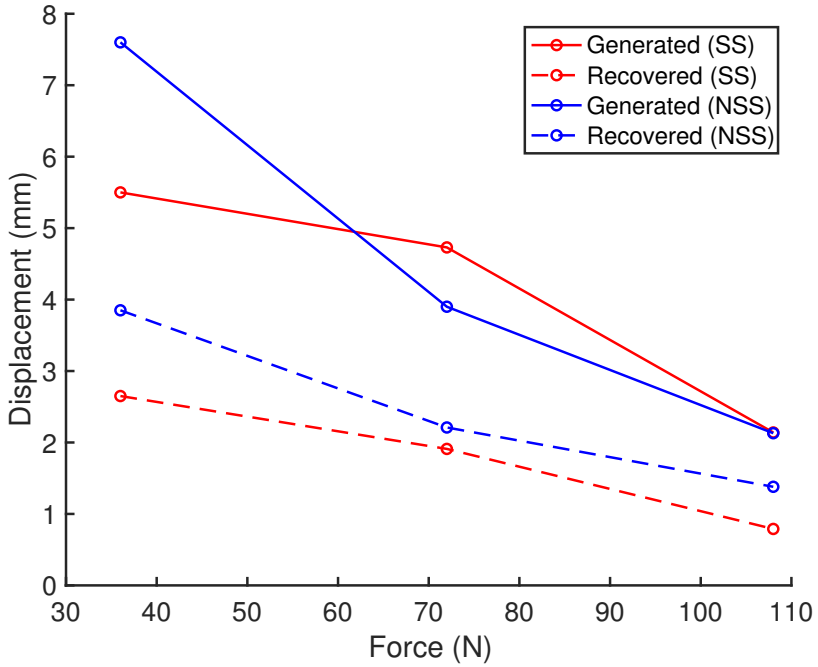

Figure 3.13: Displacement generated and recovered from thermal cycling both the shape set (SS) and non-shape set (NSS) samples at a given load.

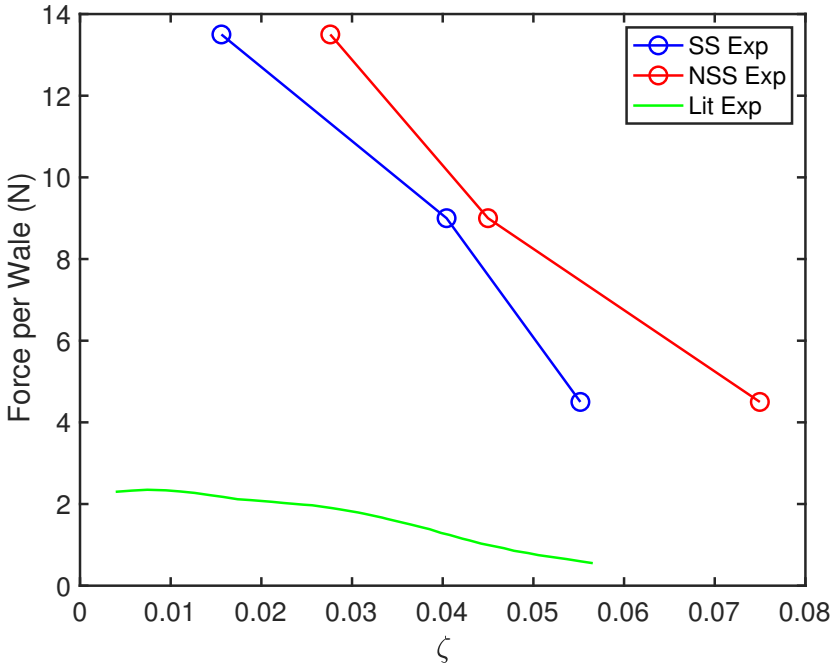

Figure 3.14: Force per wale against recovery strain comparison. Results from shape set (SS Exp) and non-shape set experiments (NSS Exp) are compared against results reported in literature [16].

Table 3.5: Displacement generated and recovered from thermal cycling the non-shape set sample at a given load.

Force (N)	Displacement Generated (mm)	Displacement Recovered (mm)	Percent Recovered (%)
36	7.60	3.85	50.7
72	3.90	2.21	56.7
108	2.13	1.38	64.8

3.3.2 Comparison of Model and Experimental Results

The results of the iso-force experiments indicated that true uniaxial loading was not achieved. When compared with the results of the uniaxial model, the experiment underperformed in both loading-based and transformation-induced extension. The failure to achieve a truly uniaxial loading scheme during the experiment is likely a result of the boundary conditions through which each sample was attached to the grips. The aramid fiber string used to knit each sample to the metal dowels of the grips was intended to provide equal loading to each wale, as the knitting technique allowed for sliding of the string, thereby equalizing load along the course. The dowels, however, were static and not spaced according to wale length, causing a misalignment between the dowels and the wales. Even in a minimally loaded configuration, a small force in the course-wise direction was applied to the sample via the attachments at the outermost wales. As load increased and the sample structurally displaced, the wale length decreased further, exacerbating the angle at which the aramid string connected with the sample and in turn increased the course-wise loading. Truly uniaxial experiments would require a load equalizing attachment method that allows for sample contraction via wale length shortening.

Figure 3.15 shows the normalized displacement resulting from transformation of the shape set sample as it compares to the shape set model runs for the unconstrained case and constrained case. The unconstrained case represents a truly uniaxial case and allows the largest amount of possible structural extension for the given geometry; wale length is not constrained, and thus sinker loops are able to slide, enabling the maximum amount of both wale length shortening and course

extension from structural contributions. The constrained model utilizes a fixed wale length; no sliding of sinker loops is allowed, and very little structural displacement is provided in extension. The experimental sample, however, allowed sinker loops to slide, though a gradually increasing force may have opposed this. As the sample wale length decreased, the angle swept between the sample edge and the aramid fiber attachment increased, leading to an increased course-wise force which opposed wale length shortening. The geometric deformation leading to extension of the experimental sample is therefore considerably improved over the constrained model while not achieving that of the unconstrained model. The experiment falls between the constrained and unconstrained models, as expected.

Figure 3.16 shows the normalized displacement of the iso-force thermal cycles carried out at 72 N for the shape set experimental sample and the constrained and unconstrained models. The experiment is shown to achieve a similar magnitude of extension upon transformation as the constrained model. This is likely due to retained martensite in the experiment, and is discussed further in section 3.3.3.

Figure 3.17 shows the normalized extension of the shape set experimental sample compared with that of the constrained and unconstrained models for an iso-force thermal cycle performed at a load of 108 N. Here, the experiment is clearly shown to achieve less extension upon transformation than the constrained model.

Figure 3.18 shows the normalized displacement due to thermal cycling of the non-shape set structure, effectively showing percent length of an RVE during a thermal cycle. The experiment extends more than both the unconstrained and constrained models at a fully cooled state, rather than extending to a value between the unconstrained and constrained extension at a cooled state as expected. Recall from section 2.7.2 that the non-shape set sample undergoes stress-induced transformation due to initial loading prior to thermal cycling. Starting temperature of the analysis greatly affects stress-induced transformation; a higher temperature during stress-induced transformation will lead to the generation of less martensite under the same loading than a cooler temperature. The model analyses were performed starting at 147^{o}C, while the experiment was loaded

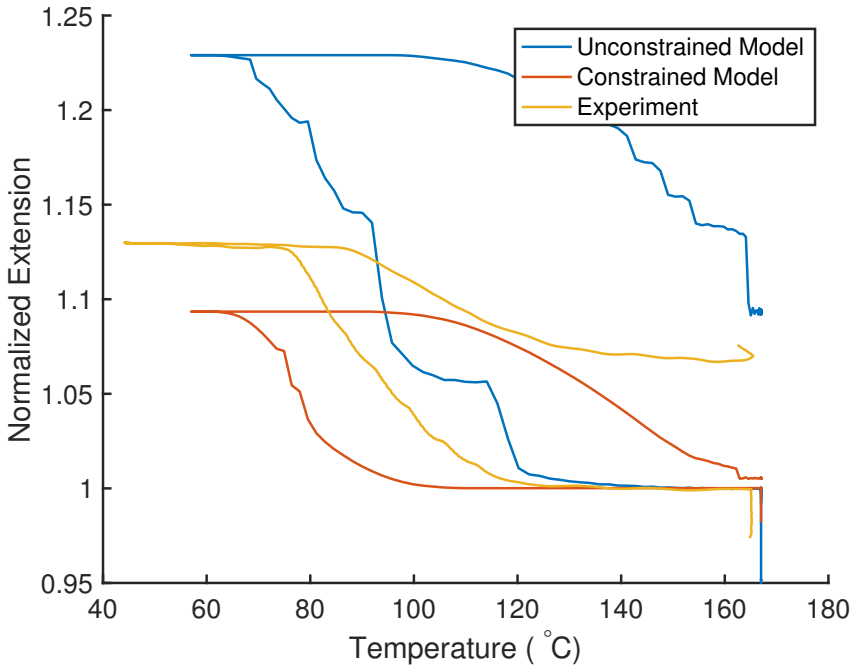

Figure 3.15: Normalized extension and recovery due to thermal cycling achieved under 36 N load (100 MPa in stitch legs) by experiment compared against model predictions for the shape set sample.

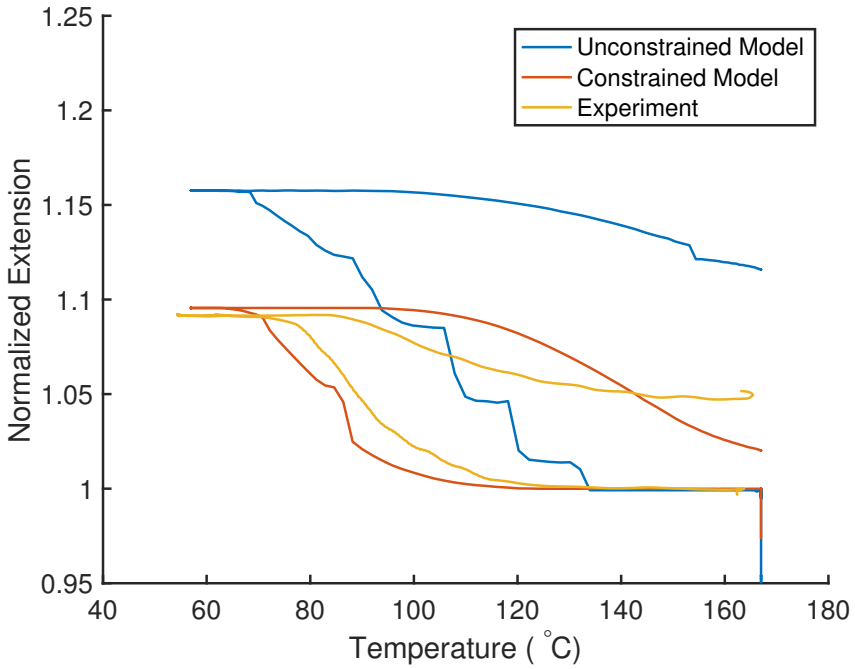

Figure 3.16: Normalized extension and recovery due to thermal cycling achieved under 72 N load (200 MPa in stitch legs) by experiment compared against model predictions for the shape set sample.

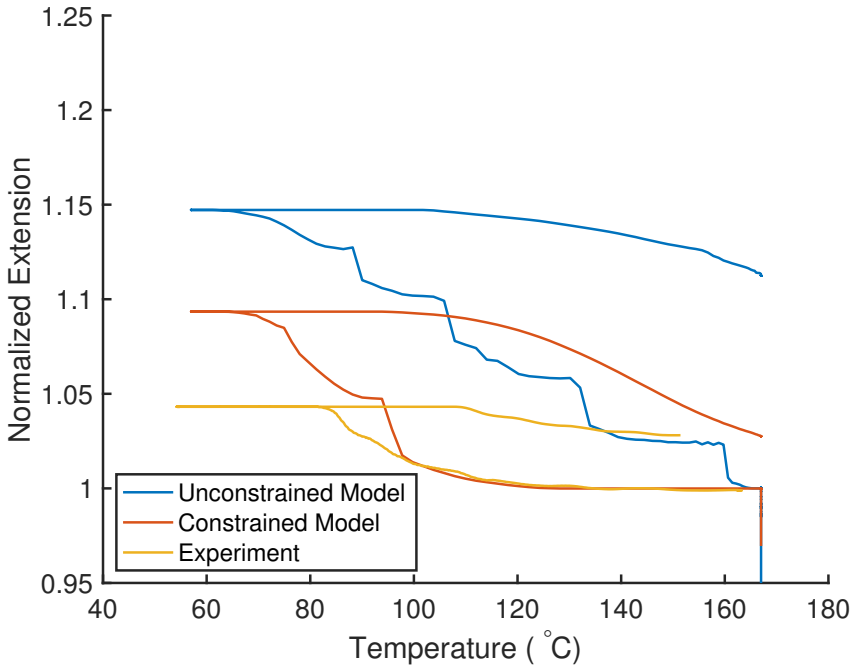

Figure 3.17: Normalized extension and recovery due to thermal cycling achieved under 108 N load (300 MPa in stitch legs) by experiment compared against model predictions for the shape set sample.

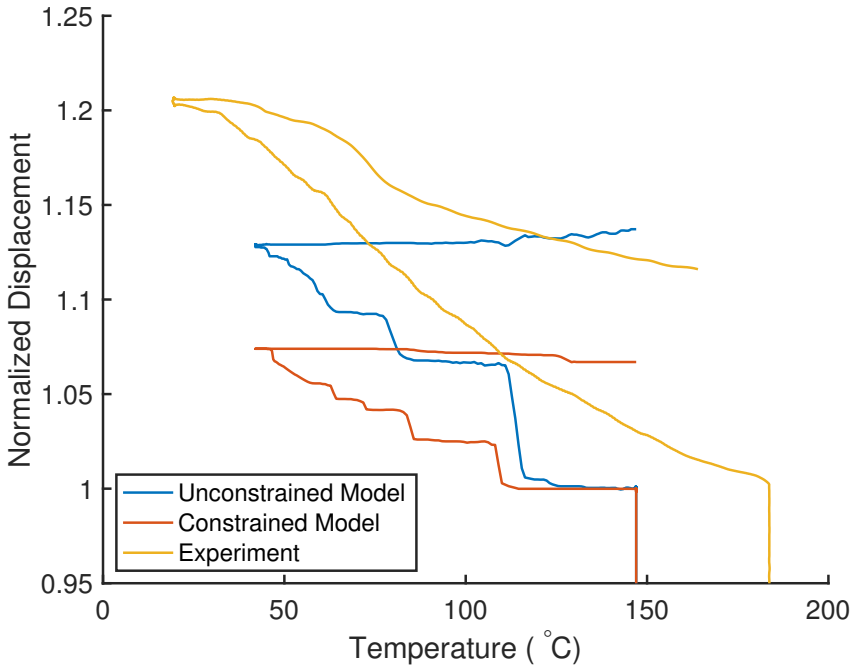

Figure 3.18: Normalized extension and recovery due to thermal cycling achieved under 36 N load (100 MPa in stitch legs) by experiment compared against model predictions for the non-shape set sample.

at 184°C; less martensite was likely generated by the experimental sample during initial loading than what the model predicted due to this temperature disparity. Therefore, upon cooling, additional martensitic transformation was allowed in the experiment than in the models, leading to a greater normalized displacement from the experiment than both models. Moreover, the experiment was cooled to a lower temperature than both models; some regions of the models did not reflect a martensitic volume fraction value of 1.0, indicating that additional cooling would generate at least some additional martensite.

Figure 3.19 shows a comparison of normalized displacement of iso-force thermal cycles performed on the non-shape set experimental sample and the models performed under a constant load of 72 N. As in the 36 N non-shape set iso-force comparison, the normalized displacement of the experimental sample is again greater than that achieved by the unconstrained model. This differs from the performance of the shape set sample under 72 N, where the shape set experiment underperformed against the constrained model due to retained martensite in the material. This indicates that the effect of stress-induced transformation during loading is more significant at this temperature difference than the residual martensite retained in the experimental sample due to a lack of unloading the sample. Like the 36 N non-shape set models, the models for the 72 N iso-force runs would achieve additional transformation with additional cooling.

Figure 3.20 shows the normalized displacement results of the 108 N iso-force experimental results compared against the unconstrained and constrained model runs for the non-shape set knit. A significant reduction in transformation displacement is obvious compared against cycles under lower loads, as the high load induces a large geometric deformation prior to thermal cycling. Notably, the constrained model outperforms the unconstrained model at this load. This is likely because material transformation in the stitch legs becomes the dominating mechanism of displacement generation at this load, and due to geometric deformation larger regions of the unconstrained model are transformed during initial loading than the constrained. This means that the constrained model can generate more displacement upon cooling, as larger regions are able to transform into martensite than in the unconstrained model. The experiment appears to follow the constrained

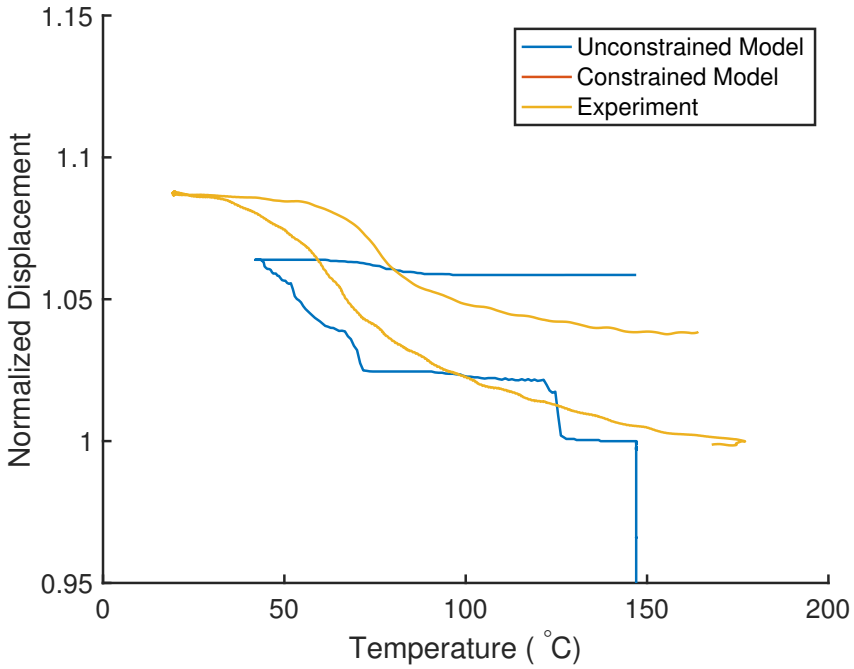

Figure 3.19: Normalized extension and recovery due to thermal cycling achieved under 72 N load (200 MPa in stitch legs) by experiment compared against model predictions of the non-shape set sample.

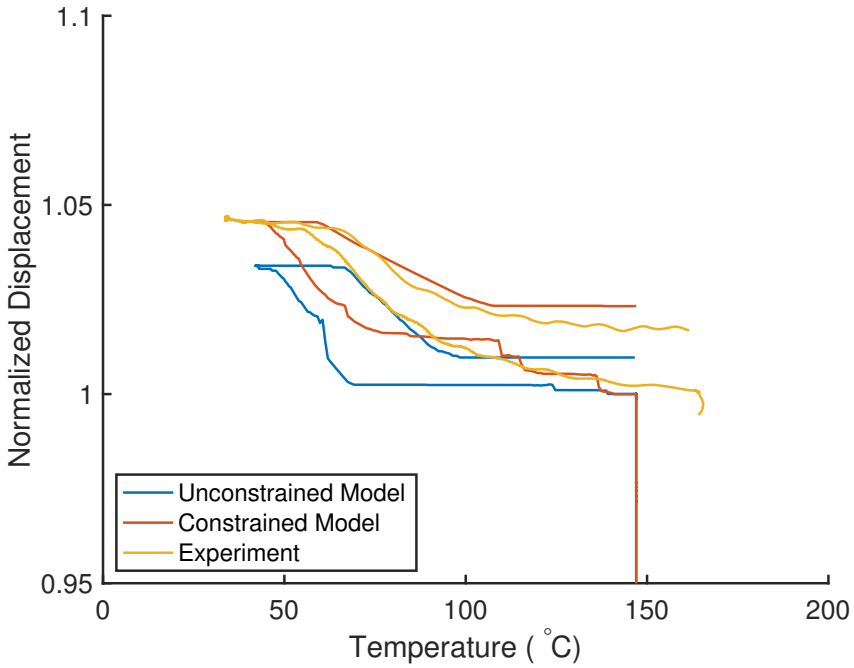

Figure 3.20: Normalized extension and recovery due to thermal cycling achieved under 108 N load (300 MPa in stitch legs) by experiment compared against model predictions of the non-shape set sample.

model. In this case, the retained martensite from the previous experiments likely offset the disparity generated from the temperature difference.

3.3.3 Discussion

The results of the 36 N iso-force thermal cycles performed with the shape set considerations were as expected: normalized extension of the experimental sample fell between the unconstrained and constrained model results. This indicates that a true uniaxial load case was not achieved in the experimental setup. However, the experimental results for the shape set 72 N and 108 N iso-force thermal cycles did not behave in this manner. In fact, for the 72 N case the normalized displacement was slightly lower than that of the constrained model.

It is important to note that during the experiment, the cycles were performed in an increasing order (i.e. 36 N was performed first, then 72 N, finally 108 N), and the sample was not unloaded between cycles. The only test that began from a zero-load state was the 36 N test. At the end of the 36 N cycle, full recovery is not achieved, indicating that unrecovered martensite remains in the material. This can be seen in both the constrained and unconstrained models as well, as the stress increase in the bends raises the temperature required for reverse transformation into austenite. The model, however, begins each iso-force thermal cycle simulation from an unloaded state; in this case, the RVE is fully austenitic at the beginning of each loading cycle.

When the experimental sample is not unloaded at the end of the 36 N thermal cycle, the unrecovered martensite remains in the material. Thus, this martensite cannot be generated upon forward transformation; therefore, the magnitude of transformation is reduced. This manifests in figure 3.16, where the extension upon transformation is now similar to that of the constrained model, rather than between the constrained and unconstrained as expected.

This phenomenon is further exacerbated in the 108 N cycle with the shape set sample, where additional unrecovered martensite from the 72 N cycle remains in the system. The magnitude of displacement generated upon cooling is significantly less than expected. It is therefore recommended that future experiments begin all trials from an unloaded state.

With regards to fitting of model parameters of the shape set sample, good matching in curve

shape between both constrained and unconstrained models and the experimental runs is generally obtained during forward transformation. On reverse transformation, however, the model results tend to have longer, flatter curves with higher transformation temperatures than the experiment. This is likely due to poor calibration of model parameters affecting reverse transformation. Additional calibrations based on isobaric thermal cycles with a single wire would likely improve model performance on recovery with respect to experimental results, though calibrating to knit experimental data may also offer improvement.

Non-shape set samples produced narrow displacement generation and recovery curves and in the three load cases tested saw greater extensions than predicted by the model. This is due to a number of factors. Model simulations did not closely match the temperature ranges imposed on the experiment. Not only did this lead to incomplete forward transformation of the model upon cooling, but the cooler temperature upon loading allowed for a greater accumulation of stress-induced martensite than what the experimental sample likely experienced. This reduced the displacement generated by the models during transformation. Unlike the shape set counterpart, the non-shape set experimental thermal cycle performed at 72 N outperformed the displacement generation predicted by the model. At 108 N, however, the retained martensite in the experiment offset the disparity created by the difference in temperature of the model, and the experimental results appeared to follow the results of the constrained model. Importantly, the constrained model also generated more displacement than the unconstrained model during transformation for this initial state and load case only. This is because the unconstrained model is at a state of deformation upon loading which allows no further inter-loop sliding, and transformation in the stitch legs is the only available method of displacement generation. The constrained model, however, has a region of the stitch loop that is able to transform during cooling, allowing some amount of inter-stitch sliding. This, in addition to the transformation of the stitch legs, allows the constrained model to produce a higher displacement than the unconstrained model for this case. The martensitic volume fractions of the unconstrained and constrained models at this initial loading are shown in figure 3.21.

In addition, non-shape set models at higher temperatures experienced a counterintuitive shift in

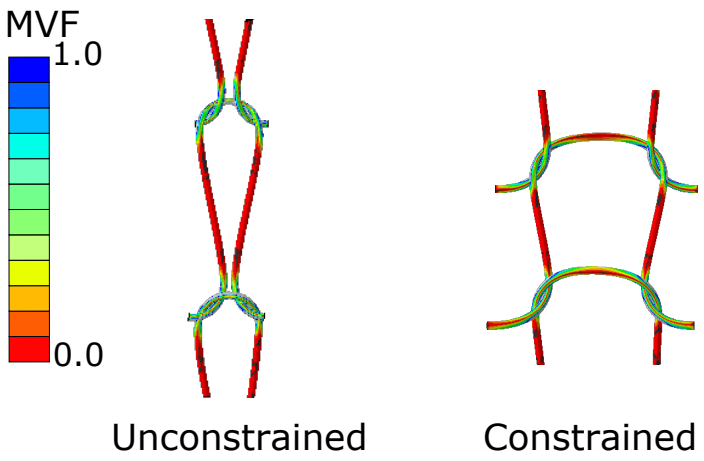

Figure 3.21: Martensitic volume fraction at initial loaded state for 108 N (300 MPa) for both constrained and unconstrained models.

transformation temperatures; as load increased, the temperature at which displacement generation occurred decreased. This is likely explained in part by a lack of geometric deformation that occurs during transformation at high load levels, particularly at 108 N of constant load. As previously discussed, geometric deformation is responsible for a majority of displacement generation and is enabled by transformation in the stitch loops. Under this load state, the loops and portions of the stitch legs are in stress-induced martensite, and almost no additional bending of stitch loops is induced due to cooling. The only mechanism able to generate displacement is martensitic transformation of lower stress regions of the legs, which due to stitch geometry are at or lower than the 300 MPa anticipated from the 108 N applied load. Not only is the relative magnitude of this displacement generation very small, but the stresses of these regions are sufficiently low to drive transformation temperatures to a much cooler temperature than expected.

3.4 Block Force Tests

A block force test is an SMA characterization test designed to explore the maximum amount of force a sample is capable of producing through thermal cycling under a fixed displacement. Special considerations were taken in both the modeling and performing of this test, as best practice for modeling and experimenting with SMA suggests loading the material from an austenite parent phase. Block force tests are less common in modern literature as they are less indicative of SMA

actuator behavior than iso-force tests in particular. However, since smart fabrics may be subject to vastly different boundary conditions than typical actuators, blocking force characterization is pertinent to this study.

3.4.1 Experiment and Results

This experiment was performed on both the shape set and non-shape set sample after each had undergone the full course of iso-force testing. A thermal chamber encased the sample and grips; laser extensometer data was obtained through a transparent window on the chamber. The unloaded sample was heated to a fully austenitic state above 165°C (438 K) and loaded to 36 N, providing an estimated 100 MPa of uniaxial stress through the legs of each stitch. The sample was then cooled under force-controlled conditions to 55°C (328 K) for the shape set sample and 20°C (293 K) for the non-shape set sample. Force control was then deactivated and grip displacement was held constant. Temperature was then increased to 165°C (438 K) while the force generated through the contraction of the sample was measured.

Results

Figure 3.22 shows the results of the shape set experimental block force test. The test was initiated at high temperature (165°C) and cooled under load control at 36 N to 55°C. In the shape set sample, this low temperature was sufficient to ensure full transformation into martensite. At the cold temperature, crosshead motion was controlled to be zero and load measurements were taken. Despite a constant temperature reading, load increased to 55.6 N. This is likely due to thermal expansion of the grips, which, due to a large thermal mass, did not equilibrate to the low temperature before load control was deactivated. Temperature was then increased, and transformation initiated around 80°C. Load increased as the sample transformed, achieving a maximum of 174.9 N at 109°C. At this point, the test was terminated to prevent the load cell from overloading. A discontinuity in the slope of the load-temperature curve occurs just before termination; this is a result of the test stopping and restarting at this point. It is nearly impossible to isolate the force contributions of the knit from those of the expanding fixtures, and therefore this test is likely an

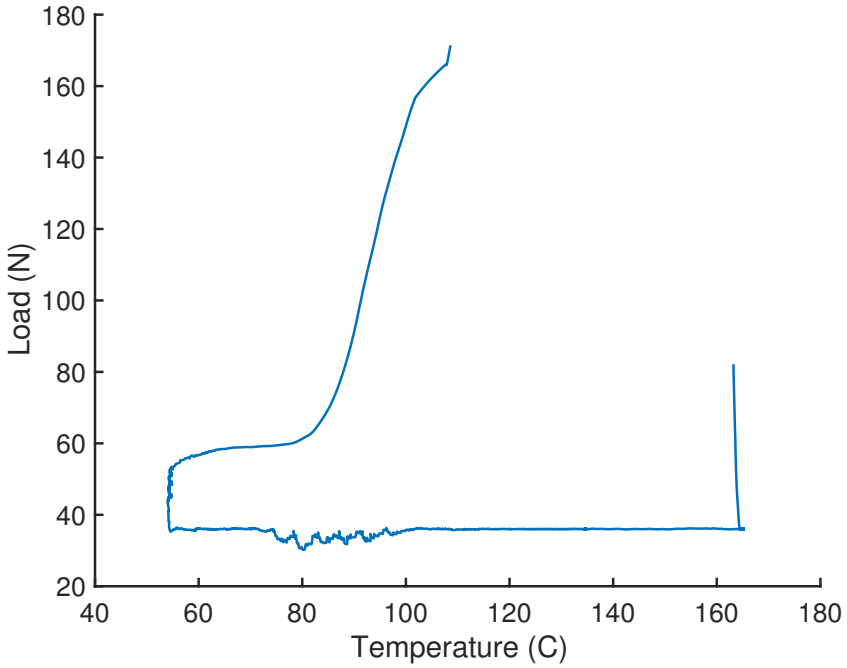

Figure 3.22: Blocking force generated by shape set sample under constant displacement.

overestimation of performance.

Figure 3.23 shows the results of the non-shape set experimental block force test. Similar features from the shape set experiment are present here, particularly at the cold state, where thermally expanding fixtures increased the load with no measured change in sample temperature. Maximum load was achieved at 117°C and is shown to be 132.3 N. However, continued heating results in a decrease in load, which is not typical for a block force test. Load at test finish was 114.9 N. This may be a result of either thermal expansion of the fixtures or deformation of the sample, as after transformation the only available mechanisms for relaxation are plastic deformation and fixture expansion. However, plastic deformation of the sample is most likely to occur in the loop segments and would not likely cause a relaxation of this magnitude.

3.4.2 Comparison of Model and Experimental Results

The challenges faced in performing the block force tests experiments, particularly thermal expansion of the fixtures, render comparison against model data difficult due to the complicated interdependencies of stress and temperature on SMA transformation. Figure 3.24 shows the shape

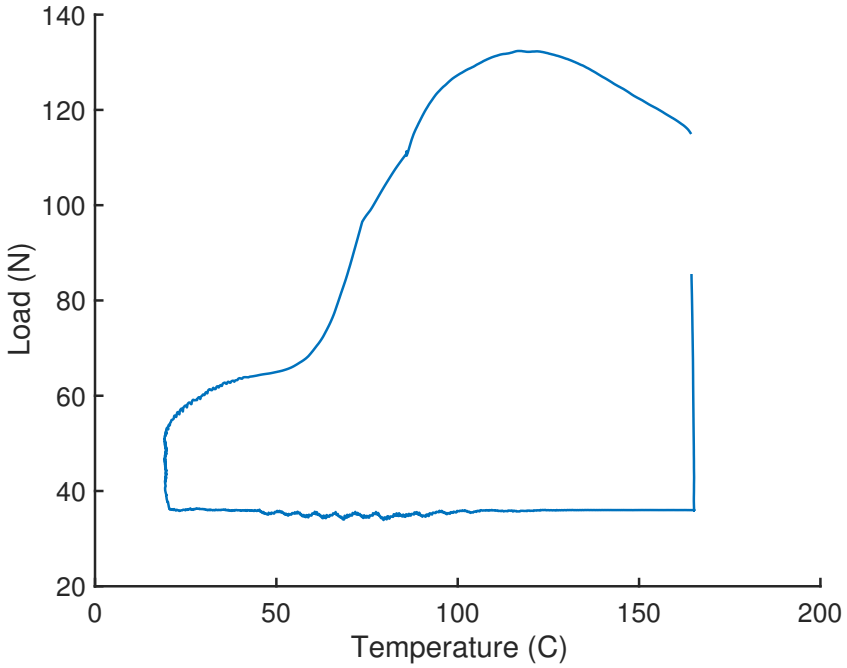

Figure 3.23: Blocking force generated by non-shape set sample under constant displacement.

set experimental block force data plotted against the model data for the same size sample for unconstrained and constrained cases. The experiment appears to exhibit the highest force output for the given temperature at every point and does not fall between the unconstrained and constrained model results. In addition, the experiment begins transformation much sooner compared to the models. Due to thermal expansion of the fixtures, the experimental sample is at a higher stress state (by way of experiencing higher load) than the model before heating; however, increased stress tends to increase transformation temperatures, so this shift is more likely due to a bad calibration of parameters affecting reverse transformation. Overall, the general trend of the experimental data indicates that the model predicts force generation of comparable orders of magnitude. With improved calibration and better controlled experiments, force generation under constrained displacement may be more reasonably predicted with this model.

Figure 3.25 shows the results of the experimental block force test compared against the model predictions for the non-shape set sample. As in the shape set case, the experiment appears to output more force for every temperature than either model prediction. Transformation of the constrained

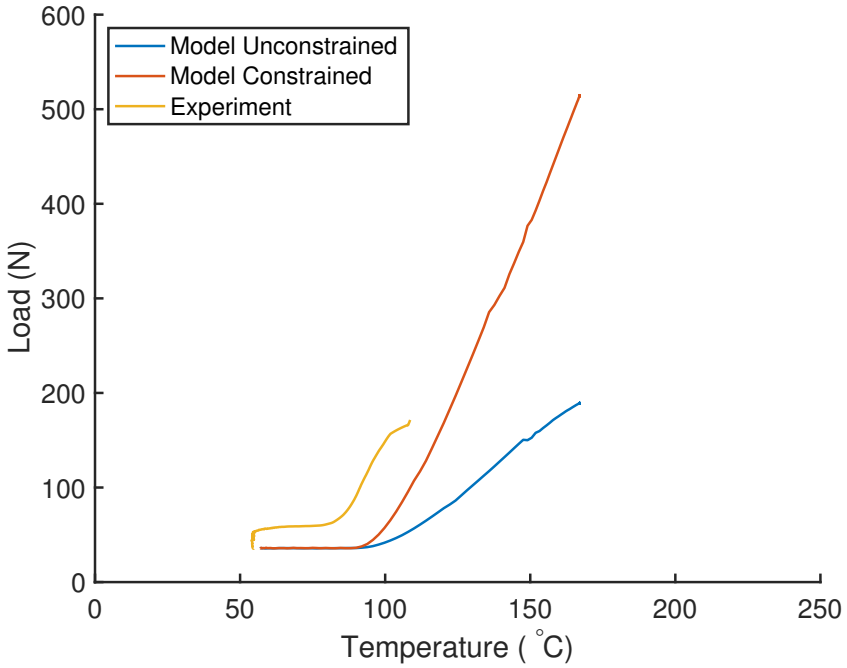

Figure 3.24: Comparison of blocking force generated by shape set sample under constant displacement.

model appears to begin around the temperature at which the analysis started. Note that additional cooling to ensure complete martensitic transformation should have been employed prior to the block force analysis. Transformation of the experiment appears to begin around 50°C, but due to the higher stress state the experiment is in at the higher load state, reverse transformation is expected to begin at a cooler temperature under the proper conditions for this block force test. Additional work is needed to draw a proper comparison between the block force experiment and the model for a non-shape set structure.

3.4.3 Discussion

The experimental block force tests in this work would benefit from many improvements. In particular and perhaps most importantly, this test was affected considerably by thermal expansion of the fixtures resulting from the crosshead control method used to fix the displacement of the knit samples. This coupled with a slight delay in temperature stabilization of the fixtures caused a significant initial increase in load upon fixing the crosshead motion as the temperature of the

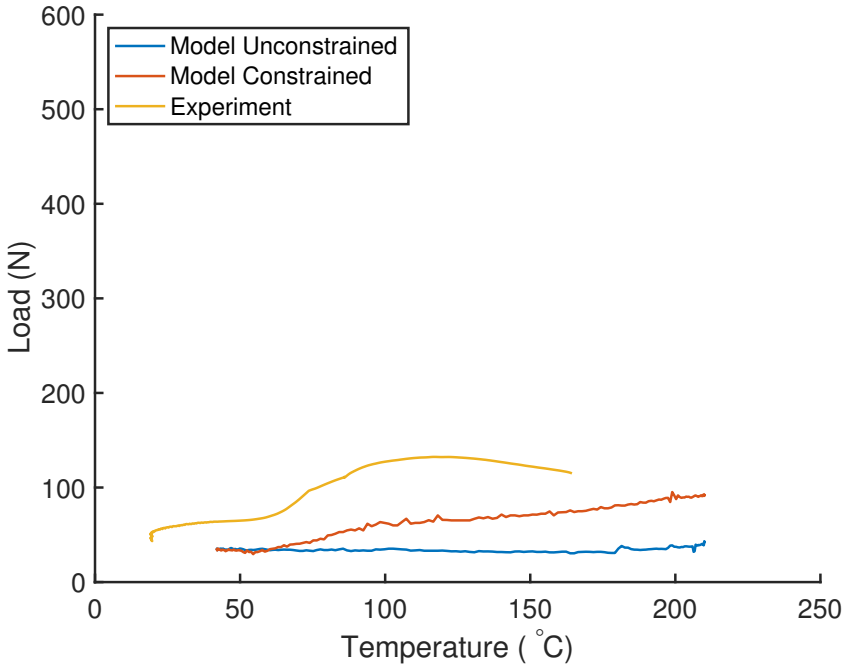

Figure 3.25: Blocking force generated by non-shape set sample under constant displacement.

thermally massive fixtures continued to stabilize and induce thermal expansion. Future studies should utilize fixtures with lower coefficients of thermal expansion and decrease temperature rate significantly to allow for thermal stabilization of all fixtures.

As mentioned in section 3.3.3, calibration of model parameters affecting reverse transformation for the shape set sample was poor. Since block force tests are solely affected by reverse transformation, this offset the reverse transformation temperatures of the model from those of the shape set block force experiment significantly. In addition, the shape set experimental sample reached the limits allowed by the load cell during this test, and therefore the test was terminated prematurely. The combination of load cell limits, poor calibration, and thermal expansion of the fixtures render comparison of this experiment with the model results very difficult.

The non-shape set results for both iso-force and block force tests would benefit from many improvements as well. In particular, more carefully considered temperature ranges should be employed for both iso-force and block force FEA analyses. Disparities in temperature alone caused misalignment in displacement magnitudes when compared with experiments. Additionally, un-

constrained models experienced very limited displacement recovery while experiments and constrained recovered some displacement. This may indicate that course-wise forces are important to structural recovery during reverse transformation.

3.5 Conclusions

Models of knitted structures must carefully consider many aspects of the proposed experimental tests to achieve accurate results. Shape set models behaved in the most expected manner. The results of the shape set 36 N iso-force experiment compared against the model results demonstrate significant potential for accurate model prediction of knit performance with careful consideration of boundary conditions. Due to the high loads studied in this work, full recovery in both experiments and models is not achieved. Therefore, it is important during iso-force experiments to unload between thermal cycles to avoid the accumulation of unrecovered martensite. If full recovery is desired, continued cycling under constant load may eventually saturate the unrecovered sections, allowing transformation to occur only in stitch legs.

Non-shape set models and experiments were found to be sensitive to initial temperature and loading conditions. The initial stress state of the knitted wire led to stress induced transformation upon loading, greatly reducing the magnitude of displacement upon thermally induced transformation when compared with the shape set models. In future work, temperature ranges that are more similar to those used in experiments should be used in modeling non-shape set structures.

Block force experiments suffered as a result of uncontrolled thermal expansion in the fixtures holding the sample. Models predicted high force outputs where geometry recovery (i.e. recovery of structural displacement) was possible, and while experiments indicated potential high force outputs, additional tests with careful considerations for fixture expansion must be performed to confirm this.

Overall, as geometric deformation was a dominant factor in transformation displacement magnitude, increased loading inhibited performance as it induced irrecoverable geometric deformation. The deformed geometry rendered the restoring forces of transformation insufficient to recover the original geometry.

It is recommended that some experiments performed in this work be repeated and compared against model results. Shape set iso-force cycles performed under 72 N and 108 N loads should be revisited, each cycle initiating from an unloaded hot state. This is expected to reduce accumulated martensite (which results from continuous cycling) and lead to experimental performance in the ranges predicted via model runs. In addition, non-shape set iso-force experiments from all loads studied should be performed subjected to the same temperature range as implemented in the model. Each of these cycles should also be initiated from an unloaded hot state. This is expected to not only reduce martensite accumulation as in the shape set experiments, but to generate martensite upon loading in a manner more consistent with model predictions.

4. SUMMARY AND CONCLUSIONS

4.1 Summary

This work explored the implementation of a finite element model of a knitted SMA structure under multiple representative load cases. Models for shape set structures and non-shape set structures were explored. Iso-force thermal cycles under three different high loads were modeled and compared against experimental results. Block force analyses were also performed and compared against experimental results. For all representative load cases modeled, two constraint cases were studied: a constrained case, where wale length is held fixed, and an unconstrained case, where wale length is allowed to shorten thereby enabling significant displacement due to geometric deformation. The unconstrained case represents a true uniaxial load case. However, a true uniaxial load case was not achieved experimentally, indicating a need for improved fixturing that allows for the macro-scale Poisson effect (i.e. wale length shortening during geometric deformation).

Shape set iso-force models compared as expected with experiments for the 36 N load case. Experimentally, when performing multiple thermal cycles, the importance of unloading between each loaded thermal cycle became apparent due to the accumulation of unrecovered martensite. Shape set block force models predicted high force outputs; experiments were unreliable due to thermally expanding fixtures and limited load cell capacity. Non-shape set knit structures were shown to be more sensitive to their initial temperature and load conditions than shape set structures due to their pre-stressed state, which caused the generation of stress-induced transformation during loading under constant high temperature.

4.2 Challenges

Both experimental and modeling aspects of this work experienced challenges. The experimental challenges faced were fairly straightforward and mostly attributed to insufficient fixturing methods. Though fixtures used in this work were intended to evenly distribute load to each wale, large structural displacements were not taken into account or accommodated due to the fixed con-

nection points on the grip. Additionally, these fixtures were very responsive to thermal stimuli, and thermal expansion was a major factor in the poor experimental results of the block force tests.

With regards to challenges experienced in the modeling effort, computational expense may hinder more complex analyses of knitted SMA structures. The VUMAT employed in this work greatly increased computation time, and analyses took on the order of 10 to 100 hours to complete. Additional complexities in the non-shape set analyses including strain mapping and potential interference with the extended segments of the RVE require further study and confirmation.

4.3 Further Study

This work represents a preliminary study in knitted SMA performance under high loads. The basic understanding of knit performance gained can be applied to other investigations of knitted SMAs, including additional knit architectures and load cases. In future work, key lessons learned will be implemented. Future experimental iso-force tests will fully unload each sample between thermal cycles, allowing full reverse transformation. Experiments to be repeated for improved comparison against model results presented here include 72 N and 108 N iso-force tests for both shape set and non-shape set samples; experiments will be initiated from an unloaded state and will take measures to match temperature profiles utilized by the modeling analyses. In addition, future experimental block force tests will take measures to control fixture thermal expansion. Experiments with larger samples and carefully considered fixtures toward a true uniaxial load case are also recommended.

Future modeling efforts will focus on non-shape set studies. Errors in strain mapping will be investigated and resolved, and temperature ranges modeled will be adjusted to correspond to experiments. Inconsistencies with forward transformation temperatures at high loads will also be studied. In addition, efforts to reduce computational expense will be implemented. For example, contact area is for constrained cases is shown to be relatively small and predictable; therefore, a reduced region can be checked for contact in this type of analysis. Inefficiencies in the current implementation of the material model will also be investigated and reduced where possible.

REFERENCES

[1] M. Thomas, *Mary Thomas's Knitting Book*. Courier Corporation, July 2013. Google-Books-ID: GP7DAgAAQBAJ.

[2] K. J. Wu, "1,700-Year-Old Sock Spins Yarn About Ancient Egyptian Fashion," Oct. 2018.

[3] J. C. H. H. F.T.I and P. J. Doyle, "Fundamental Aspects of the Design of Knitted Fabrics," *Journal of the Textile Institute Proceedings*, vol. 44, pp. P561–P578, Aug. 1953.

[4] A. Pavko-Cuden, "Geometrical models of weft knitted loop: Open, normal and compact structure," *Tekstilec*, vol. 53, pp. 113–138, Dec. 2009.

[5] D. Liu, D. Christe, B. Shakibajahromi, C. Knittel, N. Castaneda, D. Breen, G. Dion, and A. Kontsos, "On the role of material architecture in the mechanical behavior of knitted textiles," *International Journal of Solids and Structures*, vol. 109, pp. 101–111, Mar. 2017.

[6] J. Evans, D. Brei, and J. Luntz, "Preliminary Experimental Study of SMA Knitted Actuation Architectures," pp. 369–376, American Society of Mechanical Engineers Digital Collection, Dec. 2007.

[7] F. Peirce, "Geometrical Principles Applicable to the Design of Functional Fabrics," *Textile Research Journal*, vol. 17, pp. 123–147, Mar. 1947.

[8] G. A. V. Leaf and A. Glaskin, "The Geometry of a Plain Knitted Loop," *Journal of the Textile Institute Transactions*, vol. 46, pp. T587–T605, Sept. 1955.

[9] M. W. Suh, "A Study of the Shrinkage of Plain Knitted Cotton Fabric, Based on the Structural Changes of the Loop Geometry Due to Yarn Swelling and Deswelling," *Textile Research Journal*, vol. 37, pp. 417–431, May 1967.

[10] Christina Garza-Brown, "How to Read Knitting Stitch Patterns: A Knitter's Guide," Mar. 2019. Library Catalog: knitfarious.com Section: Knitting Tutorials.

[11] D. Lagoudas, *Shape memory alloys: modeling and engineering applications*. New York: Springer, 1st ed ed., 2008.

[12] T.-H. Chiang, "Catheter apparatus employing shape memory alloy structures," Apr. 1990. Library Catalog: Google Patents.

[13] J. Abel, J. Luntz, and D. Brei, "Hierarchical architecture of active knits," *Smart Materials and Structures*, vol. 22, p. 125001, Nov. 2013.

[14] J. Abel, *Active Knit Actuation Architectures.* PhD thesis, University of Michigan, 2014.

[15] K. Eschen and J. Abel, "Effect of Geometric Design Parameters on Contractile SMA Knitted Actuator Performance," American Society of Mechanical Engineers Digital Collection, Nov. 2017.

[16] "Performance and prediction of large deformation contractile shape memory alloy knitted actuators."

[17] S. Yi, C. Weinberg, K. Eschen, and J. Abel, "Preliminary Experimental Study of the Effect of Shape Setting on Knitted SMA Structures," American Society of Mechanical Engineers Digital Collection, Nov. 2017.

[18] K. Eschen, R. Granberry, and J. Abel, "Guidelines on the design, characterization, and operation of shape memory alloy knitted actuators," *Smart Materials and Structures*, vol. 29, p. 035036, Feb. 2020. Publisher: IOP Publishing.

[19] T. Tokuda, Y. Shomura, N. Tanigawa, S. Kariya, A. Komemushi, H. Kojima, and S. Sawada, "Mechanical Characteristics of Composite Knitted Stents," *CardioVascular and Interventional Radiology*, vol. 32, pp. 1028–1032, Sept. 2009.

[20] R. E. White, C. Mungatana, and M. Topazian, "Esophageal stent placement without fluoroscopy," *Gastrointestinal Endoscopy*, vol. 53, pp. 348–351, Mar. 2001.

[21] P. Zilla, L. Moodley, M. F. Wolf, D. Bezuidenhout, M. S. Sirry, N. Rafiee, W. Lichtenberg, M. Black, and T. Franz, "Knitted nitinol represents a new generation of constrictive external vein graft meshes," *Journal of Vascular Surgery*, vol. 54, pp. 1439–1450, Nov. 2011.

[22] E. Fournier, R. Devaney, M. Palmer, J. Kramer, R. El Khaja, and M. Fonte, "Superelastic Orthopedic Implant Coatings," *Journal of Materials Engineering and Performance*, vol. 23, pp. 2464–2470, July 2014.

[23] X. Wang, C. Han, X. Hu, H. Sun, C. You, C. Gao, and Y. Haiyang, "Applications of knitted mesh fabrication techniques to scaffolds for tissue engineering and regenerative medicine," *Journal of the Mechanical Behavior of Biomedical Materials*, vol. 4, pp. 922–932, Oct. 2011.

[24] J. Q. Dong, "Low profile, high stretch knit prosthetic device," May 2005.

[25] J. M. Abel, P. Mane, B. Pascoe, J. Luntz, and D. Brei, "Experimental investigation of active rib stitch knitted architecture for flow control applications," in *Active and Passive Smart Structures and Integrated Systems 2010*, vol. 7643, p. 76430H, International Society for Optics and Photonics, Apr. 2010.

[26] B. Holschuh, E. Obropta, L. Buechley, and D. Newman, "Materials and Textile Architecture Analyses for Mechanical Counter-Pressure Space Suits using Active Materials," in *AIAA SPACE 2012 Conference & Exposition*, (Pasadena, California), American Institute of Aeronautics and Astronautics, Sept. 2012.

[27] R. Granberry, J. Abel, and B. Holschuh, "Active Knit Compression Stockings for the Treatment of Orthostatic Hypotension," in *Proceedings of the 2017 ACM International Symposium on Wearable Computers*, ISWC '17, (New York, NY, USA), pp. 186–191, ACM, 2017. event-place: Maui, Hawaii.

[28] K. Eschen, J. Abel, R. Granberry, and B. Holschuh, "Active-Contracting Variable-Stiffness Fabrics for Self-Fitting Wearables," American Society of Mechanical Engineers Digital Collection, Nov. 2018.

[29] R. M. Granberry, K. Eschen, J. Abel, and B. Holschuh, "Active knit compression garments, devices and related methods," Jan. 2019.

[30] R. Granberry, K. Eschen, B. Holschuh, and J. Abel, "Functionally graded knitted actuators with niti-based shape memory alloys for topographically self-fitting wearables," *Advanced Materials Technologies*, Oct. 2019.

[31] J. Abel, J. Luntz, and D. Brei, "Two-Dimensional Analytical Model and Experimental Validation of Garter Stitch Knitted Shape Memory Alloy Actuator Architecture," pp. 353–368, American Society of Mechanical Engineers Digital Collection, Feb. 2010.

[32] H. van der Merwe, B. Daya Reddy, P. Zilla, D. Bezuidenhout, and T. Franz, "A computational study of knitted Nitinol meshes for their prospective use as external vein reinforcement," *Journal of Biomechanics*, vol. 41, pp. 1302–1309, Jan. 2008.

[33] F. Auricchio and R. L. Taylor, "Shape-memory alloys: modelling and numerical simulations of the finite-strain superelastic behavior," *Computer Methods in Applied Mechanics and Engineering*, vol. 143, pp. 175–194, Apr. 1997.

[34] M. Hatamura and T. Wada, "Huge Shape Recovery of the Knitting actuators made by TiNi Shape Memory Alloy Wires," *Transactions of the Materials Research Society of Japan*, vol. 40, no. 3, pp. 281–285, 2015.

[35] ABAQUS, "Overview of ABAQUS/Explicit."

[36] A. M. Prior, "Applications of implicit and explicit finite element techniques to metal forming," *Journal of Materials Processing Technology*, vol. 45, pp. 649–656, Sept. 1994.

[37] ABAQUS, "Mass scaling." Library Catalog: abaqus-docs.mit.edu.

[38] SIMULIA, "Abaqus 2017 Documentation."

[39] Simulia, "Domain decomposition."

[40] P. Wriggers, "Finite element algorithms for contact problems," *Archives of Computational Methods in Engineering*, vol. 2, pp. 1–49, Dec. 1995.

[41] I. V. Kragelsky, M. N. Dobychin, and V. S. Kombalov, *Friction and Wear: Calculation Methods*. Elsevier Science & Technology, May 1982. Google-Books-ID: 8EA0QgAACAAJ.

[42] Simulia, "Contact robustness and performance." Webinar, 2019.

[43] Simulia User Assistance, "Contact formulations in Abaqus/Standard," 2017.

[44] Simulia, "Abaqus Benchmarks Guide (6.13)."

[45] E. S. Watson and M. J. O'neill, "Differential microcalorimeter," Aug. 1966.

[46] K. Kus and T. Breczko, "DSC-investigations of the effect of annealing temperature on the phase transformation behaviour in Ni-Ti shape memory alloy," p. 9.

[47] Z. Li, X. Cheng, and Q. ShangGuan, "Effects of heat treatment and ECAE process on transformation behaviors of TiNi shape memory alloy," *Materials Letters*, vol. 59, pp. 705–709, Mar. 2005.

[48] D. A. Miller and D. C. Lagoudas, "Influence of cold work and heat treatment on the shape memory effect and plastic strain development of NiTi," *Materials Science and Engineering: A*, vol. 308, pp. 161–175, June 2001.

[49] E08 Committee, "Standard Test Method for Mechanical Uniaxial Constant Force Thermal Cycling of Shape Memory Alloys," tech. rep., ASTM International.

[50] P. B. C. Leal and M. A. Savi, "Shape memory alloy-based mechanism for aeronautical application: Theory, optimization and experiment," *Aerospace Science and Technology*, vol. 76, pp. 155–163, May 2018.

[51] O. Benafan, S. A. Padula, R. D. Noebe, D. W. Brown, B. Clausen, and R. Vaidyanathan, "An in situ neutron diffraction study of shape setting shape memory NiTi," *Acta Materialia*, vol. 61, pp. 3585–3599, June 2013.

[52] Brad Simmons, "Constructing Tangent Lines to Circles."

APPENDIX A

METHOD OF DEVELOPING TANGENT LINES BETWEEN CIRCLES

In developing knit structure geometries, the generation of perfectly tangent lines is important for reducing stress concentrations which occur at the connection points between the stitch legs and needle and sinker loops. The following method is used to develop inner tangent lines [52].

Circles with centers A_1 and A_2 have radii of R_1 and R_2 respectively. These circles will be referred to as circle 1 and circle 2. First, three construction circles are drawn. Two circles of radius R_1 plus R_2 are constructed with centers A_1 and A_2 respectively. A third circle with the center at the midpoint between the two circle centers is drawn such that the circle passes through both A_1 and A_2. Intersection points between the center construction circle and the construction circles with centers A_1 and A_2 are noted. The intersection points closest to the desired tangent line are marked B_1 and B_2. Next, two construction lines are drawn, connecting B_1 with A_1 and B_2 with A_2 respectively. The intersection points between these lines and circles 1 and 2 are marked as C_1 and C_2. The tangent line between circles 1 and 2 is the line that connects C_1 with C_2. The tangent line is perpendicular to lines $\overline{AB_1}$ and $\overline{AB_2}$.

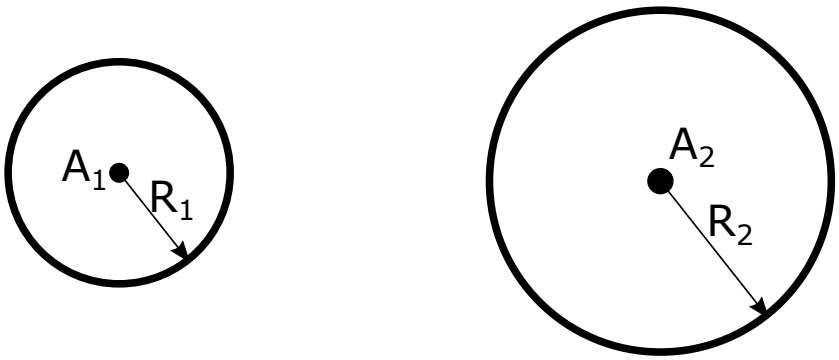

Figure A.1: Circles between which an inner tangent line is sought.

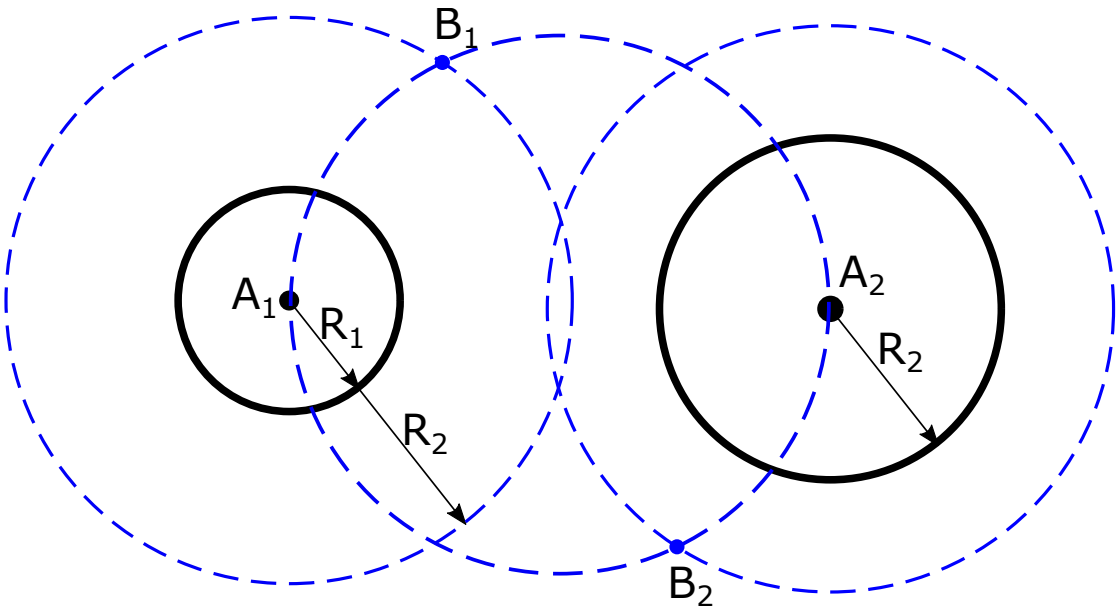

Figure A.2: Construction circles added: Circles with radius of R_1+R_2 and centers A_1 and A_2 respectively, and circle connecting center A_1 to A_2.

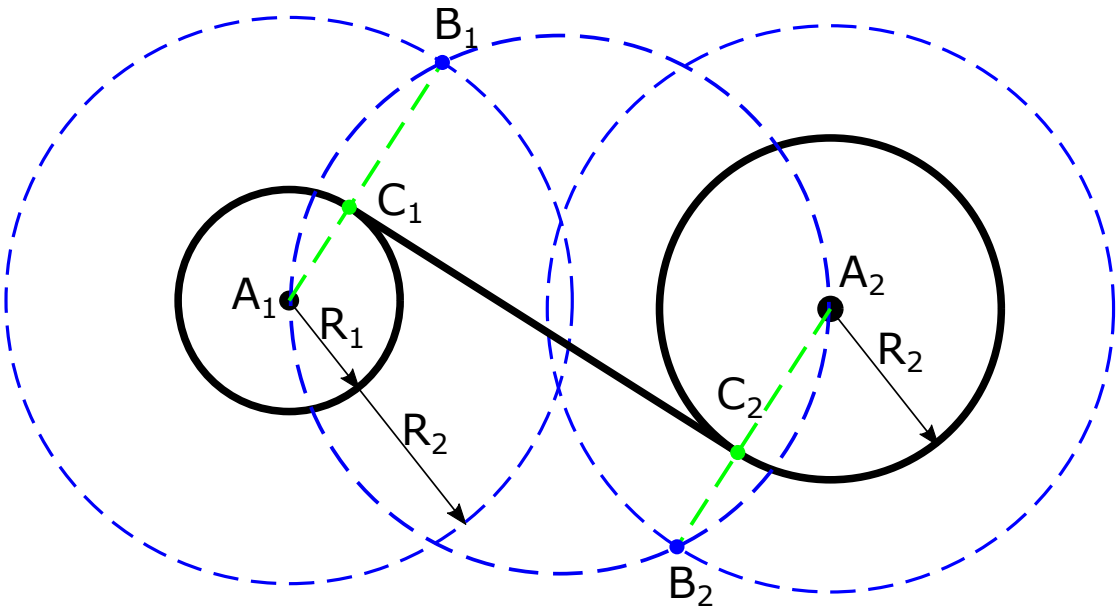

Figure A.3: Construction lines added from A_1 to B_1 and A_2 to B_2. Intersection points C_1 and C_2 used to construct tangent line.

APPENDIX B

CHANGES IN DIFFERENTIAL SCANNING CALORIMETRY RESULTS ACROSS KNITTED SAMPLES

The knitting process, particularly when performed manually, greatly deforms wire to create interlocking loops. Cold working has been shown to impact transformation properties and widen martensitic peaks [48]. The deformations imparted during the knitting process may also influence transformation properties in a similar manner. Figure B.1 shows the results of DSC tests performed on wire off the spool (figure B.1a) and wire from a non-shape set knit sample (figure B.1b). These results represent the cooling curve only and are not normalized by the baseline run to more clearly show the martensitic peaks. The martensitic peak of the spool sample is wide and slight. The peak of the non-shape set knit sample is almost unnoticeable, as it has widened considerably (further analysis confirms that a martensitic peak is in fact present). This indicates that knitting does influence transformation properties in a similar way to cold working, though the impacts of this are yet to be investigated.

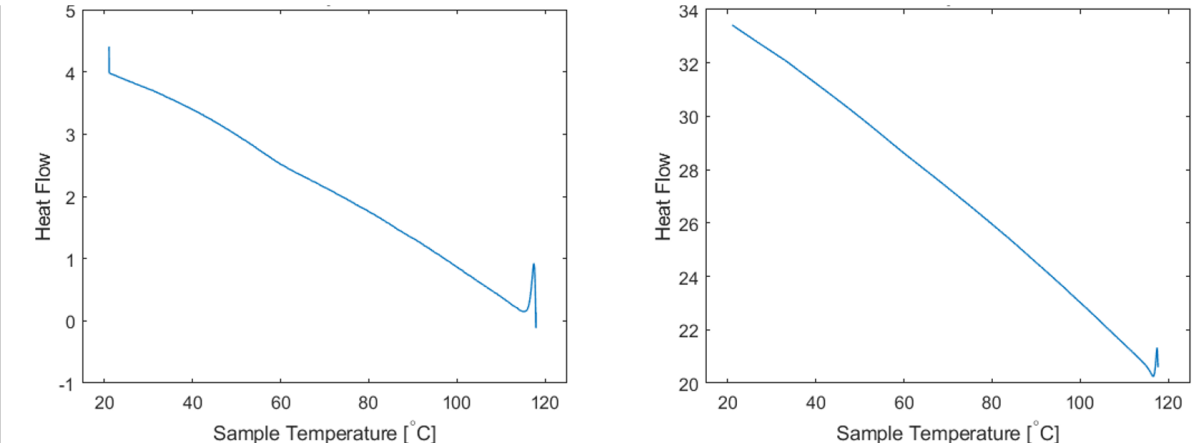

(a) Spool sample (not heat treated).

(b) As knit, non-shape set sample.

Figure B.1: Non-normalized DSC results during cooling for wire taken off the spool and wire from a non-heat treated knit sample.

APPENDIX C

COMMENTS ON MODEL STABILITY

Models developed using explicit solution methods of finite element analysis must carefully consider accuracy of the generated solution and model stability. Many factors affect model stability but solution time increment is often the most important. Time increment is also paramount in computational expense, and maximum time increment that allows model stability is desired. A study investigating model stability due to time increment was performed for a simple displacement of the shape set knit model. Importantly, this study was performed using a frictionless contact formulation. The results of this study indicate that the smallest time increment studied produces an unstable model. Though oscillations were present in the analyses performed using larger

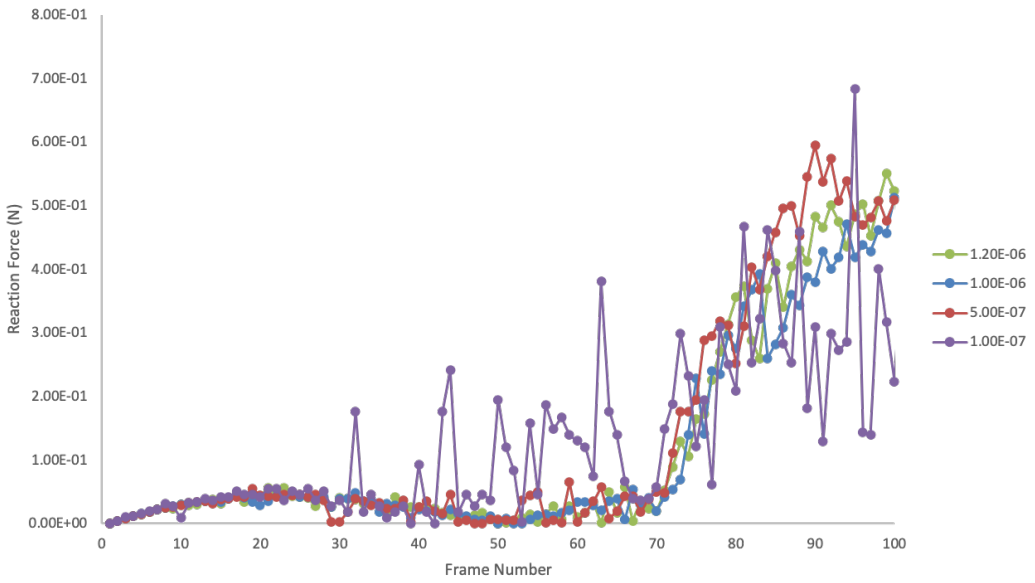

Figure C.1: Results of time step study.

time increments, their similarities regardless of time increment indicates time increment is not the culprit. In fact, frictionless models suffered from an oscillatory phenomenon due to a lack of

dissipative mechanisms. Contact between stitches resulted in a lightly damped vibrational effect which caused fluctuations in reaction force. Analysis time scale was increased to reduce the effect of these dynamic instabilities, though ultimately the addition of friction sufficiently damped these vibrations. As models became more computationally expensive, particularly with the addition of non-shape set considerations, analysis time scale was reduced to decrease computation time and this vibrational effect was not observed.